

INTERNATIONAL JOURNAL OF
MODERN ENGINEERING

The Leading Journal of Engineering, Applied Science and Technology

Industrial

Electronics

Biomedical

Civil

Aerospace

Computer

Electrical

Chemical

Mechanical



ENGINEERING



TIME TO CHANGE THE WAY ACADEMICS WORKS? TRY ACAMEDICS!

If you are not using the Internet, please skip this ad and enjoy the rest of the journal. The average burden of reading this ad is two minutes, which may add two months of productivity to your academic life. Seriously!

Whether you organize a conference, publish a journal, or serve on a committee to collect and review applications, you can use the Internet to make your life easier. We are not talking about emails. We are talking about state-of-the-art online systems to collect submissions, assign them to reviewers, and finally make a decision about each submission. We are talking about value-added services, such as payment and registration systems to collect registration fees online. We are talking about digital document services, such as proceedings CD/DVD development and duplication, or creating professional-looking digital documents.

Finally, we are talking about AFFORDABLE PRICE, QUALITY, and CUSTOMIZATION. And we are talking about each of them at the same time.

By the way, you don't have to be a computer geek to use our systems. We have a couple of them, and they will do all the technical mumbo jumbo for you. We also have a few select people from academics like you, and they know what you do. You just relax and enjoy our systems.

If you are still reading this ad, chances are you are interested in our systems or services. So, visit us at www.acamedics.com. While you are there, check the names of our clients as well. Most of them are quite familiar, but the list is too long to include here.



INTERNATIONAL JOURNAL OF MODERN ENGINEERING

The INTERNATIONAL JOURNAL OF MODERN ENGINEERING (IJME) is an independent, not-for-profit publication, which aims to provide the engineering community with a resource and forum for scholarly expression and reflection.

IJME is published twice annually (Fall and Spring issues) and includes peer-reviewed articles, book and software reviews, editorials, and commentary that contribute to our understanding of the issues, problems, and research associated with engineering and related fields. The journal encourages the submission of manuscripts from private, public, and academic sectors. The views expressed are those of the authors and do not necessarily reflect the opinions of IJME or its editors.

EDITORIAL OFFICE:

Mark Rajai, Ph.D.
Editor-in-Chief
Office: (818) 677-2167
Email: ijmeeditor@iajc.org
Dept. of Manufacturing Systems
Engineering & Management
California State University-
Northridge
18111 Nordhoff Street
Northridge, CA 91330-8332

THE INTERNATIONAL JOURNAL OF MODERN ENGINEERING EDITORS

Editor-in-Chief:

Mark Rajai

California State University-Northridge

Associate Editors:

Alok Verma

Old Dominion University

Li Tan

Purdue University North Central

Production Editor:

Philip Weinsier

Bowling Green State University-Firelands

Subscription Editor:

Morteza Sadat-Hossieny

Northern Kentucky University

Financial Editor:

Li Tan

Purdue University North Central

Executive Editor:

Sohail Anwar

Penn State University

Manuscript Editor:

Philip Weinsier

Bowling Green State University-Firelands

Copy Editors:

Victor J. Gallardo

University of Houston

Li Tan

Purdue University North Central

Publishers:

Jerry Waite

University of Houston

Hisham Alnajjar

University of Hartford

Web Administrator:

Saeed Namyar

Namyar Computer Solutions

TABLE OF CONTENTS

<i>Editor's Note: Reflections on IAJC and the Joint International Conference with ASEE.....</i>	<i>3</i>
<i>Philip Weinsier, IJME Manuscript Editor</i>	
<i>Analysis of Brushed DC Machinery Faults with Coupled Finite Element Method and Equivalent Circuit Model.....</i>	<i>5</i>
<i>Todd D. Batzel, Penn State Altoona; Nicholas C. Becker, Penn State Altoona; Mihai Comanescu, Penn State Altoona</i>	
<i>Energy Harvesting with Piezoelectric Fiber Composite from Mechanical Vibrations.....</i>	<i>14</i>
<i>Faruk Yildiz, Sam Houston State University</i>	
<i>Design and Development of a Hypocycloid Engine.....</i>	<i>26</i>
<i>Tom Conner, Arizona State University; Sangram Redkar, Arizona State University</i>	
<i>The Impact of Motorsports Engineering on Automotive Performance.....</i>	<i>32</i>
<i>Pete Hylton, Indiana University Purdue University Indianapolis; Andrew Borme, Indiana University Purdue University Indianapolis; Kirk Barber, Indiana University Purdue University Indianapolis; Paul Lucas, Indiana University Purdue University Indianapolis; Lee Beard, Don Schumacher Racing</i>	
<i>Tool-condition Monitoring in CNC Turning Operations: A Statistical Approach for Quick Implementation.....</i>	<i>37</i>
<i>Samson S. Lee, Central Michigan University</i>	
<i>Overview and Design of Near-net Formed Spherical Involute Straight Bevel Gears.....</i>	<i>47</i>
<i>Haris Ligata, American Axle & Manufacturing; Henry H. Zhang, Purdue University</i>	
<i>Bit-Error Aware Lossless Image Compression.....</i>	<i>54</i>
<i>Li Tan, Purdue University North Central; Liangmo Wang, Nanjing University of Science and Technology, China</i>	
<i>Analog Breakthrough Detection Using Laser-induced, Thermal Diffusion Shock Waves.....</i>	<i>60</i>
<i>Jun Kondo, University of Hartford; Saeid Moslehpour, University of Hartford; Hisham Alnajjar, University of Hartford</i>	
<i>A Custom Vibration Test Fixture Using a Subwoofer.....</i>	<i>68</i>
<i>Dale H. Litwhiler, Penn State Berks</i>	
<i>Border Gateway Protocols.....</i>	<i>74</i>
<i>Sadeta Krijestorac, Morehead State University; Marc Beck, University of Louisville; Jonathan Bagby, Florida Atlantic University</i>	
<i>A Multiple-Access Protocol for Multimedia Transmission over Wireless ATM Networks.....</i>	<i>77</i>
<i>Hong Yu, Capitol College; Mohammed Arozullah, The Catholic University of America</i>	
<i>Instructions for Authors: Manuscript Requirements.....</i>	<i>86</i>

EDITOR'S NOTE: REFLECTIONS ON IAJC AND THE JOINT INTERNATIONAL CONFERENCE WITH ASEE



Philip Weinsier, IJME Manuscript Editor

As we in higher education and industry reflect back on the first decade in this new millennium, we realize that the sharing of ideas and resources is the best way for us to create a better future for the next generation of students, faculty, and researchers. In the competitive and tight global markets of the 21st century, leading companies across industry have embarked on massive reorganizations, mergers, partnerships, and all sorts of collaborative projects with their like-minded peers and rivals in order to not only survive but grow and thrive. But, as industry changes with time, so must academia. Conversely, as academic R&D efforts provide advancements in technology, so must industry provide a quick turnaround from concept to market. However, many academic organizations, journals, and conferences have been slow to adapt and provide the necessary platforms for the dissemination of knowledge.

Beginning in 2006, the editorial board of the International Association of Journals and Conferences (IAJC) embarked on groundbreaking and unprecedented efforts to establish strategic partnerships with other major rival journals and organizations to share resources and offer authors a unique opportunity to come to one conference and publish their papers in a broad selection of journals representing interests as diverse as those of the researchers and educators in fields related to engineering, engineering technology, industrial technology, mathematics, science and teaching. These efforts resulted in an innovative model of joint international conferences that includes a variety of organizations and journals.

IAJC joint and independent international conferences have been a great success with the main conferences being held in the United States and regional, simultaneous conferences, in other parts of the world. In addition to bringing

people together at its conference venues, IAJC attracts myriad journals that wish to publish the best of what its attendees have to offer, thereby creating excitement in academic communities around the world. IAJC is a first-of-its-kind, pioneering organization. It is a prestigious global, multilayered umbrella consortium of academic journals, conferences, organizations and individuals committed to advancing excellence in all aspects of technology-related education.

Conference Statistics: A total of 285 abstracts from more than 100 educational institutions and companies were submitted from around the world. In the multi-level review process, papers are subjected to blind reviews by three or more highly qualified reviewers. For this conference, a total of 80 papers were accepted. Most of these were presented and are published in the conference proceedings. This reflects an acceptance rate of less than 30%, which is one of the lowest acceptance rates of any international conference.

This conference was sponsored by the International Association of Journals and Conferences (IAJC), which includes 13 member journals and a number of universities and organizations. Other sponsors were the American Society for Engineering Education (ASEE) and the Institute of Electrical and Electronics Engineers (IEEE). Selected papers from this conference will be published in one of the 13 IAJC member journals. Organizing such broad conferences is a monumental task and could not be accomplished without the help and support of the conference committee, the division/session chairs and the reviewers. Thus, we offer our sincerest thanks to all for their hard work and dedication in the development of the outstanding 2011 conference program. We personally hope you will seek them out to thank them for their fine work.

Editorial Review Board Members

Listed here are the members of the IAJC International Review Board, who devoted countless hours to the review of the many manuscripts that were submitted for publication. Manuscript reviews require insight into the content, technical expertise related to the subject matter, and a professional background in statistical tools and measures. Furthermore, revised manuscripts typically are returned to the same reviewers for a second review, as they already have an intimate knowledge of the work. So I would like to take this opportunity to thank all of the members of the review board.

As we continually strive to improve upon our conferences, we are seeking dedicated individuals to join us on the planning committee for the next conference—scheduled for fall, 2012. Please watch for updates on our web site (www.IAJC.org) and contact us anytime with comments, concerns or suggestions. On behalf of the 2011 IAJC-ASEE conference committee and IAJC Board of Directors, we thank all of you who participated in this great conference and hope you will consider submitting papers in one or more areas of engineering and related technologies for future IAJC conferences.

If you are interested in becoming a member of the IAJC International Review Board, send me (Philip Weinsier, IAJC/IRB Chair, philipw@bgsu.edu) an email to that effect. Review Board members review manuscripts in their areas of expertise for all three of our IAJC journals—IJME (the International Journal of Modern Engineering), IJERI (the International Journal of Engineering Research and Innovation), TIJ (the Technology Interface International Journal)—and papers submitted to the IAJC conferences.

Mohammad Badar	Rita Hawkins	Mani Manivannan	Ajay K. Sharma
Mehmet Bahadir	David He	G.H. Massiha	J.Y. Shen
Rendong Bai	Youcef Himri	Jim Mayrose	Ehsan Sheybani
Terrance Barkan	Xiaobing Hou	Thomas McDonald	Musibau Shofoluwe
Kevin Berisso	Shelton Houston	David Melton	Carl Spezia
Kanninika Bhatnagar	Luke Huang	Richard Meznarich	Randy Stein
Elinor Blackwell	Charles Hunt	NagaMani Molakatala	Adam Stienecker
Boris Blyukher	Dave Hunter	Ali Mottahedi	Pingping Sun
Walter Buchanan	Pete Hylton	Sam Mryyan	Jalal Taheri
Jessica Buck	Ghassan Ibrahim	Wilson Naik	Roohallah Taherkhani
John Burningham	John Irwin	Arun Nambiar	Li Tan
Shaobiao Cai	Fawaz Jabri	Ramesh Narang	Ravindra Thamma
Vigyan Chandra	Anwar Jawad	Argie Nichols	Li-Shiang Tsay
Isaac Chang	Sudershan Jetley	Hamed Niroumand	Jeffrey Ulmer
Hans Chapman	Keith Johnson	Troy Ollison	Mihaela Vorvoreanu
Rigoberto Chinchilla	Julius Jow	Reynaldo M Pablo Jr.	Philip Waldrop
Raj Chowdhury	Rex Kanu	Basile Panoutsopoulos	Abram Walton
Michael Coffman	Khurram Kazi	Jose Pena	Haoyu Wang
Kanchan Das	Satish Ketkar	Karl Perusich	Jyhwen Wang
Paul Deering	Daphene Cyr Koch	Thongchai Phairoh	Liangmo Wang
Brad Deken	John Kugler	Patty Polastri	Tom Warms
Raj Desai	Ognjen Kuljaca	Mike Powers	Baijian (Justin) Yang
Dave Dillon	Chakresh Kumar	Huyu Qu	Faruk Yildiz
David Domermuth	Zaki Kuruppallil	John Rajadas	Emin Yilmaz
Marilyn Dyrud	Ronald Land	Desire Rasolomampionona	Yuqiu You
Mehran Elahi	Jane LeClair	Mohammad Razani	Pao-Chiang Yuan
Ahmed Elsayy	Jay Lee	Mulchand Rathod	Biao Zhang
Bob English	Margaret Lee	Sangram Redkar	Chongming Zhang
Rasoul Esfahani	Shiyoung Lee	Michael Reynolds	Jinwen Zhu
Fereshteh Fatehi	Soo-Yen Lee	Marla Rogers	
Dominic Fazarro	Chao Li	Mehdi Safari	
Verna Fitzsimmons	Stanley Lightner	Anca Sala	
Richard Freeman	Jimmy Linn	Darrel Sandall	
Hamed Hakimzadeh	Dale Litwhiler	Balaji Sethuramasamyraja	
Mohsen Hamidi	Daniel Lybrook	Mehdi Shabaninejad	
Bernd Haupt	Sudhir Madhavaram	Hiral Shah	

ANALYSIS OF BRUSHED DC MACHINERY FAULTS WITH COUPLED FINITE ELEMENT METHOD AND EQUIVALENT CIRCUIT MODEL

Todd D. Batzel, Penn State Altoona; Nicholas C. Becker, Penn State Altoona; Mihai Comanescu, Penn State Altoona

Abstract

Although brush-type DC machinery has lost market share over the years to its brushless counterparts, it still maintains a significant presence in the automotive, aerospace, power tool, and home appliance industries. Especially in automotive and aerospace power-system applications, early detection of brush-type, or brushed, DC machine faults will help to avoid problematic system failures, decrease maintenance costs, and increase system reliability. This study focused on a modeling approach that is used to investigate the effects of various fault mechanisms of the brushed DC machine at an early stage in their progression. Results from the proposed model were then used to show the effects of a variety of DC machine failure modes and identify observable parameters to assist in early fault detection. The simulation results were then confirmed through laboratory experiments performed on a DC generator.

Introduction

The brushed DC machine is still widely used in automotive and aerospace systems as an actuator, starter, generator or starter/generator. The detection of impending failures associated with brush-type DC machines can be used to draw attention to the need for maintenance and, therefore, reduce the possibility of a catastrophic system breakdown. In this study, a modeling approach was developed to investigate the effects of various fault mechanisms of the machine and identify measurable parameters that can be used as indicators of a developing fault.

Although research in this area is sparse, investigation of DC machine failure modes have been reported in the literature. A mathematical model was used to investigate the effects of short- and open-circuit armature coils [1], [2]. Position-dependent machine inductances used in this model were pre-determined using finite element analysis (FEA), and brushes were approximated by a variable resistance. Experimental results suggest that field-current harmonics can be used to indicate armature coil short circuits. However, armature open circuits were virtually undetectable.

The approach was modified [3] to include saturation effects using a winding function approach.

A lumped-parameter mathematical model [4], including mechanical parameters inertia and friction, was used to detect brushed permanent-magnet DC machine faults. This proposed technique uses the starting current transient as an indicator of short- and open-circuit armature coils and brush wear. Application of this method was limited to systems where mechanical parameters were well-known. The amount of sparking at the brushes in a DC machine is an accepted measure of commutation quality and, therefore, may be used as an indicator of excessive brush wear. Other studies have presented methods for monitoring the sparking index in the brush DC motor [5], [6].

In this study, a lumped-parameter circuit model was used where each individual armature coil was placed based on the present commutation state. The resulting differential equation model was coupled with a time-stepping finite element analysis to obtain a solution for armature and field voltages and currents. The model, which is readily modifiable to analyze machine faults, was then used to evaluate performance at the onset of faults such as armature open and short circuits, field winding short circuits, commutator segment failures, and brush degradation. The information from these simulations was then used to identify observable parameters that can detect and classify the onset of brushed DC machine failures.

DC Machine Mathematical Equations

Figure 1 shows the armature coil and commutator segment connections of a two-pole brushed DC generator with 12 coils and commutator segments. Coil position in the armature slots is shown in Figure 2, where a double-layer lap winding is used and each coil consists of 15 series-wound conductors. A single brush pair is employed. The voltage across each of the j coils in Figure 1 is

$$v_j = e_j + i_j R_j = \frac{d\lambda_j}{dt} + i_j R_j \quad (1)$$

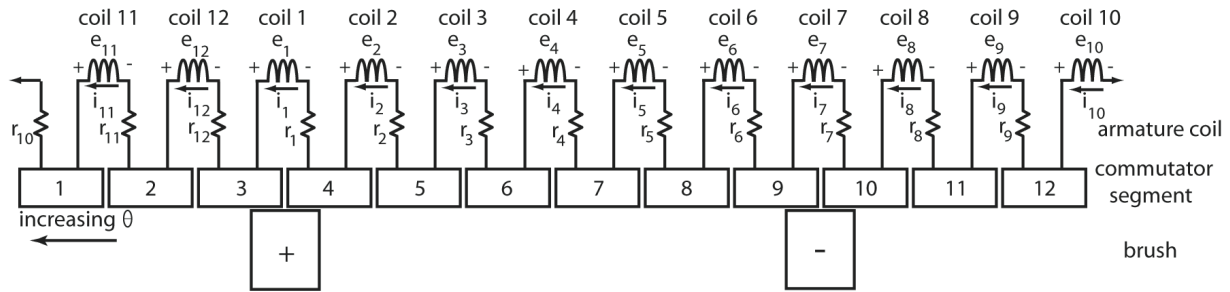


Figure 1. Coil and Commutator Segment Connections for a DC Generator

$$\begin{bmatrix} \lambda_1 \\ \lambda_2 \\ \mathbf{M} \\ \lambda_{12} \\ \lambda_f \end{bmatrix} = \begin{bmatrix} L_{1,1} & L_{1,2} & L & L_{1,12} & L_{1,f} \cos(\theta) \\ L_{2,1} & L_{2,2} & L & L_{2,12} & L_{2,f} \cos(\theta - 30^\circ) \\ \mathbf{M} & \mathbf{M} & \mathbf{O} & \mathbf{M} & \mathbf{M} \\ L_{12,1} & L_{12,2} & L & L_{12,12} & L_{12,f} \cos(\theta + 30^\circ) \\ L_{f,1} \cos(\theta) & L_{f,2} \cos(\theta - 30^\circ) & L & L_{f,12} \cos(\theta + 30^\circ) & L_{f,f} \end{bmatrix} \begin{bmatrix} i_1 \\ i_2 \\ \mathbf{M} \\ i_{12} \\ i_f \end{bmatrix} \quad (2)$$

where, v , e , i and R represent the terminal voltage, induced emf, current, and resistance, respectively, of the coil. For a 12-coil machine with a wound field, the flux linkages can be represented in matrix form, as shown in Equation (2), where θ is the angle between the magnetic axis of the field winding and rotating coil 1.

coils were considered a function of the rotor angle. Vector notation shown in Equation (2) can be simplified to:

$$\lambda = \mathbf{L}(\theta)\mathbf{i} \quad (3)$$

The induced emf vector \mathbf{e} in Equation (1) is determined by:

$$\mathbf{e} = \frac{d}{dt} \lambda = \omega \mathbf{L} \mathbf{i} + \mathbf{L} \frac{d}{dt} \mathbf{i} = e_o + e_L \quad (4)$$

The first term on the right side of Equation (4) represents voltage induced by armature rotation, while the second is due to inductive (self and mutual) coupling between coils.

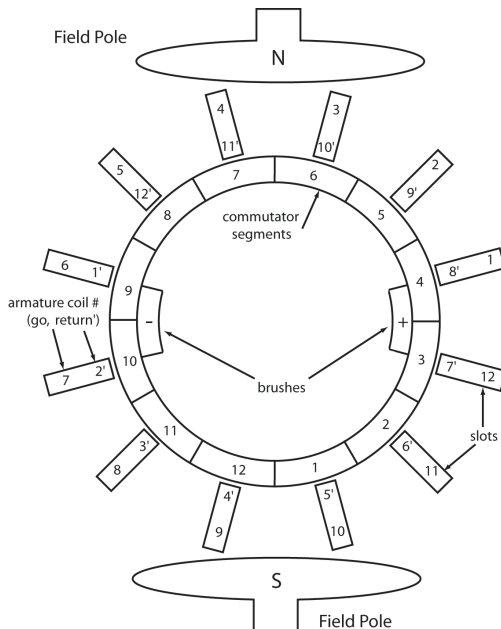


Figure 2. Coil Placement in the Armature

For simplicity, the self and mutual inductances between all armature coils were considered to be constant, while all mutual inductances between the field winding and armature

DC Machine Circuit Model

A simplified model for the DC machine can now be presented. The analytical circuit model for a sample DC generator (with 12 armature coils) is shown in Figure 3. In this model, an index, $j=1$ through 12, was used to identify each coil and commutator segment, s . The modulo 12 index was assigned based on rotor position θ , according to Table 1.

The resistances, r_{a1} , r_{a2} , r_{b1} and r_{b2} , represent the brush-to-commutator contact resistance, which was determined based on rotor position, contact surface area, and current density [7]. The contact conductance for a healthy brush at nominal current density is shown in Figure 4, where it was assumed that the brush never contacts three segments simultaneously. The term g_{\max} was used to represent the maximum brush-to-commutator conductance, which occurs when the brush has maximum contact area with the commutator. The use of a lookup table to identify conductances makes it relatively simple to model certain aspects of brush and commutator wear.

Table 1. Index vs. Rotor Angle

Rotor Angle (θ)	Index (j)	Rotor Angle (θ)	Index (j)	Rotor Angle (θ)	Index (j)
$15^\circ > \theta \geq -15^\circ$	$j=1$	$135^\circ > \theta \geq 105^\circ$	$j=5$	$255^\circ > \theta \geq 225^\circ$	$j=9$
$45^\circ > \theta \geq 15^\circ$	$j=2$	$165^\circ > \theta \geq 135^\circ$	$j=6$	$285^\circ > \theta \geq 255^\circ$	$j=10$
$75^\circ > \theta \geq 45^\circ$	$j=3$	$195^\circ > \theta \geq 165^\circ$	$j=7$	$315^\circ > \theta \geq 285^\circ$	$j=11$
$105^\circ > \theta \geq 75^\circ$	$j=4$	$225^\circ > \theta \geq 195^\circ$	$j=8$	$345^\circ > \theta \geq 315^\circ$	$j=12$

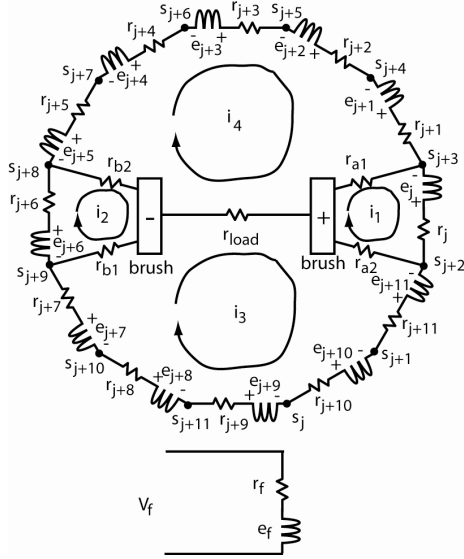


Figure 3. Circuit Model for Brushed DC Generator

The model of Figure 3 can be further simplified by combining series-connected coils, where the coils connected in series depend on the present brush position. The resulting model is shown in Figure 5, where, $e_{\omega n}$, L_n and r_n ($n=1$ to 4) are the induced motional emf, the inductance terms, and resistance of the equivalent coils, respectively, at any rotor position. Applying mesh analysis to the circuit of Figure 5 and including the mutual inductance terms that are not obvious from the circuit diagram yields Equation (5), where

$e_{\omega 1}$ and $e_{\omega 2}$ represent the induced voltages due to motion only in the branches undergoing commutation, while $e_{\omega 3}$ and $e_{\omega 4}$ are the sums of voltages induced due to motion only in the series-connected armature branches not under commutation. The subscripts 1 through 4 have similar meaning when used with the branch currents, resistances,

$$\begin{bmatrix} e_{\omega 1} \\ e_{\omega 2} \\ e_{\omega 3} \\ e_{\omega 4} \\ V_f - e_f \end{bmatrix} = \begin{bmatrix} (r_1 + r_{a1} + r_{a2}) & 0 & -r_{a2} & -r_{a1} & 0 \\ 0 & (r_2 + r_{b1} + r_{b2}) & -r_{b1} & -r_{b2} & 0 \\ -r_{a2} & -r_{b1} & (r_3 + r_{b1} + r_{a2} + r_{load}) & -r_{load} & 0 \\ -r_{a1} & -r_{b2} & -r_{load} & (r_4 + r_{a1} + r_{b2} + r_{load}) & 0 \\ 0 & 0 & 0 & 0 & R_f \end{bmatrix} \begin{bmatrix} i_1 \\ i_2 \\ i_3 \\ i_4 \\ i_f \end{bmatrix} + \begin{bmatrix} L_{11} & -L_{12} & 0 & 0 & -L_{1f} \\ -L_{21} & L_{22} & 0 & 0 & L_{2f} \\ 0 & 0 & L_{33} & -L_{34} & 0 \\ 0 & 0 & -L_{43} & L_{44} & 0 \\ -L_{f1} & L_{f2} & 0 & 0 & L_{ff} \end{bmatrix} \frac{d}{dt} \begin{bmatrix} i_1 \\ i_2 \\ i_3 \\ i_4 \\ i_f \end{bmatrix} \quad (5)$$

and inductances. In vector form, Equation (5) can then be written as Equation (6).

$$\mathbf{e}_{\omega} = \mathbf{r}\mathbf{i} + \mathbf{L} \frac{d}{dt} \mathbf{i} \quad (6)$$

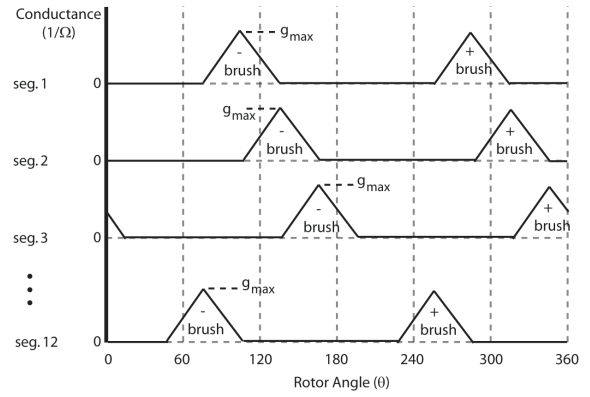


Figure 4. Brush-to-Segment Resistances

Time-Stepping DC Machine Analysis

The DC machine was modeled using magnetostatic FEA tools [8] coupled with the differential circuit equation given in Equation (6). The magnetostatic FEA was capable of determining the instantaneous self and mutual inductance terms and the motional emf (e_{ω}) terms of Equation (6). To obtain the machine state at each time step, the FEA program first uses the present current vector to compute, e_{ω} , \mathbf{L} , and \mathbf{r} based on the brush position and angular velocity. With these FEA results, the differential equation identified by Equation (6) was used to update the current vector. The current determined at each time step becomes the initial condition for the following time step. The magnetostatic FEA tools used in the analysis can be used to determine the

motional voltage, but voltages due to self and mutual inductances must be incorporated into the differential equations linking the FEA result to the time-stepping analysis. The inductance values at each step are determined by FEA [9].

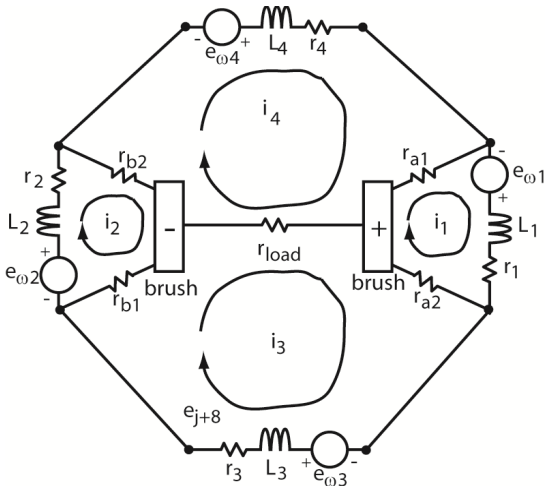


Figure 5. Circuit Model for Brushed DC Generator

As an example, the magnetic flux vector calculated by FEA at a single time step is shown in Figure 6. The magnetic flux and the machine state variables at that time step allows calculation of all coil voltages. Once the induced (due to mechanical motion) coil voltages are determined, the rotor position dictates the electrical circuit configuration (which is brush-position dependent). The resulting circuit configuration is then solved using standard circuit-analysis techniques.

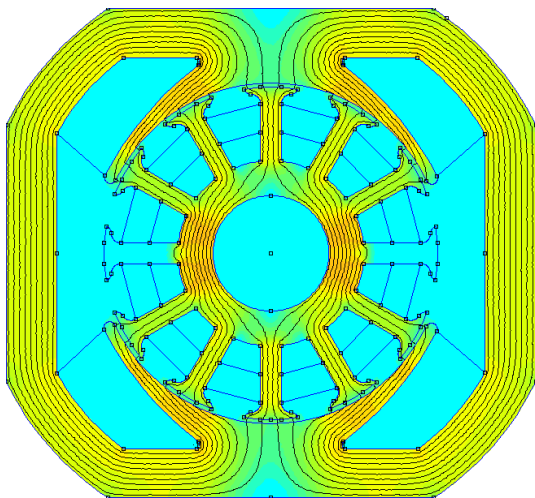


Figure 6. Magnetic FEA Flux Results at a Single Time Step

In summary, the FEA calculation and associated circuit analysis performed at a progression of time steps yielded armature voltage, armature current, field voltage, field current, and even quantities that would not be feasible to measure on a physical system—such as the current in an individual coil. Using this approach, it is rather straightforward and relatively fast to analyze a DC machine operating as a motor or generator under various conditions—even for conditions such as winding failures or brush/commutator defects.

Fault Simulations for a DC Machine

Coupled FEA simulations were performed on a DC machine operating as a starter/generator for normal (baseline) operation as well as a variety of winding and brush/commutator failure modes. Scenarios evaluated include field winding short circuits, armature winding faults, brush resistance increase (due to uneven wear), commutator bar open and short circuits.

Each of these scenarios was evaluated at various operating speeds and load currents to determine observable quantities that are indicative of the respective failure mode. Baseline simulations were first performed to characterize the operation of a healthy DC machine. Although simulations were conducted for various operating conditions, for purposes of comparison all results will be shown with the DC machine acting as a generator at a speed of 3000RPM, a load of 5 ohms, and a constant applied field voltage. For this rotational speed, the 2-pole machine with 12 commutator segments had a pole-passing frequency of 100Hz and a commutation frequency of 600Hz. Figure 7 shows the armature voltage and current, the current in a single coil (which can't easily be measured physically), and the field current FFT. Note the presence of the commutation frequency in both the armature and field current.

Operation with a field winding short circuit was then simulated by altering the winding structure of the FEA machine description. Figure 8 shows the results of a simulation with 12% of the field windings short-circuited. When comparing the baseline results of Figure 7 with the field winding short circuit, note that less armature voltage is produced relative to the field current magnitude with a shorted field winding. This results in the first identified observable effect called the *transfer impedance*, which is defined as the ratio of the induced armature voltage relative to the field current. The decrease in the transfer impedance when the field winding is short-circuited is readily explained. With fewer field turns available to produce magnetic flux at any reference speed, the induced voltage is reduced by Faraday's law.

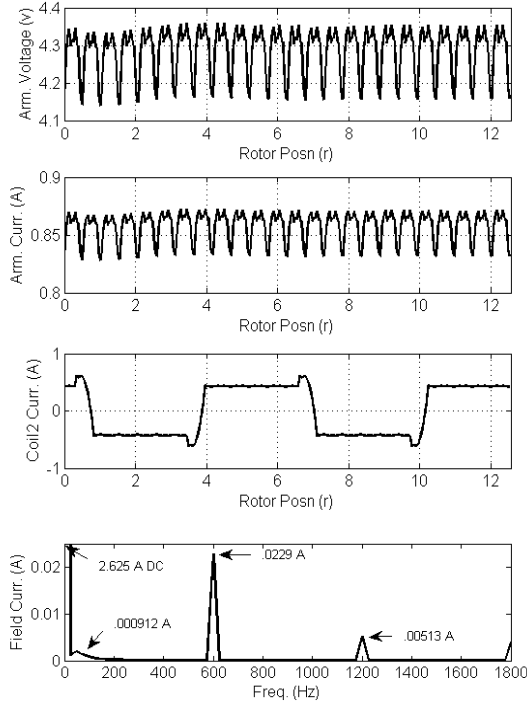


Figure 7. Baseline Simulation Results

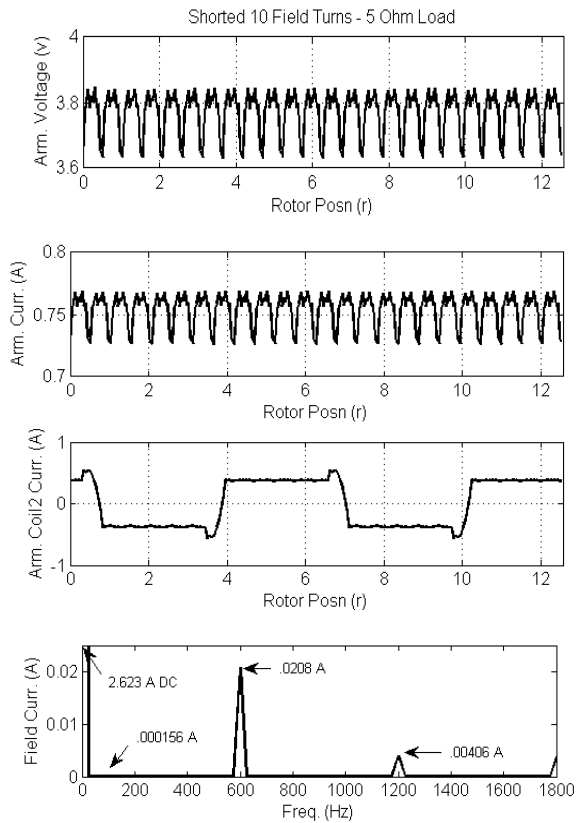


Figure 8. Simulation of Field-Winding Short

Since the induced armature voltage is also speed dependent, the transfer impedance is normalized relative to some reference speed, ω_r , so that the transfer impedance is calculated by

$$\frac{e_a}{i_f} \left(\frac{\omega}{\omega_r} \right) \quad (7)$$

where ω is the actual velocity.

Simulations of armature winding failures were then performed. Results for short-circuit (5.6% of armature turns) and open-circuit (single coil) armatures are shown in Figures 9 and 10, respectively. In both cases, there was a marked increase in the field current at the pole-passing frequency as compared to baseline performance. This increase also concurs with the results found by Glowacz & Zdrojewski [2]. Thus, the pole-passing frequency component of the field current is an observable parameter that indicates a possible armature-circuit problem. The pole-passing frequency is defined as the number of poles of the starter/generator multiplied by the rotational speed in revolutions per second:

$$\text{pole-passing frequency} = \omega (\# \text{ poles}). \quad (8)$$

The field current at the pole-passing frequency was obtained by performing an FFT on the field current and then determining the amplitude of field current at the pole-passing frequency.

Commutator segment faults were then simulated. A commutator segment that does not make contact with the brush was simulated with results shown in Figure 11. A significant pole-passing component (and harmonics) of field current was again developed as a result of this bad commutator segment. In addition, a field current component at the commutation frequency of 600Hz appeared. The commutation frequency, similar to the pole-passing frequency, uses the number of commutator segments on the machine:

$$\text{commutation freq.} = \omega \# \text{ commutator bars}. \quad (9)$$

Physically, the field winding contains useful information about commutation because the armature coils undergoing commutation (i.e., the coils shorted by the brushes) are well-coupled magnetically with the field winding. Since a short circuit across adjacent commutator segments is similar to a short-circuited armature coil, as shown in Figure 9, those results are not included here.

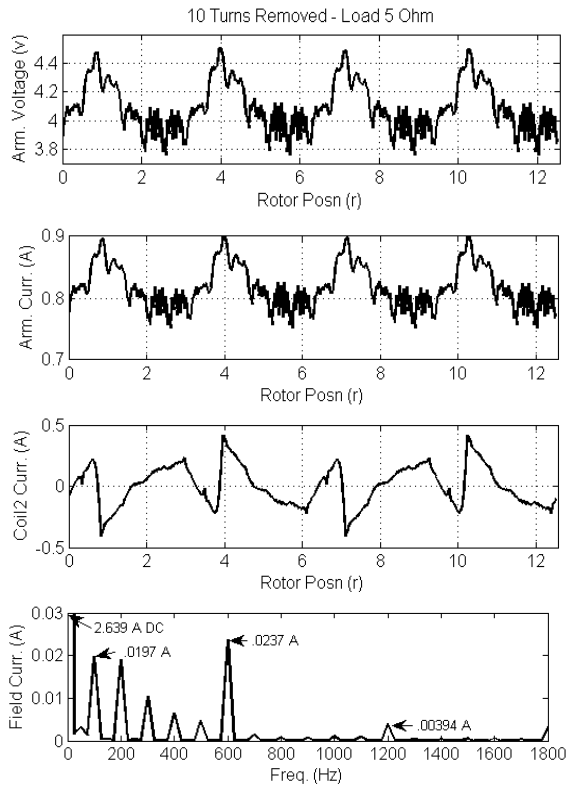


Figure 9. Simulation of Armature Short Circuit

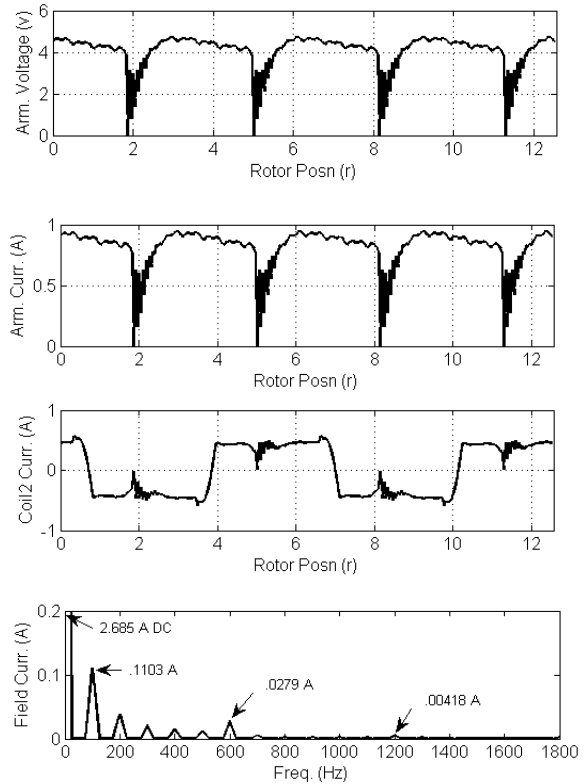


Figure 11. Open-Commutator Segment Simulation

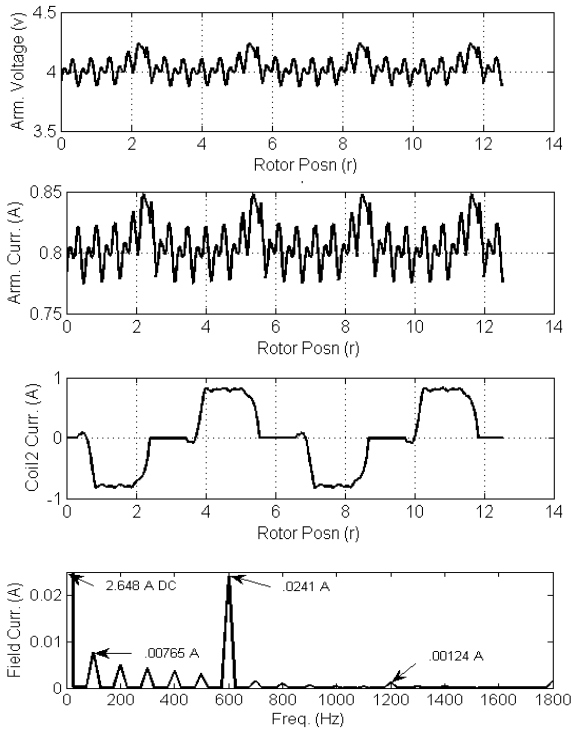


Figure 10. Simulation of Armature Open Circuit

Finally, simulations were performed to analyze increased brush resistance. This may occur for several reasons, such as decreased brush pressure or poor filming of the brush/commutator interface. The result of a 22% increase in brush contact resistance is shown in Figure 12. Though there is little visible difference between the baseline results and Figure 12, the transfer impedance was indeed reduced to 1.73 from its baseline value of 1.77 as brush resistance increases. Physically, this drop in transfer impedance occurs due to the increased drop in potential across the brushes. This effect is increasingly observable under higher load conditions.

The various faults and associated observables determined through the coupled FEA simulations are given in Table 2.

Seeded Fault Laboratory Experiments

As a follow-up to the FEA simulations, a series of laboratory experiments were performed on a DC machine to confirm the simulation results. For these tests, the faults used for simulations were, where feasible, seeded into the machine. For each case, a 4-pole DC machine with 72 com-

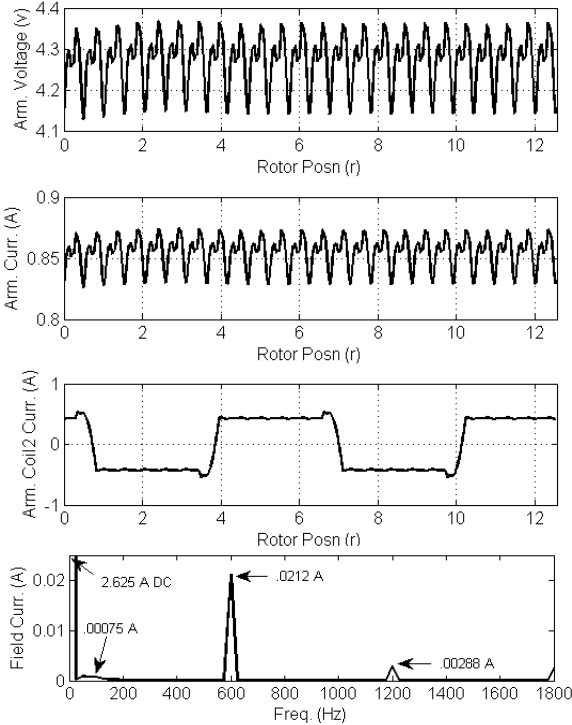


Figure 12. Increased Brush Resistance Simulation

mutator segments was operated at 1800RPM and a load of 12.5 ohms. Thus, the pole-passing frequency was 120Hz, and the commutation frequency was 2160Hz. Except for the shorted armature coil test, the output voltage was regulated to 120V. The armature of the DC machine used in these experiments is shown in Figure 13.

Table 2. DC Machine Fault Observables

Fault Type	Transfer Imped. (e/i_f)	i_f at pole-passing	i_f at comm freq.
Field Short	decrease	no change	no change
Arm Short	decrease	increase	no change
Arm Open	decrease	increase	no change
Bad Comm Seg	decrease	major increase	small increase
Comm Seg Short	decrease	major increase	no change
Brush Wear	slight decrease	no change	no change



Figure 13. Experimental DC Machine

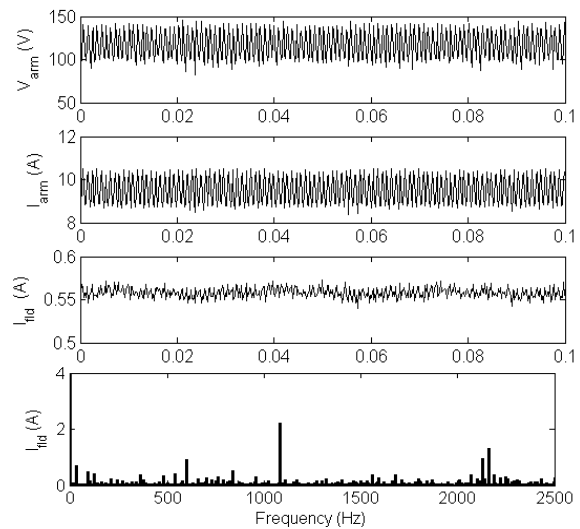


Figure 14. Experimental Baseline Results

Baseline operation of the experimental DC machine is shown in Figure 14. For baseline operation of this experimental DC machine, the transfer impedance was 217.3 ohms. Following the baseline test, a short circuit of approximately 10% of the field winding coils was established. The results, as shown in Figure 15, demonstrate that in order to maintain the nominal output voltage of 120V, a much higher field current is required. This yields reduced transfer impedance as predicted by the FEA. Specifically, the transfer impedance in this case drops to 180 from its baseline of 217.3.

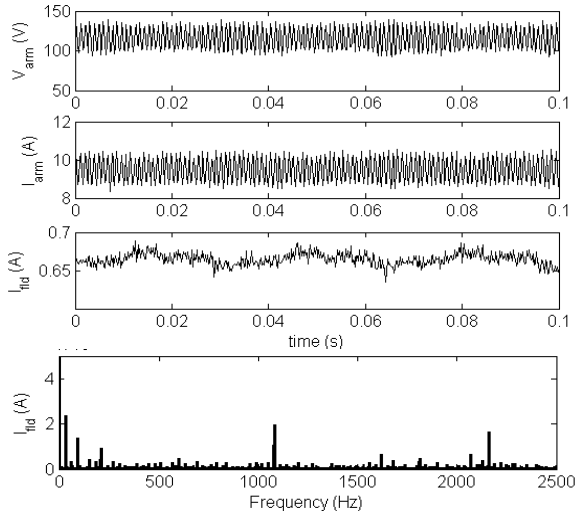


Figure 15. Field-Winding Fault Experiment

Shorted armature coil experimental results are shown in Figure 16. For this test, a reduced field current was used to avoid permanent damage to the armature due to high short-circuit currents. Despite the reduced output voltage, the results clearly show an elevated component of field current at the pole-passing frequency of 120Hz. This result concurs with FEA simulation results.

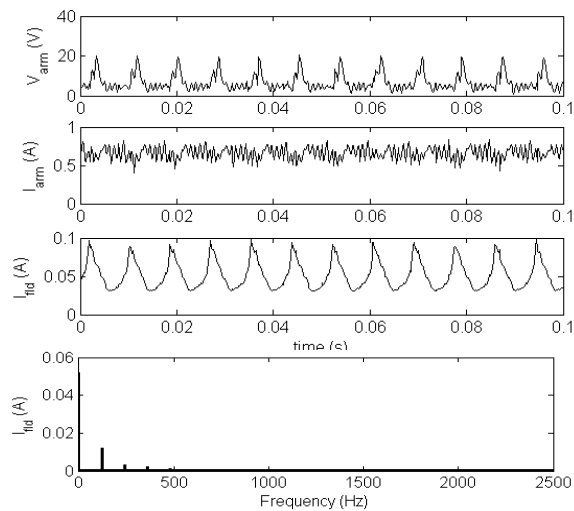


Figure 16. Armature Short Experiment

To increase overall brush resistance, the brushes were intentionally compromised, as shown in Figure 17. With these worn brushes, the machine was again run in generator mode under the same conditions. Very little change in the armature or field currents was evident when compared with the baseline; however, the transfer impedance dropped from

the baseline value of 217.3 to 208. This effect was also predicted by the coupled FEA simulations.

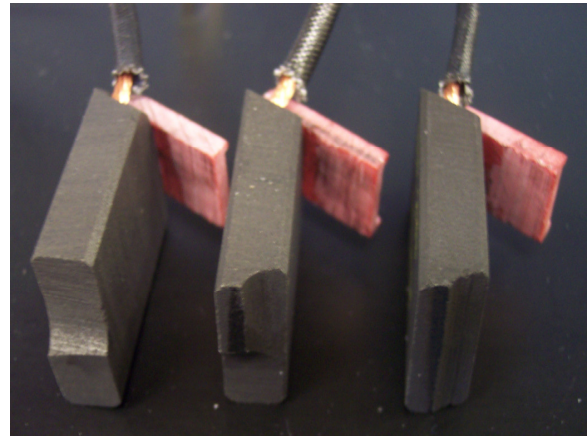


Figure 17. Compromised Brushes

Conclusions

A method for detailed analysis of the brushed DC machine operating under fault conditions was presented. The proposed method has been used to analyze the brushed DC machine under conditions including armature short circuit and open circuit, short-circuit field winding, bad commutator segment, and brush degradation. From these simulations, several important parameters were identified that may indicate the onset of DC machine faults. Those parameters are the transfer impedance and the field-current component at both the pole-passing and commutation frequency. Laboratory seeded fault tests on a DC machine were then used to confirm the effect of various faults on the identified observables. The results of this study can be used as a starting point for a predictive diagnostics implementation for DC machinery.

The views and conclusions contained in this document are those of the authors and should not be interpreted as representing the official policies, either expressed or implied, of the Aviation Applied Technology Directorate or the United States Government.

Acknowledgements

This work was partially funded by the Government under Agreement No. W911W6-07-2-0003. The U.S. Government is authorized to reproduce and distribute reprints for Government purposes notwithstanding any copyright notation thereon.

References

- [1] Z. Glowacz, and A. Zdrojewski, "Mathematical Modeling of Commutator DC Motor in Failure Conditions," *5th IEEE International Symposium on Diagnostics for Electric Machines, Power Electronics, and Drives (SDEMPED)*, 2005, pp. 1-5.
- [2] Z. Glowacz, and A. Zdrojewski, "Diagnostics of Commutator DC Motor Basing on Spectral Analysis of Signals," *IEEE International Symposium on Diagnostics for Electric Machines, Power Electronics, and Drives (SDEMPED)*, 2007, pp. 497-500.
- [3] R. Retana, A. Paweletz, and H. Herzog, "Analysis and Detection of Short Circuits in Fractional Horsepower Commutator Machines," *IEEE Trans. on Energy Conversion*, vol. 23, no. 2, pp. 484-491, June 2008.
- [4] M. Liu, X. Yang, and S. Cui, "Online Fault Detection and Diagnosis of Permanent-magnetic DC Motor," *IEEE Vehicle Power and Propulsion Conf.*, 2008, pp. 1-5.
- [5] G. Kliman, and D. Song, "Remote Monitoring of DC Motor Sparking by Wavelet Analysis of the Current," *IEEE International Symposium on Diagnostics for Electric Machines, Power Electronics, and Drives (SDEMPED)*, 2003, pp. 25-27.
- [6] S. Barwany, and G. Thomas, "A Non-intrusive System (SMS) to Monitor Sparking Along the Brush/Commutator Interface of a DC Machine," *5th International Conference on Electrical Machines and Drives*, 1991, pp. 72-76.
- [7] R. Wang, and R. Walter, "Modeling of Universal Motor Performance and Brush Commutation Using Finite Element Computed Inductance and Resistance Matrices," *IEEE Transactions on Energy Conversion*, vol. 15, no. 3, pp. 257-263, 2000.
- [8] D. C. Meeker, Finite Element Method Magnetics, Version 4.0.1, <http://www.femm.info>
- [9] K. Sawa, H. Yamamoto, and K. Miyachi, "Analysis of Armature Circuit Inductance of DC Machines by FEM," *IEE Proceedings on Electric Power Applications*, vol. 132, no. 6, 1985, pp. 307-314.

Biographies

TODD D. BATZEL received a BS in electrical engineering from Pennsylvania State University in 1984, an MS in electrical engineering from the University of Pittsburgh in 1989, and a PhD in electrical engineering in 2000 from Pennsylvania State University. He is currently an associate professor of electrical engineering at Penn State Altoona. His research interests include machine controls, electric

drives, and artificial intelligence. Dr. Batzel may be reached at tdb120@psu.edu

NICHOLAS C. BECKER is currently a fourth-year student in the electro-mechanical engineering technology program at Penn State Altoona.

MIHAI COMANESCU received his BSEE from Bucharest Polytechnic University in 1992 and his MS and PhD from Ohio State University in 2001 and 2005, respectively. He is currently an assistant professor of electrical engineering at Penn State Altoona. His research interests are power electronics, AC drives, and motion control systems.

ENERGY HARVESTING WITH PIEZOELECTRIC FIBER COMPOSITE FROM MECHANICAL VIBRATIONS

Faruk Yildiz, Sam Houston State University

Abstract

The use of Piezoelectric elements has not been very successful for energy-harvesting systems even though there have been many research studies in this area. This does not mean that piezoelectric materials are not capable of energy harvesting, but more advanced piezoelectric materials are needed to increase the efficiency of ambient energy-harvesting systems. ACI (Advanced Cerametrics Incorporated) has recently developed Piezoelectric Ceramic Fiber Composites (PFC) for energy-harvesting systems. The PFC consists of uniquely flexible ceramic fiber capable of capturing waste ambient energy from mechanical sources such as vibrations, motion, and bending via the piezoelectric effect. This device functions between ambient vibration sources and an electrical circuit with a storage device to convert mechanical vibrations into electrical energy. This unique development allows some applications to be powered without the need for battery power such as wireless sensors, transmitters, microcircuits, smartcards, cell phones or other handheld devices. For the purpose of energy harvesting and storage, shoe or sneaker insoles, surplus vibrations from industrial machinery, shuddering railway cars, flexing joints, and even the stomp of city's rush-hour commuters could all be tiny, renewable sources of power. These are good sources of mechanical stress, deformation, and vibration since mechanical motion exists to generate low power. In this study, a piezoelectric fiber composite bimorph (PFCB) was investigated and tested to show that potential energy generation capacity depends upon source characteristics by implementing an energy-harvesting circuit.

Introduction

A piezoelectric energy-harvesting method converts mechanical energy into electrical energy by straining a piezoelectric material [1]. Strain or deformation of a piezoelectric material causes charge separation across the device, producing an electric field and, consequently, a voltage drop proportional to the stress applied. The oscillating system is typically a cantilever beam structure with a mass at the unattached end of the lever, since it provides higher strain for a given input force [2]. The voltage produced varies with time and strain, effectively producing an irregular AC sig-

nal. The piezoelectric energy conversion produces relatively higher voltage and power density levels than the electromagnetic system. Moreover, piezoelectricity has the ability to generate an electric potential of elements such as crystals and some types of ceramics from a mechanical stress [3].

If the piezoelectric material is not short-circuited, the applied mechanical stress induces a voltage across the material. There are many applications based on piezoelectric materials, such as electric cigarette lighters. In this system, pushing the button causes a spring-loaded hammer to hit a piezoelectric crystal and the high voltage produced jumps across a small spark gap, thus igniting the flammable gas. Following the same idea, portable sparkers are used to light gas grills and stoves, and a variety of gas burners have been built in piezoelectric-based ignition systems.

In a study conducted recently by Marzencki [4] to test the feasibility and reliability of different ambient vibration energy sources, three different vibration energy sources including electrostatic, electromagnetic, and piezoelectric were investigated and compared according to their complexity, energy density, size, and problems encountered (Table 1).

Table 1. Comparison of vibration energy-harvesting techniques

	Electrostatic	Electromagnetic	Piezoelectric
Complexity of process flow	Low	Very High	High
Energy density			
Current size	4 mJ cm ⁻³ Integrated	24.8 mJ cm ⁻³ Macro	35.4 mJ cm ⁻³ Macro
Problems	Very high voltage and need of adding charge source	Very low output voltages	Low output voltages

The problem of how to get energy from a person's foot to other places on the body, for example, has not been suitably solved. For a Radio Frequency Identification (RFID) tag or other wireless device worn on the shoe, the piezoelectric

shoe insert offers a good solution. However, the application for such devices is extremely limited and, as mentioned earlier, not very applicable to some of the low-powered devices such as wireless sensor networks. Active human power, which requires the user to perform a specific power-generating motion, is common and may be referred to separately as active human-powered systems [5].

An example of energy harvesting using unimorph piezoelectric structures was conducted by Thomas, Clark and Clark [6]. This research focused on a unimorph piezoelectric circular plate which is a piezoelectric layer assembled to an aluminum substrate. The vibrations were driven from a variable ambient pressure source such as a scuba tank or blood-pressure meter. The researchers showed that by creating the proper electrode pattern on the piezoelectric element (thermal “regrouping”), the electrode was able to produce an increase in available electrical energy. In the system, as the cantilever beam vibrates, it experiences variable stresses along its length. Regrouping the electrodes targeting specific vibration modes resulted in maximum change collection. This type of design may add possibilities for miniaturization and practicality to piezoelectric energy-harvesting technology.

The piezoelectric active fiber composites (AFC) are made by Advanced Ceramics Incorporated (ACI) [7] from a uniquely-flexible ceramic fiber that was able to capture wasted ambient energy from mechanical vibration sources and convert it into electric energy. The piezoelectric fiber composites’ fiber lines are capable of generating electricity when exposed to an electric field. In piezoelectric fiber composite bimorph (PFCB) architecture, the fibers that are suspended in an epoxy matrix and connected using inter-digitized electrodes create the AFC. It is already known through tests by the manufacturing company that thin fibers with a dominant dimension, a length, and very small cross-sectional area are capable of optimizing both the piezo and the reverse piezo effects. The amount of energy produced by mechanical-to-electrical energy conversion through the PFCB is much better than that compared to other piezoelectric materials, according to the ACI’s internal studies. An investigation into the improvement of performance and efficiency, using a PFCB, of an energy-harvesting system was considered. The PFCB characteristics and properties were intensively studied in order to build an efficient energy-harvesting circuit for further study. The power generation efficiency of the PFCB depending on various input vibrations was measured by building an operational difference amplifier instrumentation test circuit. Only one type of piezoelectric element, which is PFCB, was available to test with a small constant shaker. The shaker functioned as an ambient vibration source (passive human power) and was

used to shake the PFCB to produce electricity for the energy-harvesting circuit.

Since cycle durability of fiber composites was determined by the manufacturer, the life-cycle test of the PFCB material was ignored in this research. Manufacturer cycle tests show that fiber composite materials are extremely durable and are able to handle one billion cycles without any degradation of properties. Materials efficiently generated constant continuous power during the tests. [7].

The PFCB was tested by itself by flicking the tip with a mechanical pencil without any mass attached. The power output signal characteristics were observed using an oscilloscope and multimeter. A photograph of the PFCB with the inter-digitized electrodes to align the field (energy-harvesting circuit) with the fibers is shown in Figure 1.



Figure 1. Basic specifications of the PFCB

In the next sections, the PFCB energy source is modeled as a steady AC power source for the circuit components for the energy-harvesting circuit. This AC source was then converted to DC voltage since all the electronic components for the energy-harvesting and battery-charging circuits required a DC voltage source to operate.

Power Characteristics

A piezoelectric energy source is most often modeled as an AC voltage source because of its AC power characteristics when excited with periodic vibration. Piezoelectric fiber composites can be connected in series with the capacitors and resistors to reduce or smooth the high-voltage input produced by PFCB. The simple connection diagram architecture of the piezoelectric material with a capacitor, resistor and load (representing a storage unit) is shown in Figure 2. The AC-DC conversion circuit is not included in this diagram since it is explained in detail in subsequent sections.

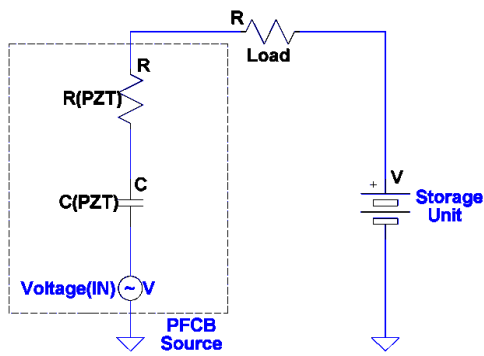


Figure 2. PFCB as a sinusoidal (AC) voltage source

Because of budget and equipment restrictions, the author was not able to purchase a variable-frequency shaker to test the PFCB and the system with different frequencies. Only a shaker (115V at 60Hz) was used as a constant vibration source. The tip of a mechanical pencil was used to flick the tip of the PFCB product in order to provide the initial disturbance for test purposes. The instruments used for testing included a multimeter, a shaker, and an oscilloscope to take voltage readings from the PFCB. The first test for voltage output depended on time variation and was conducted without any mass placed on the tip of the PFCB. This was followed by a test with variable masses that were placed on the tip of the PFCB to observe the output voltage levels.

The more mass added on the tip of the PFCB, the more time passed until vibration of the PFCB stopped. At the same time, the voltage from the PFCB increased depending on the mass and the force applied to the tip of the PFCB. The plots in Figure 3 are a summary of the peak-to-peak voltage levels and the corresponding time for 2.5gr, 5gr, 7.5gr, and 10gr (gram) masses, respectively, added onto the tip of the PFCB to increase the decay of vibration. The AC signals and voltage outputs were similar to each other; however, the time required for the vibration to decay was observed to be longer with more masses attached to the PFCB. The signal ringing lasted longer than the entire time captured on the oscilloscope. However, it was observed that the time until vibration stops is longer with more mass attached to the PFCB. The resonant frequency does not depend upon the pencil flicks but rather upon the mass (including distributed mass and lumped tip mass) and the distributed spring constant of the cantilevered beam. For a sinusoidal excitation, the most energy is transferred when excited at the resonant frequency. The decay depends upon the input resistance of the measuring device (electrical damping) and the mechanical damping from the material and from the air.

Furthermore, the output voltage produced by the PFCB was observed mainly above 300V, as specified by the PFCB

manufacturer. The obtained voltage level is an open-circuit voltage and would decrease any time a load is connected between the inter-digitized electrodes of the PFCB. The power outputs of the PFCB are discussed more in the energy-harvesting circuit design section with the supporting simulation outputs.

The PFCB was carefully clamped on the table with plastic bumpers to avoid damaging the part during its vibrations. The wiring between all modules was done carefully to allow reading of the voltage outputs from the oscilloscope and multimeter displays. The overall test system used for the experiment is shown in Figure 4.

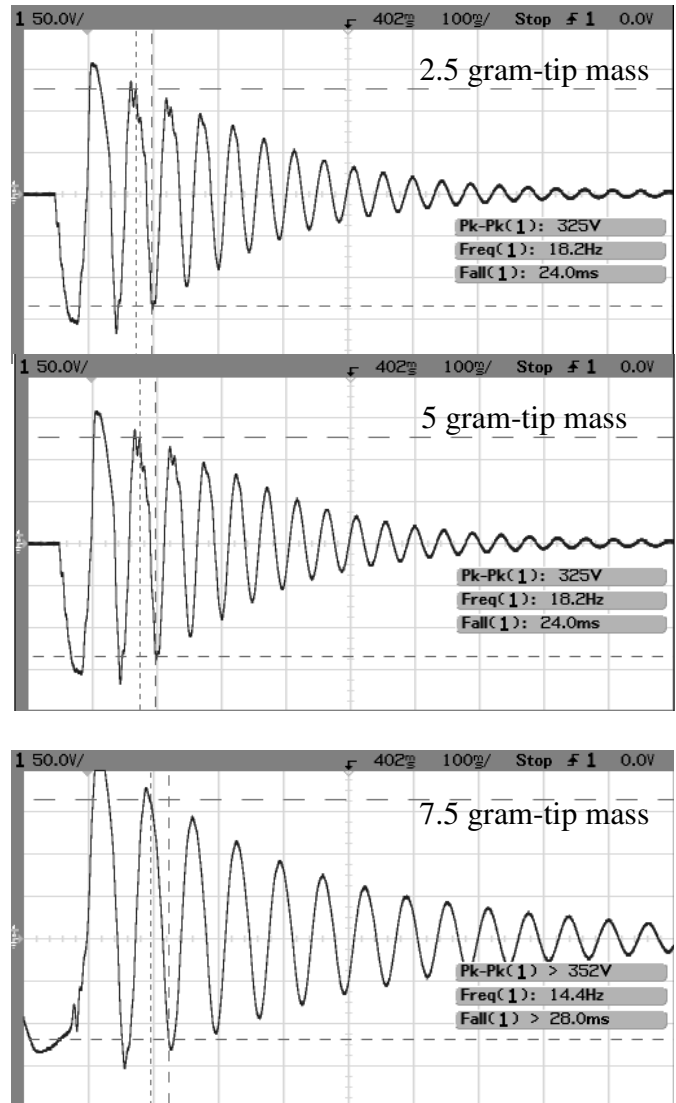


Figure 3. Plots of voltage decay of the open circuit PFCB configuration

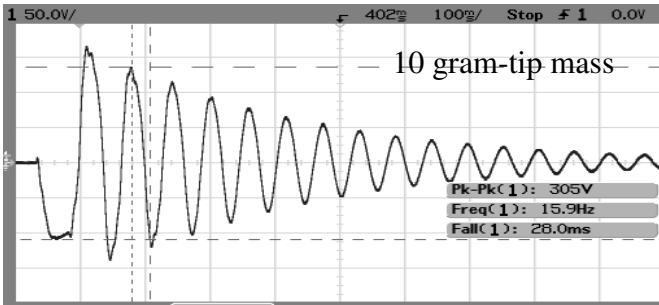


Figure 3 continued: Plots of voltage decay of the open circuit PFCB configuration

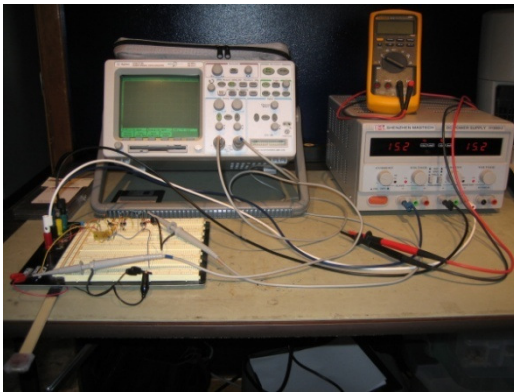


Figure 4. The test fixture to test power characteristics of the PFCB

The PFCB layer and material properties were not known accurately enough in order to predict the frequency rate, so the value had to be determined experimentally on the test fixture. To allow a calculation of the current output, wires from the PFCB electrodes were connected to the oscilloscope probes through a 1kohm resistor. The current outputs could not be measured by a multimeter and were observed on the oscilloscope screen when the PFCB was vibrated by the shaker at 60Hz. It was not possible to plot the current and power outputs due to a lack of the proper data-acquisition system. However, there were very low current outputs produced that may be harvested with a proper energy-harvesting circuit. From the vibration test results, it was determined that with the variable frequency, the power generated from the PFCB is sufficient to be used to power low-power electronic devices. The obtained values would be enough to build an energy-harvesting circuit to charge a small-scale storage device such as a battery, capacitor or super capacitor, albeit slowly.

Energy-harvesting Circuit Design

After testing the power output and the working characteristics of the PFCB at different stretches and attached

masses, the author built the energy-harvesting circuit used to charge the batteries under low current levels. The mechanical-to-electrical energy conversion is usually managed by the energy-harvesting circuits, including conventional buck-boost converters, bridge rectifiers, and battery-charging circuits [8-11]. The energy-harvesting circuit was designed, developed, and built according to the ambient source and piezoelectric fiber composites' low-current constraints in order to produce efficient power output.

The following energy-harvesting and battery-charging circuit design was built with typical components that could decrease high-input voltages and increase low-input currents from the PFCB in order to provide sufficient charge currents to the batteries. The circuit was designed to start charging when the battery voltage drops below a nominal value, and stops charging when voltage reaches the battery's nominal voltage. The LTSPICE simulation interface that shows the overall circuit is depicted in Figure 5. It represents the system circuit modules which are simulated together to test the output power level of the circuit [12]. All of the necessary simulations were conducted using SwitcherCAD™ Spice III because of the Linear Technology based DC-DC buck-boost converter and battery-charging circuit components [13]. Initially a full-wave bridge rectifier was added to the energy-harvesting circuit. A full-wave bridge rectifier is very efficient, converting positive and negative cycles from the PFCB and supplying DC voltage to the battery through the battery-charging part of the energy-harvesting circuit. Since the current produced from the PFCB was low, an intermediate operational amplifier (op amp) circuit was placed on the energy-harvesting circuit to increase the current levels for test purposes [14]. This instrumentation circuit consisted of operational amplifiers, resistors, and intermediate/storage capacitors to implement the circuit at $\pm 15V$, which was supplied by an external power source. A buck-boost converter and battery-charging circuit is shown as the last part of the simulation interface before the storage unit.

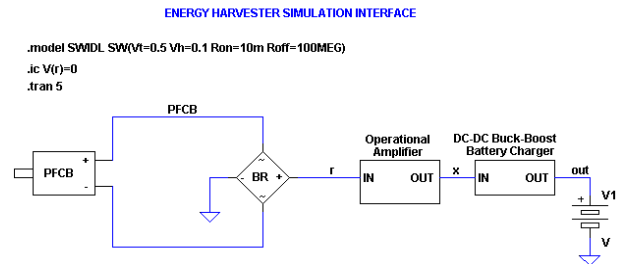


Figure 5. Energy-harvesting circuit-simulation interface

The pump part of the energy-harvesting circuit consists of three single operational amplifiers that are configured as difference amplifiers. This demonstrates that the voltage differential between the two branches is the output of the circuit. The pump instrumentation circuit is shown in Figure 6. This pump instrumentation circuit design is used to observe voltage outputs from the PFCB and the capacity changes of the capacitors when the PFCB was being vibrated. The capacitors (C1 and C11) were charged depending on how much voltage generated by the PFCB was observed by the oscilloscope through the operational-amplifier instrumentation circuit.

The general operational amplifier in Figure 6 was used to observe the charging phase of the C11 intermediate storage capacitor. An initial voltage of 5V was supplied across capacitors in both circuits. In circuit A, the voltage across the capacitor with the 10Mohm impedance, which was representing a flux digital multimeter, was measured. The voltage across the capacitor (C1) dropped almost 2V when the circuit was simulated at the same input voltage. However, the voltage across the capacitor (C11) in the operational-amplifier circuit stayed relatively constant. The voltage level across both capacitors (C1 and C11) was simulated and is plotted in Figure 7 in order to compare voltage drops across the capacitors.

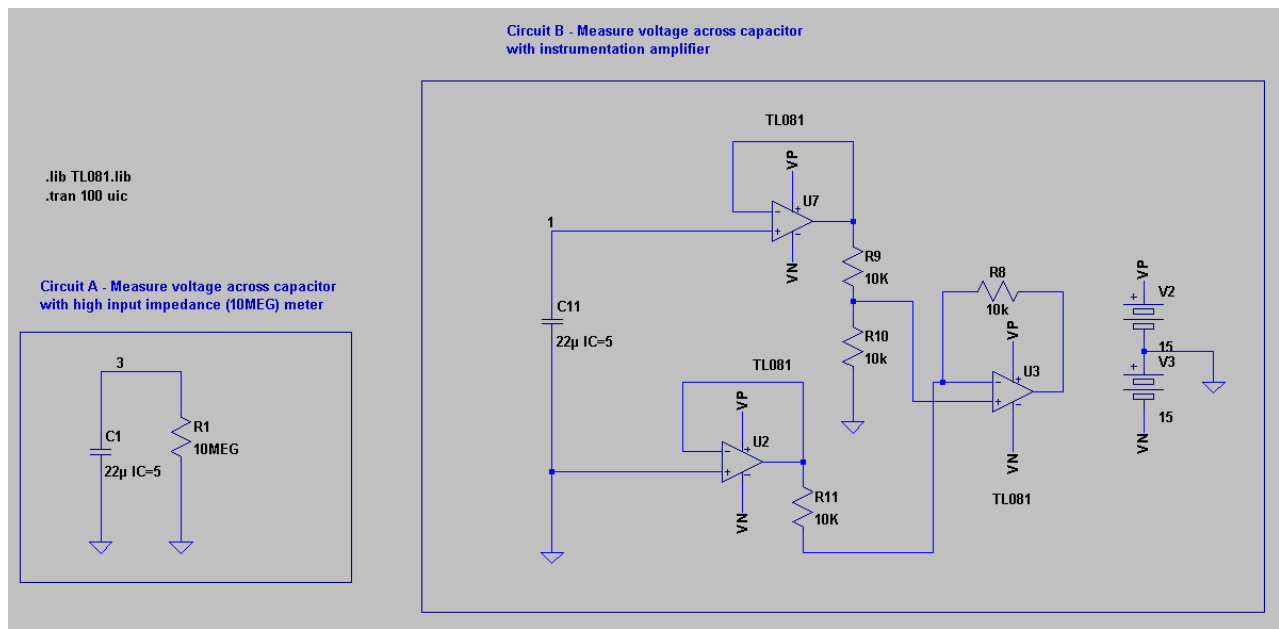


Figure 6. Operational Amplifier instrumentation circuit

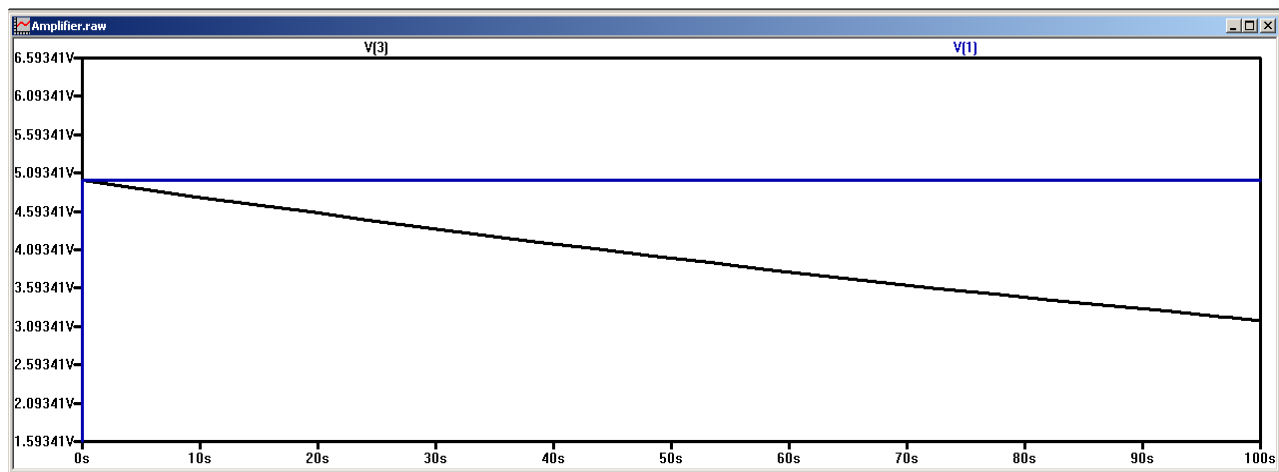


Figure 7. Voltage levels across intermediate storage capacitors

When the PFCB was placed on the constant shaker, it started generating voltages and charging the capacitors. The operational-amplifier circuit kept the initial voltage level constant to allow for accurate reading of the voltage levels of the intermediate storage capacitor. In circuit A, the voltage readings would not be accurate because of the voltage drops across the capacitor when measuring the voltage with a digital multimeter. However the capacity readings across capacitor C11 would be accurate since the operational amplifier keeps the initial voltage level constant.

DC-DC Buck-Boost Converter and Battery-charging Circuit

DC-DC converters efficiently step-up (boost), step-down (buck) or invert DC voltages without the necessity of transformers. In these structures, switching capacitors are usually utilized to reduce or to increase physical size requirements. DC-DC converters allow product size reduction for portable electronic devices where increased efficiency and regulation of input power are necessary for optional requirements.

Taking the above features of the buck-boost converters into consideration, a linear-technology-based LT1512 DC-DC buck-boost SEPIC constant-current/voltage battery-charging integrated circuit was used to regulate the high output voltage that was produced from the PFCB to charge small-scale batteries for test purposes [15]. An LT1512 battery-charging circuit was added to the energy-harvesting circuit. Since buck-boost converters are very sensitive, proper design in conjunction with supporting components and physical layout is necessary to avoid electrical noise generation and instability.

Considerations for LTSPICE modeling, converter selection, circuitry building, debugging, and power-output improvements were followed step-by-step in order to create a good energy-harvesting circuit.

This circuit would maximize the power flow from the piezoelectric device and was implemented in coordination with a full-wave bridge rectifier, intermediate storage capacitor, and voltage-sensitive switching circuit. It was observed that when using the energy-harvesting circuit, over twice the amount of energy was transferred to the battery than with direct charging alone. However, if the power-harvesting medium produced less than 2.7V, power flow into the battery was reduced due to losses in the additional circuit components and the threshold characteristics of the LT1512. For the purpose of storing energy in the intermediate storage unit, a capacitor was placed before the voltage-sensitive circuit and buck-boost converter. The voltage-sensitive circuit consists of diodes (including Zener diodes),

MOSFET switches, and resistors to transfer the energy from an intermediate capacitor to the battery through a DC-DC buck-boost converter [16]. The MOSFET switches and Zener diodes on the voltage-sensitive circuit sense the voltage in the intermediate capacitor and transfer the energy when the capacitor reaches specific voltage levels. The voltage level in the intermediate capacitor is controlled by the Zener diodes until the capacitor is discharged by transferring its energy to the battery.

Depending on the Zener diode values, the stored energy in the capacitor is transferred to the storage unit through the DC-DC buck-boost converter and battery-charging circuit. Due to known high-discharge rates of the capacitors, the Zener diode voltage values chosen were 12V and 6.2V (which are small values for the purpose of energy harvesting from PFCB) in order to avoid losing stored energy in the intermediate capacitor. One of the most important benefits of the intermediate capacitor and voltage-sensitive switching circuit is the increase in the amount of transferred energy from the PFCB. There is a reduction in the circuit loss throughout the energy-harvesting circuit caused by the electronic components. The circuit is shown in Figure 8 and was built in four phases to represent the overall energy-harvesting circuit modules in order to simulate the circuit.

The first module is a mechanical-to-electrical energy-conversion module and functions the same as a PFCB producing AC power.

The second module has rectification (the conversion of AC voltage to DC voltage) and an energy-storage unit (intermediate capacitor). The third module is a voltage-switching circuit which senses the voltage level of the intermediate capacitor and transfers it to the battery through a DC-DC buck-boost converter and battery-charging circuit. The fourth module is the model of a buck-boost converter and battery-charging circuit representing exact characteristics of the LT1512 SEPIC constant-current/voltage integrated circuit, which will be discussed in subsequent sections.

The circuit shown in Figure 8 was simulated using LTSPICE (SwitcherCAD III). Mechanical energy is converted into electrical energy by the piezo, and is rectified and stored as charge on a capacitor. When the storage capacitor voltage $V(\text{in})$ reaches 15V, the voltage sensitive switch turns on allowing the energy stored on the capacitor to be transferred to the buck converter which charges the battery. As the capacitor charge is transferred to the battery, the storage capacitor voltage will decrease until it reaches the lower threshold (about 8V), at which time the voltage-sensitive switch will turn off. Now, the storage capacitor voltage will start increasing again as mechanical energy is

converted into electrical energy, and the cycle will repeat. The charge and discharge steps are repeated while the PFCB produces electricity from the vibrations.

The DC-DC converter and battery-charging circuit design, which is part of the energy-harvesting circuit simulation interface, is shown in Figure 10. This circuit simulation interface is employed to handle the decrease or increase in voltage levels and keep it constant according to the battery specifications. The voltage output of the circuit can be easily modified by using different resistance values if a different battery is integrated with the system.

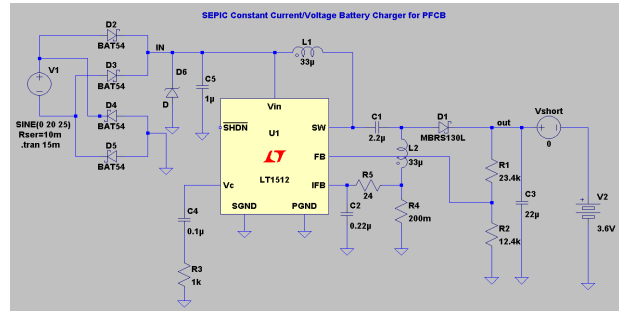


Figure 10. Energy-harvesting and charging circuit

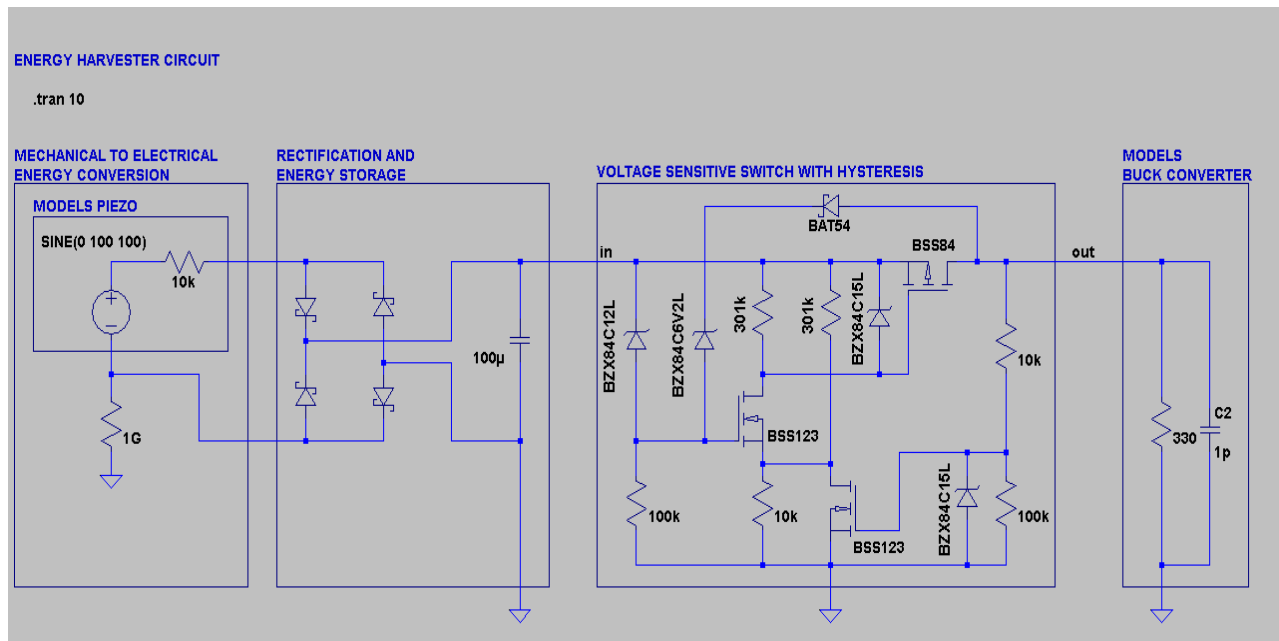


Figure 8. Intermediate voltage-sensitive switch with hysteresis

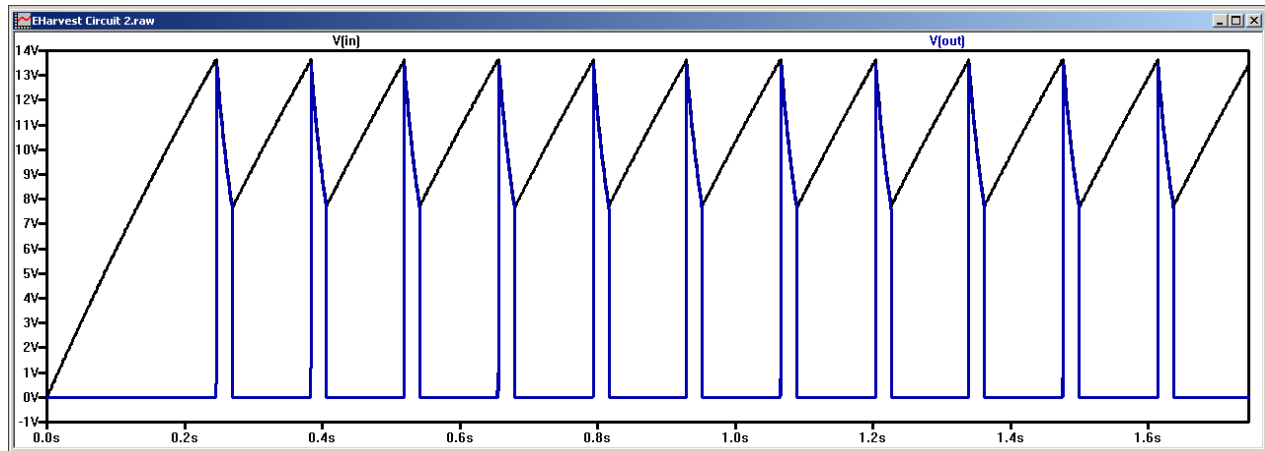


Figure 9. Voltage input and output simulation of voltage-sensitive switch

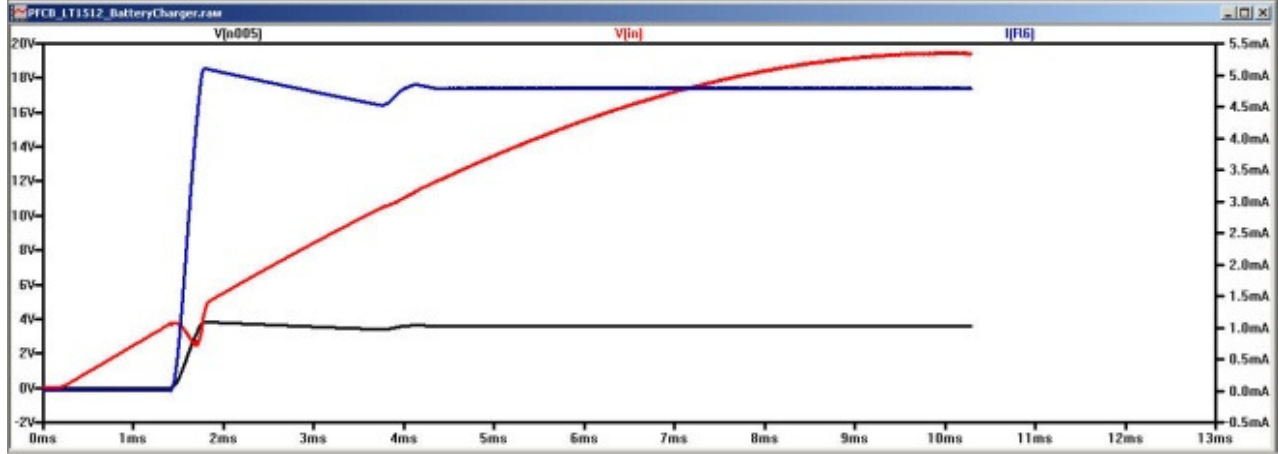


Figure 11. Battery-charging values simulation

Circuit Simulation

The simulation graph of the major circuit components through the LT1512 SEPIC battery-charging circuit (including input voltage, battery-charging voltage and current) were simulated and are depicted in Figure 11. All three important aforementioned parameters of the energy-harvesting and battery-charging circuit were simulated together to examine the consistency of the voltage/current levels on the circuit design simulation interface, shown in Figure 11.

The input-voltage (V_{IN}) simulation plot was generated by the vibrations through the PFCB while being shaken as shown. This voltage level was measured after rectification of the AC voltage signal, which came from the PFCB unit as a DC voltage and served as the input for the buck-boost converter and the voltage-regulator circuit. Since the maximum input voltage of an LT1512 integrated circuit is $30V_{MAX}$, a Zener diode was placed between V_{IN} and the ground of the LT1512 in order to avoid damaging the internal components of the LT1512.

The input voltage (V_{IN}) and regulated battery-charging voltage (V_{OUT}) were compared in order to check the input and output voltage differences after regulation. The input voltage levels that were greater or less than 3.6V were regulated by the LT1512 buck-boost converter and the battery-charging IC (Integrated Circuit) in order to charge the battery at the nominal voltage level which is 3.6V at 60mAh for the test battery.

The battery-charging current (I_{ROUT}) and battery-charging voltage (V_{OUT}) simulation plots are depicted to indicate battery-charging values. Both voltage and current

levels were supplied at a steady state for proper battery charging $I_{ROUT} = 5mA$ (which is a standard charging current for the battery) and $V_{OUT} = 3.6V$ nominal charging voltage. The charging current that was generated by the PFCB was less than 1mA but was increased to 5mA by the intermediate capacitors.

The intermediate capacitors were charged to the minimum charging threshold of the battery and then released to the battery terminals by discharging themselves to allow them to accept charge voltages from the PFCB again. However, the current level was not able to increase sufficiently to charge the battery because of the low current produced by the PFCB. The specific voltage and current levels that are specified in the simulation plot can charge at 3.6V at 60mAh for a fully discharged battery in approximately 27hrs with constant vibrations from the PFCB.

Building the Circuit

An energy-harvesting and charging-circuit was designed to charge small-scale NICD and NIMH batteries at the constant charging phase. The printed circuit board for the energy-harvesting circuit was designed and built as small as possible to fit even small places for power generation including the battery soldered on the circuit. However, for test purposes, the instrumentation circuit on the bread board and the energy-harvesting circuit were placed near the measuring equipment with the PFCB assembled to allow for reading of output values on the oscilloscope display. The energy-harvesting circuit which is soldered on the printed circuit board is shown in Figure 12.

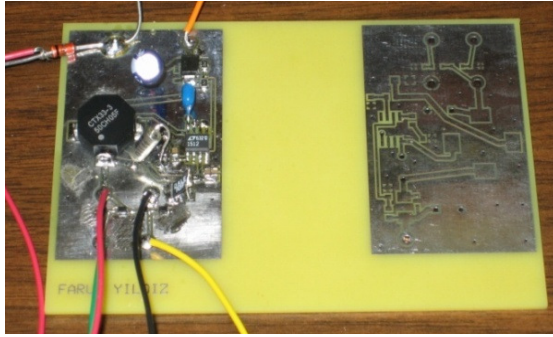


Figure 12. Energy-harvesting, conversion, and charging circuit

This circuit can be designed and built smaller, but appropriate tools should be used during the soldering process of the very small electronic components. The dimensions of the energy-harvesting circuit design on the PCB are small enough to allow it to be easily mounted in a small place, including the storage unit soldered on the circuit. However, a protective box should be designed and built to protect the circuit components and the battery from bending and experiencing deformations from the vibration sources.

Storage-unit Tests

One problem that was encountered when using power-harvesting systems was that the power produced by the piezoelectric material was often not sufficient to power most electronics. Therefore, methods are needed to accumulate the energy in an intermediate storage device so that it may be used as a power source. The method typically used to accumulate the energy is a capacitor. However, capacitors have characteristics that are not ideal for many practical applications such as limited capacity and high leakage rates. For the purpose of intermediate storage units, typical capacitors were used in the energy-harvesting circuit without causing any critical issues. A number of capacitors were connected in parallel with the resistors in order to smooth the delivered voltage, making the output voltage easily readable by the multimeter. Using the approximate displacement and frequency levels, the stored energy in the capacitors could be calculated.

Displacement of PFCB: 4mm;
PFCB Voltage: 350V; and
Capacitor value: 400 μ F

The 400 μ F capacitor bank was charged to 50V in about 4 seconds by PFCB on a constant-frequency shaker generating 350V. Taking the test results into consideration, the energy stored in the capacitors was:

$$E = \frac{1}{2} C.V^2 = \frac{1}{2} (400\mu F)(50V)^2 = 0.5J$$

Then, 0.5J of energy would produce 1/8W (0.125W) of power in 4 seconds as calculated here:

$$P = \frac{d}{dt} E = \frac{E}{\Delta t} = \frac{0.5J}{4Second} = \frac{1}{8} W (0.125W)$$

It was assumed that 125mW of energy would be sufficient to power a variety of low-power wireless or portable electronic devices. The calculations above are valid if the PFCB is constantly shaken or vibrations are applied to the PFCB material. According to the manufacturer's test results (ACI), E=880mJ of energy can be stored in 13 seconds as a result of the PFCB vibrations. Taking the stored energy into consideration, the average output power and current levels at different voltages were calculated as

E=880mJ;
 Δt =13sec;

$$P_{AVG} = \frac{E}{\Delta t} \quad (3)$$

where

P_{AVG} =Average power;
E=Energy stored;
 Δt =Time takes to store the energy;

$$P_{AVG} = \frac{880mJ}{13sec} = 67.69mW$$

V_{RMS} =0.1V, 0.2V... 10V;

$$I_{RMS}(V_{RMS}) = \frac{P_{AVG}}{V_{RMS}} \quad (4)$$

$$I_{RMS}(4V) = \frac{67.69mW}{4V} = 16.92mA$$

$$I_{RMS}(3V) = \frac{67.69mW}{3V} = 22.56mA$$

The current levels for battery-charging purposes were calculated according to the input voltage levels. If the input voltage is increased, the output current would automatically increase, thereby decreasing the battery-charging time. All

the calculations were done according to the energy stored in 13 seconds (as reported by tests). The graph in Figure 13 compares voltage and current levels and average power output in 13 seconds.

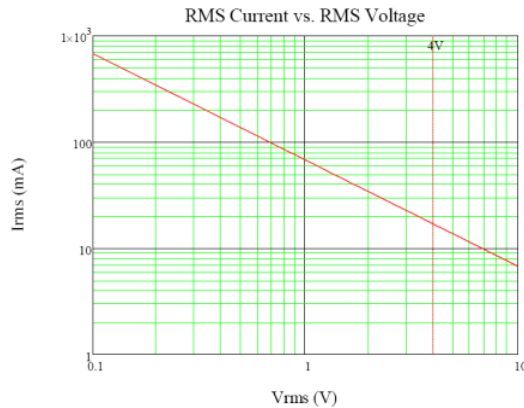


Figure 13. RMS Voltage/Current comparison for energy stored in thirteen seconds in capacitors

When a resistive load is relatively large, the power output from the PFCB does not produce significantly more power. The results of using a larger capacitor to smooth the output voltage suggest that the size of the smoothing capacitor affects the amount of power that can be delivered to a resistive load (battery). This is attributed to the non-ideal behavior of the capacitor, which leads to internal losses. Following construction of the energy-harvesting circuit, NICD- and NIMH-type batteries were charged to determine the battery-charging time that could be effectively observed for each with a constant frequency. After testing the voltage levels of the PFCB using the capacitors, the PFCB was then tested with the batteries to observe its battery-charging efficiency. For this purpose, a permanent magnet shaker was used to induce vibrations; two rechargeable batteries and an energy-harvesting circuit were used for the experiment. A PFCB consisting of two active fiber composites (bimorph)

was clamped to a thin piece of metal of the constant shaker for the energy-harvesting experiment. The photograph of the battery-testing system is shown in Figure 14.

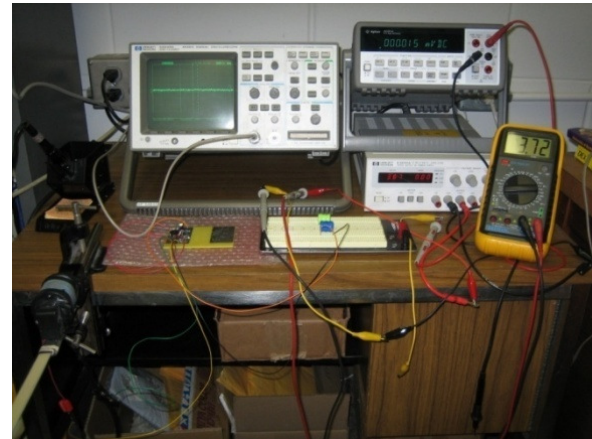


Figure 14. Battery-charging test fixture

The batteries used in the experiment are listed in Table 2 with the basic specifications that are needed as charging parameters. In order to charge batteries, the PFCB interdigitized electrodes were connected to the battery terminals through the energy-harvesting circuit.

The constant vibrations from the shaker were applied to the PFCB at 60Hz. The voltage measurements from the batteries were taken every hour and it appeared that the increase was very small. The reason for the slow charging was the very low current produced from the PFCB and the losses across the energy-harvesting and battery-charging circuit. Because of the low charging current, the test battery was not able to be charged at the specified standard charging time. However, this charging experiment was conducted with only a single PFCB, which is not recommended for charging batteries. In some applications, more than three PFCBs are connected in parallel to increase the current levels and efficiency of the energy-harvesting system. The number of

Table 2. Rechargeable battery specifications

Type	Name of Comp.	Nom. Voltage (V)	Ampacity (mAh)	Charge		Quick Charge		Charge time with PFCB (h)
				A (mA)	Time (h)	A (mA)	T (h)	
NIMH	Ps Sonic	1.2	80	8	15			47
NICD	Various	3.6	60	6	14	20	7	36
NIMH	Dantona Industry	3.6	60	6	14	20	7	41

PFCBs would be increased to charge the batteries in a specified time frame in order to avoid voltage drops across the batteries while powering the electronic device.

Furthermore, this experimental test showed that batteries can be charged with constant current/voltage in longer time frames than the specific time frame on the battery data-sheets. The last column in Table 2 shows the time required to charge the batteries with one PFCB. If more than one PFCB is used for the energy-harvesting system, charging time would be decreased considerably.

Discussion

Mechanical vibrations as an ambient energy source were considered as a possible energy source to generate electricity through a PFCB to charge low-scale rechargeable batteries. The batteries were expected to operate low-power electronic devices such as a radio, MP3 player, mobile phone or GPS unit. It was proven that the PFCB was able to produce enough voltage with low current as an input power to charge a small-scale rechargeable battery, depending on the time- and vibration-source characteristics. However, in the case of powering the electronic device, the batteries were placed in the system fully charged. It is essential to determine if the gained and stored power compensate for the consumption of the electronic device while it is operating. If the power produced compensates for the daily consumptions and the leakages of the electronic device, it could be said that vibrations as ambient energy sources are a feasible source for the electronic application.

Conclusion

The advances made from the work presented in this research will provide future researchers with the tools necessary to use PFCBs effectively in numerous applications. The sensing capabilities of the PFCB were investigated and its abilities were shown in an energy-harvesting system through an experiment and battery-charging circuit. The energy-harvesting circuit can be improved to increase current levels from the PFCB while decreasing voltage levels for battery-charging purposes. The increase of current during the vibration of the PFCB would decrease the battery-charging time by supplying more energy to the electronic device. Also, the PFCB can be placed around the door or in a hydraulic door closer to capture wasted human power. A special design would be constructed to create vibrations when the door is opened by human power. The special design should be located in a proper place where the most vibrations can be created for energy-harvesting purposes.

References

- [1] Sodano, H. A., Inman, D.J., & Park, G. (2004). A review of power harvesting from vibration using piezoelectric materials. *The Shock and Vibration Digest*, 36 (3), 197-205.
- [2] Roundy, S., Wright, P. K. (2004). A piezoelectric vibration based generator for wireless electronics. *Smart Materials and Structures*, 13, 1131-1142
- [3] Skoog, D. A., Holler, J. F., & Crouch, S. R. (2006). *Principles of Instrumental Analysis*. 6th Edition, Florence, KY: Cengage Learning, Brooks Cole.
- [4] Marzencki, M. (2005). Vibration energy scavenging. European Commission research Project VIBES (IST-1-507911) of the 6th STREP Framework Program.
- [5] Roundy, S. J. (2003). Energy Scavenging for Wireless Sensor Nodes with a Focus on Vibration to Electricity Conversion. A dissertation, The University of California, Berkeley.
- [6] Thomas, J., Clark, J. W., & Clark, W. W. (2005). *Harvesting Energy from Piezoelectric Material*. University of Pittsburgh, 1536-1268 IEEE Published by the IEEE CS.
- [7] Advanced Cerametrics Incorporated. (2007). Retrieved December 16, 2009, from <http://www.advancedcerametrics.com/>
- [8] DC-DC Converter Basics. (2008). Retrieved January 18, 2010, from http://www.powerdesigners.com/InfoWeb/design_center/articles/DC-DC/converter.shtml
- [9] Bridge Rectifier. (2008). Retrieved January 29, 2010, from <http://hyperphysics.phy-astr.gsu.edu/Hbase/electronic/rectbr.html>
- [10] Designing A SEPIC Converter Introduction. (2008). Retrieved February 11, 2010, from <http://www.national.com/an/AN/AN-1484.pdf>
- [11] Switching Regulator. (2008). Glossary of Terms. Retrieved February 16, 2010, from www.elpac.com/resources/glossary/index.html
- [12] LTspice/SwitcherCAD III. (2007). Retrieved January 14, 2010, from <http://www.linear.com/designtools/software/index.jsp#Spice>
- [13] Linear Technology. (2007). Retrieved February 1, 2010, from <http://www.linear.com>
- [14] Maxim. (2007). Operational Amplifiers, Retrieved January 2, 2010, from www.maxim-ic.com/appnotes.cfm/an_pk/1108
- [15] LT1512 SEPIC Constant-Current/Constant-Voltage Battery Charger, Linear Technology. (2007). Retrieved December 1, 2009, from <http://cds.linear.com/docs/Datasheet/1512fa.pdf>

-
- [16] Diodes. (2008). Retrieved January 20, 2010, from www.kpsec.freeuk.com/components/diode.htm

Biography

FARUK YILDIZ holds a BS in Computer Science from Taraz State University, KZ, an MS in Computer Science from City University of New York, and a Doctorate in Industrial Technology from the University of Northern Iowa. He is an Assistant Professor in Industrial Technology Program at Sam Houston State University. His research is in renewable energy harvesting, conversion, and charging system and ambient energy sources. Dr. Faruk Yildiz may be reached at fx001@shsu.edu

DESIGN AND DEVELOPMENT OF A HYPOCYCLOID ENGINE

Tom Conner, Arizona State University; Sangram Redkar, Arizona State University

Abstract

In this study, a hypocycloid engine was designed and developed. This engine is based on the Wiseman Mechanism. The Wiseman Mechanism, (patent # US 6,510,831,B2) allows the piston and connecting rod of an Internal Combustion (IC) engine to travel in a perfect linear motion while transferring the reciprocating energy from the piston to the rotational energy of the output shaft thereby reducing frictional losses at the piston pin and the piston-cylinder sidewall by reducing piston side load. This engine design offers significantly higher thermodynamic efficiency compared to the conventional slider-crank IC engine. This engine offers a high power-to-weight ratio, improved fuel consumption, reduced weight, and increased engine life. In this paper, the authors present the design, development, and simulation results of this novel engine.

Introduction

The IC engine is a dominating force in the modern industrialized world with annual production exceeding 100 million units worldwide. The IC engine is the primary driving force behind generators, automobiles, aircraft, locomotives and motorcycles, and the list goes on. In all of these applications and every other successful commercial application, the slider-crank mechanism is the method used to convert the reciprocating motion of the piston into the rotary motion of the output shaft. There has been tremendous advancement of the IC engine over the past 100 years, but this integral part has remained essentially unchanged. Additional details about IC engine technology are given by Taylor [1], [2]. There are a number of limitations and disadvantages of the slider-crank mechanism, two of which are listed below.

1. The inclination of the connecting rod produces a force on the piston perpendicular to the axis of the cylinder, causing piston side load. This side load plays a significant role in frictional losses [1], [2].
2. The reciprocating motion of the piston combined with the complex motion of the connecting rod is very difficult to completely balance and virtually impossible in single-cylinder applications [1], [3].

A proposed solution to these problems is the patented

Wiseman Mechanism [4] for IC engines. The Wiseman Mechanism, based on the hypocycloid concept (See Figure 1), replaces the conventional slider-crank or crankshaft with an equally simple mechanism that allows for perfectly linear and sinusoidal motion of both the piston and connecting rod.

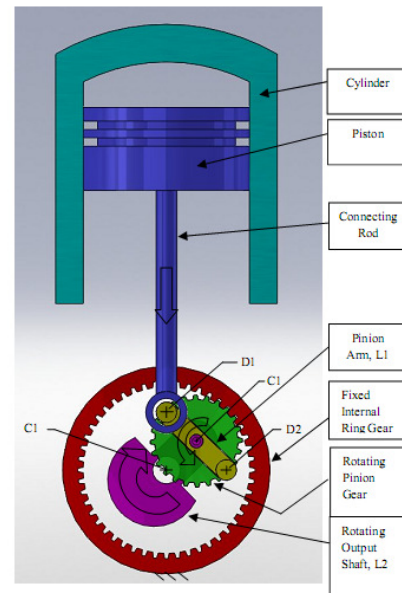


Figure 1. Single Cylinder Hypocycloid Mechanism

This simple mechanism is comprised of a rotating pinion gear that rolls around a fixed internal ring gear. When the pinion gear is half the pitch diameter of the fixed internal ring gear, the point D1 (located on the pitch diameter of the pinion gear) travels in a perfectly straight line. In addition to traveling in a straight line, the motion of D1 is also sinusoidal and a simple harmonic for any fixed engine RPM [5].

In the Wiseman Mechanism, this unique motion requires only two moving parts, which is unique and proprietary to this design and protected by a U.S. Patent [3]. The straight-line design feature eliminates piston side load and allows for perfect balance, even in single cylinder applications, without adding significant complexity. A cutaway view of the Wiseman Mechanism in a small IC engine, currently in development, is shown in Figure 2. The engine prototype is shown in Figure 3.

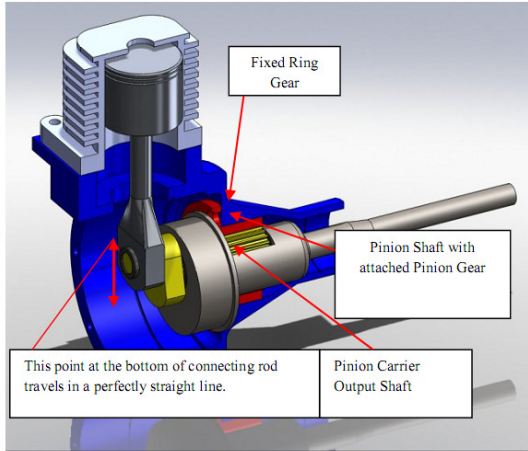


Figure 2. 30cc Wiseman Mechanism Engine



Figure 3. 30cc Wiseman Mechanism Prototype Engine

This prototype is a modified version of a two-cycle 30cc string trimmer engine. The slider-crank mechanism has been removed and replaced with the Wiseman Mechanism. Virtually all other stock engine components are unmodified including the cylinder, piston, carburetor, ignition, and exhaust. The basic engine design parameters have also been retained including bore, stroke, and compression ratio. The resulting prototype is nearly identical to the stock engine in every aspect except for the Wiseman Mechanism conversion. This prototype engine runs quite well; however, it is not perfectly balanced. Perfect balance would allow it to run smoother, quieter, and last longer than the stock conventional engine. The primary focus of this work is to perfectly balance this prototype engine using commercial motion simulation software (Solidworks Motion Analysis).

It should be noted that variations of the hypocycloid mechanism have been tested in the past [5-10]. These hypocycloid mechanisms were complex. The Wiseman mecha-

nism utilizes only 2 moving parts. In this paper, the authors present the dynamic balancing of this Wiseman mechanism using Solidworks Motion Analysis software. The most important contributions of this work are the development of a software routine that can be used to balance a single-cylinder Wiseman engine and to use this program to simulate and balance the prototype Wiseman engine and compare the engine performance. These simulation results are very important and the software program helps us to study what-if scenarios and optimize the engine hardware.

Balancing a Hypocycloid Engine

The shaking force in a single-cylinder slider-crank engine is given by [3]

$$\sum F_{sx} \cong -m_c(r\omega^2 \cos \omega t) - m_p[r\omega^2(\cos \omega t + \frac{r}{l} \cos 2\omega t)]$$

$$\sum F_{sx} \cong -m_c(r\omega^2 \cos \omega t) \quad (1)$$

where F_{sx} and F_{sy} are the shaking forces in the X and Y directions, respectively. m_c and m_p are the lumped mass of the crank and piston, respectively, r is the radius of the crank, ω is the angular velocity of the crank, and r/l is the crank-to-con-rod ratio. It can be noted that adding mass m_{BAL} with a radius r_{BAL} at 180° from m_c such that $m_{BAL}r_{BAL} = m_c r_c$ would cancel the directional shaking force completely and balance the shaking force in the direction of a reciprocating mass that oscillates out-of-phase with the piston. It is not possible to add this reciprocating mass in a single-cylinder engine and, hence, a single-cylinder slider-crank IC engine cannot be completely balanced. Sometimes overbalancing is used to minimize the shaking force due to a reciprocating mass [3], [11].

In certain applications like weed-whacker or string-trimmer engines, these undesirable shaking forces cause operator fatigue. As the engine RPM increases, the magnitude of the shaking forces increase. A detailed mathematical treatment of the single-cylinder slider-crank engine balancing is offered by Norton [3], Harkness [11] and Ishida [12]. On the other hand, the hypocycloid engine can be completely balanced reducing noise, vibration and shaking forces, significantly. The basic method used to fully balance a single-cylinder hypocycloid engine can be seen graphically in Figure 4, adapted from [6]. This method has been implemented in the Solidworks motion analysis software.

The four diagrams in Figure 4 are in 30° increments of output-shaft rotation starting in the upper left, where the piston is at top dead center (TDC). The total output rotation shown is only 90° but it is possible to extend this concept to

the full 360° of rotation. The link, L2, is analogous to the crankshaft of a conventional engine and is responsible for the output rotary motion. The link, L1, is attached to and rotates the pinion gear at twice the angular velocity and in the opposite direction of L2. The total stroke of this mechanism from TDC to bottom dead center (BDC) is four times the distance r .

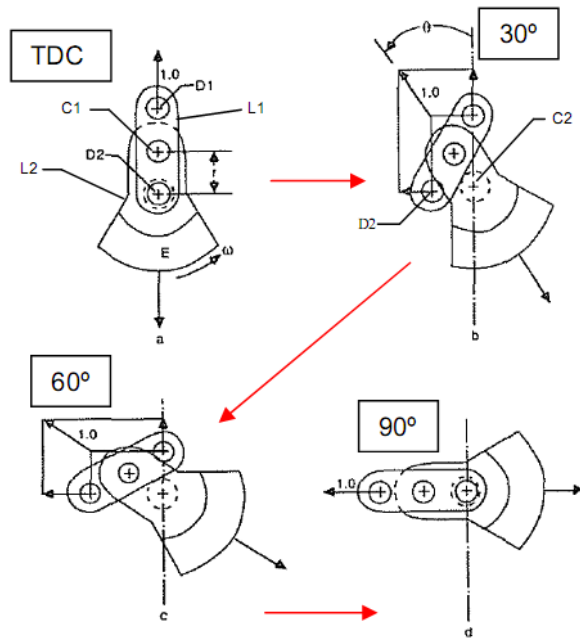


Figure 4. Hypocycloid Balance Concept Adapted From [6]

According to Beachley & Lenz [6], when attempting perfect balance in the plane shown in Figure 5, it can be assumed that the mass of the piston and connecting-rod assembly is concentrated at D1; therefore, the piston and connecting rod are not represented in this exercise. The first step in balancing this mechanism is to focus on the total mass located at point D1, which includes the piston and connecting rod mass. This mass is rotating about point C1 and, therefore, generates an inertial force which is highest at TDC. Note that even as D1 is rotating about C1, it remains on the vertical centerline at all times. In order to balance the mass at D1, a second mass at D2 is sized and located such that the center of mass (CM) of D1 and D2 is located at C1. This CM location at C1 allows the balancing method to continue by assuming the combined mass of D1 and D2 is concentrated at C1. The inertial forces generated by D1 and D2 when vector summed together act in-line with points C1 and C2 at all times. This inertial force can then be balanced by placing a counterweight, E, with its CM located 180° and equidistance (r) from C1. The inertial force vectors will then cancel and perfect balance is achieved.

Baseline Prototype Balance Evaluation

This analysis begins with modeling and simulating the existing prototype in its current state in order to establish a baseline of the vibration behavior. Once a baseline is established, the balancing method in Figure 4 will be applied to the prototype and validated in software simulations. The completed assembly, as shown in Figure 2, was used in the first baseline simulation. The engine under investigation has an exact displacement of 29.80cm³ with a stroke of 2.856cm and bore of 3.645cm. The intent of this exercise is to reduce the shaking forces generated by the rotating and reciprocating masses in the engine assembly. To reduce simulation calculation time, a few of the rotating assemblies were assumed to already be in perfect balance and, therefore, were not included in the analysis. In order for the simulation to accurately predict shaking forces, the masses of all components must be known. The density properties were assigned for each component in order to determine their total mass and CM location. The three bearings included in the simulation were the only exceptions. Because the bearings were symmetric simple shapes and already balanced, only their mass was required for the simulation.

With components and masses defined, the desired outputs of the simulation had to be specified. The internal forces that result from inertial effects in an engine design play a very important role in bearing and component loads. Another important design consideration when dealing with inertial effects was the amount of vibration that is transferred from the engine to its mounts and ultimately to the entire system surrounding the engine. In UAV's and many other applications, these forces are detrimental to Noise Vibration and Harness (NVH) performance and must be kept to a minimum. These shaking forces are the desired outputs of this analysis, particularly in the horizontal X-axis and vertical Y-axis directions as shown in Figure 5. These types of forces can be very large even for a small engine at moderate speeds in a conventional engine. The big competitive advantage of a single-cylinder hypocycloid engine is the ability to eliminate these shaking forces with proper balancing. Because the moving components are primarily in the plane shown in Figure 5, the shaking moment that occurs around the X axis will be neglected. In other words, this is a two-dimensional balancing effort. This assumption greatly simplifies this exercise; however, to fully balance the engine, the shaking moment will eventually need to be accounted for. This first simulation run is just to get a baseline of the peak shaking forces occurring in the X and Y axes as defined. The engine was simulated at a rotational speed of 3000 RPM for approximately one revolution of the

output shaft starting near TDC. The results shown assume that the engine is already running at a constant 3000 RPM and a snapshot of one revolution is taken. The shaking-force results of the baseline simulation in the X and Y axes are shown in Figure 6.

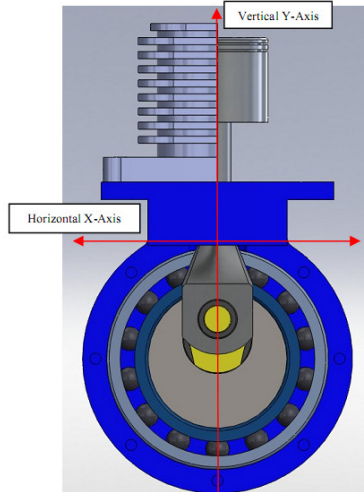


Figure 5. Axis Definitions

The results of this first simulation show a peak X-axis shaking force of 9.0 N that occurred exactly midway between TDC and BDC. In the X-axis, the inertial effect of the reciprocating piston and connecting rod is hidden, meaning that a rotational imbalance somewhere in the assembly was causing this shaking force. On the Y-axis, a much higher peak shaking force of 118 N occurred at BDC and TDC. On the Y-axis, the inertial effect of the reciprocating piston and connecting rod was dominant. The high peak force in the Y-Axis indicates that the reciprocating components were unbalanced.

Balancing Method

The balancing method for the hypocycloid engine described earlier (Figure 4) was then applied to the prototype in an attempt to reduce both the X- and Y-axis shaking forces. Material was carefully added and removed (in software) from the components involved until a perfect balance was achieved. Theoretically, it should be possible to reduce the shaking forces to zero in the simulation. However, in the real-world, limitations on manufacturing tolerances will prevent perfect balance and zero shaking forces. The simulation results are intended to be a nominal starting point for the components in the engine.

An important outcome of this exercise was the feasibility of this balance method. It may certainly be possible to perfectly balance the prototype in the simulation, but the

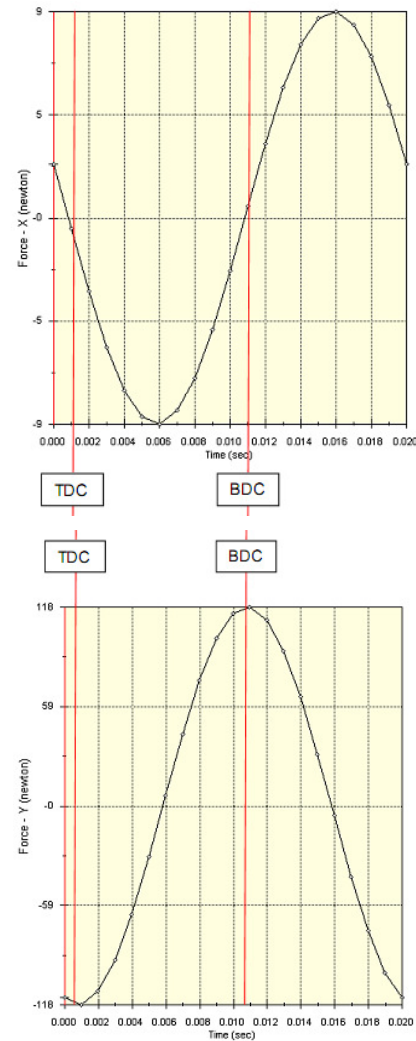


Figure 6. X and Y axis Shaking Forces

resulting design may be unacceptable due to size, strength, and weight constraints. The ability to quickly simulate different solutions offers a tremendous cost and time savings over a build, test, and modify approach using a physical prototype.

Early in the balancing process it is valuable to reduce the complexity of the system as much as possible. Simulations are repeated many times early on and unnecessary complexity slows down the process. As noted previously, the mass of the piston and connecting rod can be replaced by a concentrated point mass at D1 for the purpose of analysis. This is done by placing a solid cylinder slug that is concentric with D1 and equal in mass to the piston and connecting rod. This not only simplifies the preliminary analysis but it also verifies this mass-replacement approach. When the final simulation is run with the piston and connecting rod back in

place, balance should still be retained. The connecting rod bearing must also be included as it contributes to the mass located at D1. The modified assembly shown Figure 7 is now ready for integration and simulation of the entire engine assembly. The engine was again run at 3000 RPM in the simulation and then analyzed for shaking forces in the X - and Y-axis directions. The resulting shaking forces for the balanced design are shown in Figure 8.

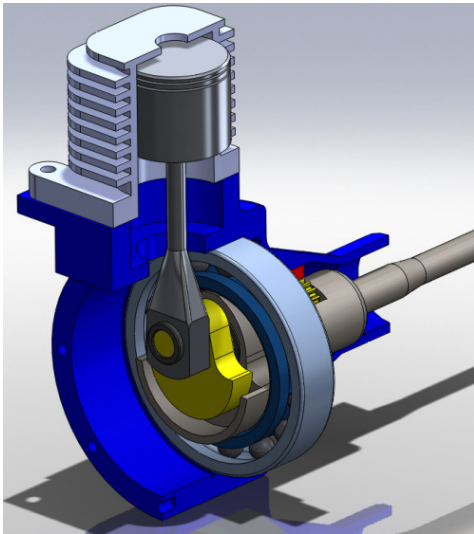


Figure 7. Balanced Assembly Model

Discussion and Results

Shown in Table 1 is a summary of the shaking forces at 3000 RPM before and after the balancing method was applied. The large percentage reduction of shaking forces in both axes proves the feasibility of the hypocycloid balancing method for use in a Wiseman engine. It also validates the technique of replacing the piston and connecting rod with a concentrated mass to simplify early analysis. The size and shape of counterweights would likely still need adjustment before manufacturing, but the design certainly appears feasible at this point. In addition, balancing the system does not require excessive material removal or excessive additional material in any specific component. The size and shape of the counterweights added are also consistent with similarly-sized conventional engines.

Currently, the existing prototype hardware is being modified and balanced. Once the balanced Wiseman engine is built, dynamometer and vibration testing can be performed. It is anticipated that the performance of this balanced engine will be better when compared to the existing unbalanced engine. These experimental results will be reported in future.

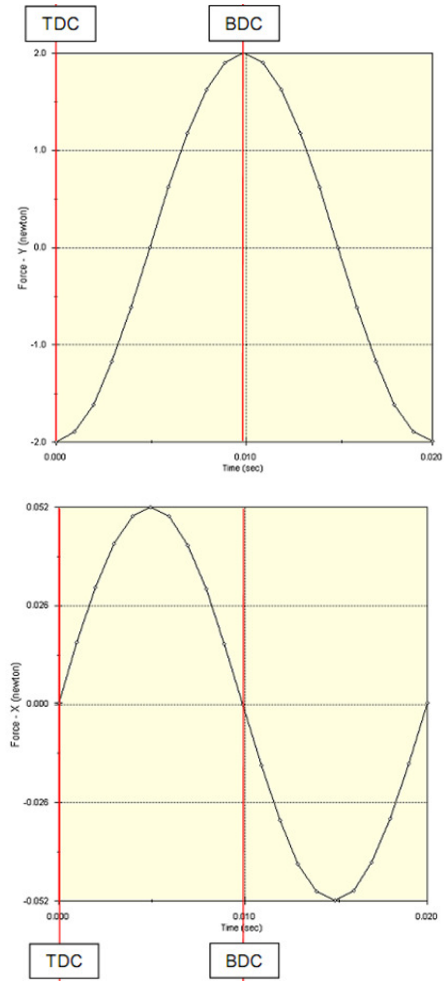


Figure 8. Balanced Engine Shaking Forces

Table 1. Shaking Force Summary Before and After Balance

	Before Balance	After Balance	Percent Reduction
X-Axis Shaking	9	.052	99.4
Y-Axis Shaking	118	2.0	98.2

Acknowledgments

The authors thank the Wiseman Group including Keith Voigts, Jerry Blankinchip, and Mark Smith for their gracious support, and extensive prototype development. This project was supported by the Governor's Office of Economic Recovery and Science Foundation Arizona.

References

- [1] Taylor, C. F., *The Internal Combustion Engine in Theory and Practice. Volume 1: Thermodynamics, Fluid Flow, Performance, Second Edition, Revised.* The M.I.T. Press, Massachusetts Institute of Technology, Cambridge, Massachusetts, 1985
- [2] Taylor, C. F., *The Internal Combustion Engine in Theory and Practice. Volume 2: Combustion, Fuels, Materials, Design, Revised Edition.* The M.I.T. Press, Massachusetts Institute of Technology, Cambridge, Massachusetts, 1985
- [3] Norton, R. L., *Design of Machinery.* New York: McGraw-Hill, 2004
- [4] Wiseman, R. Patent No. 6,510,831. US. 2003
- [5] Badami, M. & Andriano, M., "Design, Construction and Testing of Hypocycloid Machines". Advanced Powerplant Concepts 1998, SAE International Congress and Exposition, Detroit, Michigan, February 23 -26, 1998,
- [6] Beachley, N. H. & Lenz, M. A., "A Critical Evaluation of the Geared Hypocycloid Mechanism for Internal Combustion Engine Application". International Congress and Exposition, Detroit, Michigan, February 29 - March 4, 1988,
- [7] Ishida, K. & Yamada, T., "Research on a Two-Stroke Cycle Single Cylinder Vibrationless Reciprocating Engine Chain Saw Utilizing an Internal Gearing System (1st Report, Analysis of This Engine and Numerical Computation)". Bulletin of the JSME, Vol. 29, No. 257, November 1986. pp. 3846-3853
- [8] Ruch, D. M., Fronczak, F. J. & Beachley N. H., "Design of a Modified Hypocycloid Engine" International Off-Highway & Powerplant Congress and Exposition, Milwaukee, Wisconsin, September 9-12, 1991, SAE Technical Paper Series. pp. 73-90
- [9] Ruch, David M., "An Experimental And Analytical Investigation Of A Single-Cylinder Modified Hypocycloid Engine Design," PhD dissertation, University of Wisconsin at Madison, 1992
- [10] Shih, A. J., "Analysis and Comparison of Epicycloidal and Hypocycloidal Internal Combustion Engine Mechanisms" *Journal of Mechanical Design, Transactions of the ASME*, Vol. 115, 1993 pp. 960-966.
- [11] Harkness, J. R., "Methods of Balancing Single Cylinder Engines" SAE National Combined Farm Construction and Industrial Machinery, Powerplant, and Transportation Meetings, Milwaukee, Wisconsin, September 9-12, 1968, 9 p
- [12] Ishida, K., "Fundamental Researches on a Perfectly Balanced Rotation-Reciprocation Mechanism (Report 1, Basic Theories of This Mechanism and

Basic Constitutions)". *Bulletin of the JSME*, Vol. 17, No. 103, January 1974. pp. 132-140

Biographies

TOM CONNER is a graduate student in Engineering Technology Department at Arizona State University. He may be reached at tconner1@asu.edu

SANGRAM REDKAR is an assistant professor in Engineering Technology Department at Arizona State University. He may be reached at sredkar@asu.edu

THE IMPACT OF MOTORSPORTS ENGINEERING ON AUTOMOTIVE PERFORMANCE

Pete Hylton, Indiana University Purdue University Indianapolis; Andrew Borme, Indiana University Purdue University Indianapolis;
Kirk Barber, Indiana University Purdue University Indianapolis; Paul Lucas, Indiana University Purdue University Indianapolis;
Lee Beard, Don Schumacher Racing

Abstract

The application of sound engineering design principles in the development of vehicles intended for motorsports competition has come into more frequent use during the past decade. Instead of the trial-and-error mode of development, which was prevalent in motorsports in the past, engineers are now playing a major role in the design of new cars intended for competition. This has brought about a new field of study at some institutions of higher education: the field of motorsports engineering. One of these schools is Indiana University Purdue University Indianapolis (IUPUI), where students and faculty have been working with racing teams and businesses associated with motorsports to produce designs capable of improving vehicle performance in competition. On June, 11, 2010, Cory McClenathan set a new world record for the quickest that a vehicle has ever traveled 1,000 feet from a standing start. The record was the result of a unique collaboration between Don Schumacher Racing (DSR) and IUPUI and was a demonstration of how the engineering aspects of motorsports are making an impact in engineering education, as well as how motorsports engineering graduates will impact the future of the sport and automotive design.

Introduction

In a world where engines produce over 8,000 horsepower and vehicles achieve over 300 miles per hour in a mere 1,000 feet of distance in just over three seconds of time, engineering analysis can be a very useful tool to achieve performance optimization. In an effort to examine vehicle behaviors in this incredible environment, Don Schumacher Racing (DSR) and Indiana University Purdue University Indianapolis (IUPUI) partnered on an educational research program [1]. DSR is one of the most successful teams in the Top Fuel category of the National Hot Rod Association's (NHRA) premier drag racing series. IUPUI is the first university in the United States to offer a bachelor's degree in motorsports engineering [2], with a curriculum specifically aimed at training the next generation of engineers for the motorsports industry [3]. The innovative motorsports engineering courses at IUPUI, with a distinct applied-engineering slant, have drawn attention for their innovation

[4]. Plans of study that involve experiential learning and research activities, which focus on undergraduate student involvement, have been indicated in studies by the National Academy of Engineering [5] and numerous leaders of engineering academia [6] as the direction of the future for engineering education. IUPUI has been one of the leaders in attempting to develop innovative curricula for undergraduates and pre-engineering STEM students [7], with motorsports-themed activities leading the way [8].

The relationship between DSR and IUPUI arose from the inspiration of Lee Beard, the DSR Team Manager. Race teams are always looking for a competitive advantage, and Beard believed that the coupling of bright young minds from the university with experienced members of DSR's team could yield new ideas. The first project of the partnership was aimed at determining the characteristics of the chassis of a Top Fuel class car, which might have a beneficial effect on performance. Cory McClenathan was the driver of one of the DSR Top Fuel cars, shown in Figure 1.

Methodology

With the tremendous levels of power being transmitted to the ground by these cars, traction is paramount. The critical focus of the study became whether the chassis could be optimized in a way that positively enhanced the car's ability to maximize traction. The first step was to construct a Finite Element Model (FEM) of the existing chassis. IUPUI students worked side-by-side with DSR fabricators to understand the design of the frame and develop their model, as shown in Figure 2. The students had completed courses in structural modeling, statics, dynamics, and vehicle dynamics, all under the guidance of IUPUI's engineering technology and motorsports engineering faculty. The model was constructed as a tube frame using a FEM routine. Particular attention had to be paid to tube dimensions, material properties, and configuration of the tube junctions.

The second step was to correlate the model. DSR conducted a static load test, fixing the frame at the front suspension attachment points and at the rear axle housing. A static load was applied in the center of the frame and deflections were measured along its length. The model was then con-

strained at the same locations and the same load was applied. Predicted and measured deflections were then compared. This step required refinement of the model, particularly in the vicinity of the rear constraint, to accurately represent the frame in its test configuration. The emphasis had originally been on the frame members and not on the axle housing. This had to be adjusted in order to match the test results.



Figure 1. Cory McClenathan’s Don Schumacher Racing Top Fuel dragster was the object of a redesigned chassis based on analysis by motorsports engineering students (Photo used with permission of DSR)

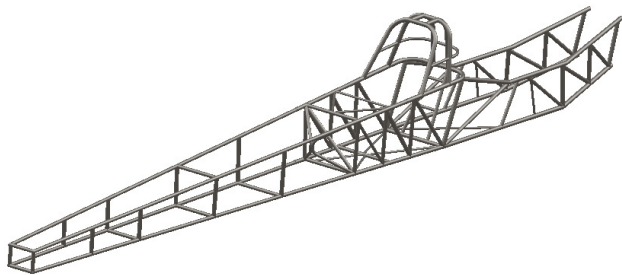


Figure 2. Finite element model of a Top Fuel dragster chassis

Ultimately, a good correlation was achieved, as shown in Figure 3, allowing the analysis to continue. The chassis has a different stiffness in twist, vertical bending, and horizontal bending. The next step in the process was for the experienced members of the DSR team to sit down with the IUPUI students and faculty to discuss what flexibility characteristics of the chassis they collectively believed had the greatest impact on the vehicle’s ability to maximize traction and, thus, its ability to put the power to the ground. The IUPUI team then began parametric studies utilizing the correlated model. Over a hundred different configurations were examined in a process that indicated several trends pointing toward the selected goals. To examine the various

configurations, three load cases were repeatedly applied to the model. One case examined vertical bending of the chassis, one examined lateral bending of the chassis, and the third examined torsional twist of the chassis. Deflection results of the model, as shown in Figures 4 and 5, were summarized for each configuration and were compared back against the baseline to see which configuration best achieved the goals. In addition to the performance parameters, maximum stresses under various load conditions were tracked to make sure that frame life would not be significantly impacted; weight was also tracked since a gain in weight of the race car would offset any advantage gained from the increase in traction.

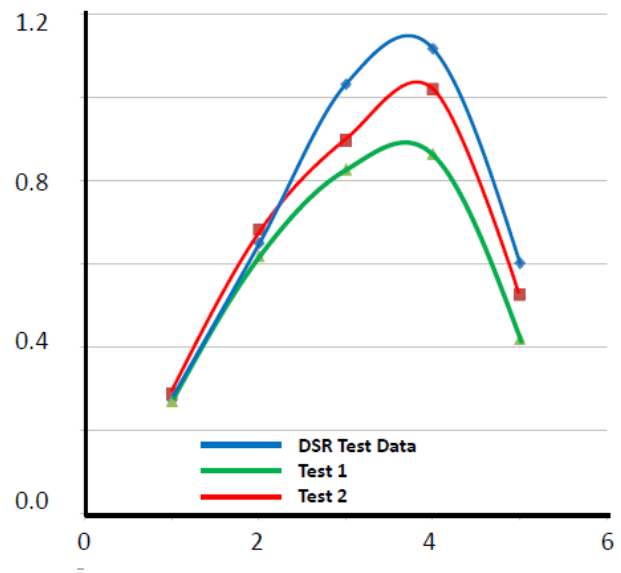


Figure 3. Correlation of chassis deflection test and analysis data

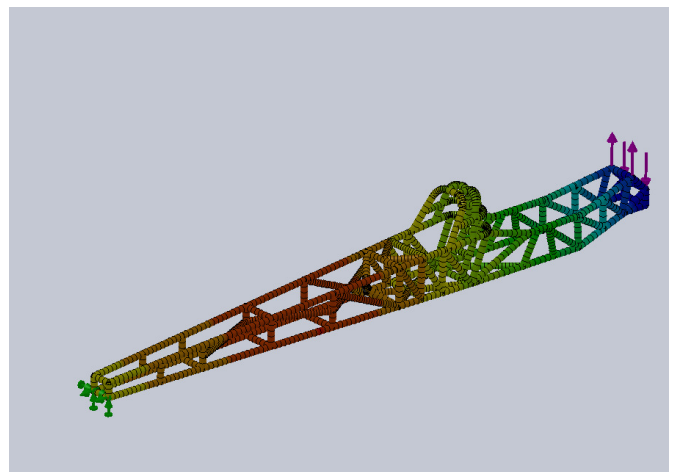


Figure 4. Predicted bending deflections shown for a load case on the Top Fuel chassis

Another aspect of vehicle design that was examined was driver safety. Fire is always a safety concern in motorsports, especially in the Top Fuel classes where nitro methane is used as fuel. Figure 6 shows the magnitude of the fireball that can occur in a worst-case scenario. Given the proximity of the driver to the engine, as shown in Figure 7, there is a possibility of flame or engine parts making their way into the driver's cockpit in such an explosion. For that reason, the DSR staff was interested in extending the protective cowling from behind the driver's head, over the top of the cockpit, to create a barrier against fire and, thus, further protect the driver. However, even to the casual observer, such additional bodywork would appear likely to increase the aerodynamic drag around the cockpit. In a car running over 300 miles per hour, such drag could become a real competitive disadvantage.

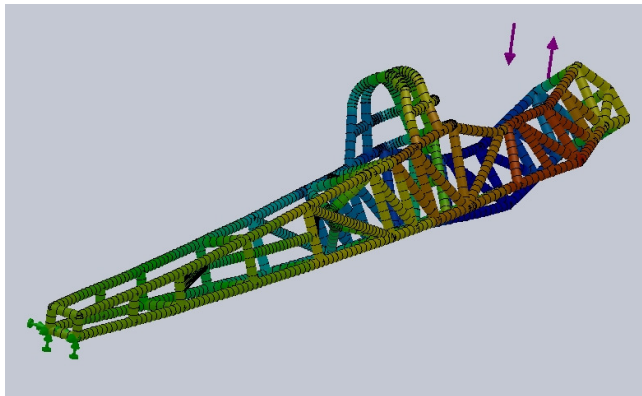


Figure 5. Predicted torsional deflections shown for a load case on the Top Fuel chassis



Figure 6. Fire is always a safety concern in nitro methane-fueled dragsters (Photo used by permission of Jeff Burk/ DragRacingOnline.com)

Therefore, another study was initiated by IUPUI and DSR, relative to the aerodynamics of the car. Using the

Computational Fluid Dynamics (CFD) options of the FEM routine, the streamlines and turbulent-energy distribution around the cockpit were examined, as shown in Figure 8. This was done in order to ascertain whether the additional protective cowling would, as expected, create unwanted drag. When it was determined that the effect would be a performance disadvantage, further analysis was performed to determine if there existed a means to counteract this negative effect. A proposed modification to the windscreen was determined, which would subtly deflect air around the cockpit in a manner that prevented the new protective cowling from being an aerodynamic disadvantage. However, to further ensure that no detrimental effects occurred due to the changes, the flow of air around the cockpit was examined to determine if it would hinder the air flow into the engine's inlet or if it would alter the airflow over the downforce-producing rear wing. Figure 9 shows results of this portion of the analysis.



Figure 7. The air flow around the cockpit and engine of the Top Fuel car was an area of interest (Andrew Borme photo)

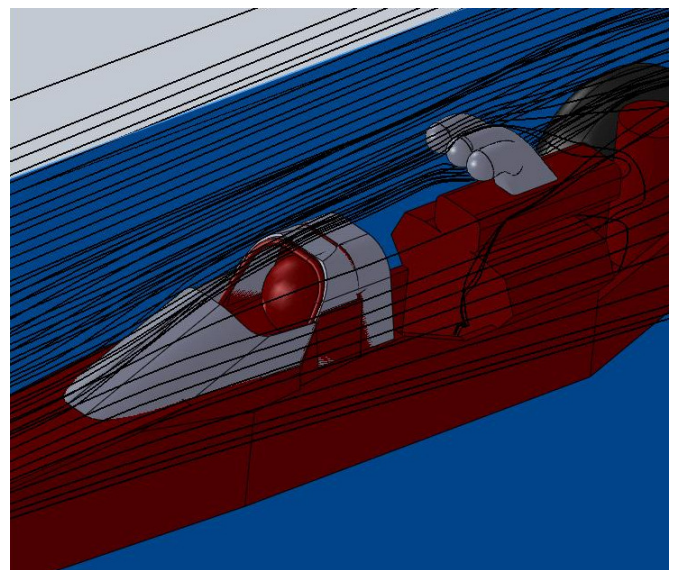


Figure 8. CFD analysis model showing airflow streamlines over and around the cockpit and engine

CFD analysis is akin to conducting a wind-tunnel test on a computer; it provides both a visualization tool and a calculation tool, and will allow the engineer to calculate both lift (or in the case of a racecar, downforce) and drag as a function of the shape of the car. Flow energy, as well as turbulence, was studied. In the end, an appropriate combination of cockpit cowl and windscreen angle was determined, which provided the desired protection without hurting the drag, the engine inlet flow, or the downforce provided by the rear wing.

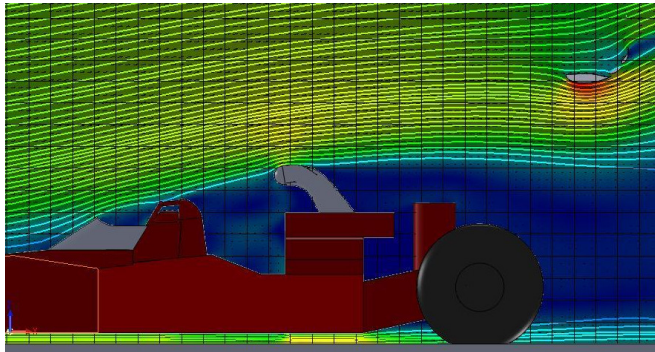


Figure 9. CFD analysis model showing airflow energy over and around the cockpit, engine, and rear wing

Results

Motorsports of any form is, by definition, a very competitive business. For this reason, those working on the DSR/IUPUI project are not at liberty to discuss either the precise goals that were set or the exact chassis modifications that were used to achieve them. However, the results have been stunning. An initial configuration change was implemented in Cory McClenathan's frame in June, 2010. The second event after the change was held at Old Bridge Township Raceway Park in Englishtown, New Jersey. The team set the fastest thousand-foot time in NHRA history at 3.752 seconds and a top speed of 324.75 miles per hour. In the post-qualifying interview, McClenathan acknowledged the work of the university, saying, "We have been working with IUPUI, and those kids are just unbelievable when it comes to aerodynamics and how the chassis should work. We have been working close with them and they were a big part of some configurations we have used. This car is basically set up the way they would like to see it go in the future." [9]

The configuration of the cowl around the cockpit was tested on two of the DSR cars during practice days for the annual U.S. Nationals race at O'Reilly Raceway Park in Indianapolis, held on Labor Day weekend, 2010. Both cars ran equivalent elapsed times and top speeds to their old configuration, while utilizing the new cowl and windscreen.

Pressure data was also taken around the engine inlet, and no loss of air flow was detected. These results would indicate that the use of engineering tools and analytical skills allowed a configuration to be designed that had the desired safety provision with no detrimental performance impact. But more importantly, from a safety standpoint, when Tony Schumacher's engine exploded after the end of one of the test runs, no fire entered the cockpit and, in fact, the driver was initially unaware of the explosion. Subsequently, Schumacher, on March 27, 2011, in a race in Pomona, California, set the fastest-ever top speed for a thousand-foot run, at just over 327 miles per hour, using the new cockpit cowl. Clearly, this new design offers protection without harming vehicle performance.

Conclusions

1. Proper selection of racing-chassis stiffness parameters has been shown to affect the ability to maximize vehicle traction.
2. Small changes in body shape can create noticeable improvements in air-flow around the race car, affecting drag, downforce, and inlet flow.
3. The use of engineering-design skills to achieve improved vehicle designs in motorsports can determine subtle changes capable of producing significant results.
4. Engineering programs focused on motorsports can develop curricula and research projects with the ability to develop unique skill specialties applicable to motorsports, and produce students capable of making a significant impact within the industry.
5. Since developments in motorsports can lead to improvements in street cars, a program such as the one discussed here may one day influence the design of everyday vehicles.
6. Industry/academia partnerships can yield both innovative improvements and excellent learning opportunities.

References

- [1] "DSR and IUPUI Share Latest Technology to Improve On-Track Performance," *Motorsports Journal*, January 16, 2010. Retrieved from http://www.motorsportsjournal.com/archives/2010/01/dsr_and_iupui_s.php.
- [2] Tussing, M. "Motorsports Degree Program at IUPUI Is Off to Fast Start," *Indianapolis Star*, May 15, 2009, A23.
- [3] Hylton, P. "Let's Go Racing – Constructing a Collegiate Motorsports Program," *Proceedings of the*

-
- ASEE Section Conference*, Indianapolis, Indiana, March 2007.
- [4] Hylton, P. "Guest Editorial: Students and Careers in Motorsports," *Manufacturing Engineering*, 141(3).
- [5] National Academy of Engineering, *Educating the Engineer of 2020*. Washington, D.C.: The National Academies Press, 2005.
- [6] Vest, C. (2008). "Context and Challenge for Twenty-First Century Engineering Education," *Journal of Engineering Education*, 97(3), 235-236. Retrieved from Education Research Complete database (34435790).
- [7] Hylton, P. and Otoupal, W. "Engaging Secondary-School Students in Pre-Engineering Studies to Improve Skills and Develop Interest in Engineering Careers." *The International Journal of Engineering Education*, 25(3), 119-125.
- [8] Hylton, P. "Using Motorsports Design Concepts to Further STEM Education," *Journal of Technology Studies*, 36(1), 12-15.
- [9] Burgess, P. "Cory Mac Makes Quickest-ever Pass to Lead Super Nationals Qualifying," *National Dragster On-line*, July 11, 2010. Retrieved from <http://www.nhra.com/story/2010/6/11/2010-englishtown-friday/>.

Biographies

PETE HYLTON is currently an associate professor and director of motorsports engineering at Indiana University Purdue University Indianapolis. He has industry experience in both aerospace and motorsports and is responsible for the creation of the first motorsports engineering BS degree program in the United States. He is author of several books on motorsports history and is a recipient of the Sports Car Club of America's highest honor, the Woolf Barnato Award for contribution to motorsports. Professor Hylton may be reached at phylton@iupui.edu

ANDREW BORME is currently a lecturer in the Indiana University Purdue University Indianapolis motorsports program. He has extensive industry experience in motorsports with two Indianapolis 500 Mile Race wins as an engineer for driver Helio Castroneves and three years as the chief-aerodynamics engineer for the Toyota Formula One team. Professor Borme may be reached at aborme@iupui.edu

KIRK BARBER is a motorsports engineering student at Indiana University Purdue University Indianapolis and was an integral part of the project that led to redesigning the Top

Fuel dragster that was used by Don Schumacher Racing and Cory McClenathan. He is expecting to graduate with a dual BS degree in motorsports engineering and mechanical engineering in May 2013. After graduation, Kirk plans to use his education and experience to build high performance, environmentally friendly automobiles. He has experience in several different forms of motorsports and is currently the youngest championship-winning crew chief in United States Auto Club (USAC) history. Mr. Barber may be reached at kirbarb@iupui.edu

PAUL LUCAS is currently working toward a bachelor of science in motorsports engineering at Indiana University Purdue University Indianapolis. He is a member of IUPUI's Formula SAE team as a chassis team member and was an integral part of the project that led to redesigning the Top Fuel dragster that was used by Don Schumacher Racing and Cory McClenathan. Mr. Lucas may be reached at pwlucas@iupui.edu

LEE BEARD has spent more than 30 years in drag racing. He has earned more than 50 wins as a crew chief in the Top Fuel and Funny Car ranks. He began his career as an owner/driver in the Top Fuel class in the early 1970s and has tuned for some highly successful drivers, including Jerry Ruth, Gary Ormsby, Pat Austin, Ed McCulloch, Cory McClenathan, Cruz Pedregon, Kenny Bernstein, Whit Bazemore, Rod Fuller, and Antron Brown. He led Ormsby to the 1989 NHRA Top Fuel championship and has won the prestigious U.S. Nationals event four times.

TOOL-CONDITION MONITORING IN CNC TURNING OPERATIONS: A STATISTICAL APPROACH FOR QUICK IMPLEMENTATION

Samson S. Lee, Central Michigan University

Abstract

This study presents the development of a tool-condition monitoring (TCM) system that utilizes signal decomposition techniques and multi-sensor methods. The raw signals obtained from multiple sensors under a series of combination of different machining parameters and tool conditions were examined. The most significant components of each signal were employed to develop a tool-condition monitoring system. Fairly simple and quick statistical model implementation methods are proposed to eliminate the effects of machining parameters from the signal sensor to avoid multicollinearity among independent variables. The statistical TCM system developed in this study showed 90% accuracy from 151 test samples with a reject flank wear size of 0.2mm or larger. The test results demonstrated the practical applicability of the TCM system developed to reduce machine downtime associated with tool changes and to minimize the number of scraps in existing machine shops.

Introduction

Metal-cutting processes, such as milling, drilling, and turning operations, are primary manufacturing processes and finishing operations used to achieve very high dimensional accuracy close to the desired surface finish [1]. Even though automated metal-cutting processes, such as computer numerical control (CNC) machining, has provided cost-effective solutions by replacing highly skilled but costly laborers, manufacturers have faced increasing mass-customized product demands in the past couple of decades [2-4]. The products have become more individualistic, varied, and complex to manufacture. Manufacturers require new technologies and methods that allow small-batch production to gain the economic advantages of mass production [1], [5], [6]. Computer Integrated Manufacturing (CIM) and Flexible Manufacturing Systems (FMS) provided ideal solutions by increasing machining flexibility (the capability to perform a variety of operations on a variety of part types) in addition to flexibility in routing, process, product, production, and expansion [1].

Although the combination of CIM and FMS technologies showed a great promise as cost-effective solutions for current industry demands, CIM-FMS systems require a number of prerequisites, such as uninterrupted machining to achieve maximum efficiency [7]. However, deteriorating process conditions often force manufacturers to interrupt machining processes to respond to deteriorating production conditions such as machine conditions. Thus, developing an effective means of monitoring machine conditions has become one of the most important issues in the automation of the metal-cutting process [8].

Among the many possible machine conditions to be monitored, tool-condition is the most critical for ensuring uninterrupted machining as poor tool conditions can cause degraded surface quality, dimensional work piece defects, and even machine failures [8]. Any effective monitoring system must sense tool conditions and allow for effective tool-change strategies when tools deteriorate and maintain proper cutting conditions throughout the process by reducing machine downtime caused by changing the tool, thus leading to fewer process interruptions and higher efficiency [9]. The information obtained from the tool-wear sensors can be used for several purposes including the establishment of a tool-change policy, economical optimization of the machining operations, on-line process manipulation to compensate for tool wear, and, to some extent, the avoidance of catastrophic machine failure.

Since advanced machining was introduced in the mid-1900s, various methods to monitor tool wear have been proposed, thereby expanding the scope and complexity of traditional methods. However, none of these efforts has been applied universally due to the complex nature of the machining process [10]. More automated approaches were attempted using computer-numerical control (CNC) technology. However, several obstacles, such as 1) the narrow learning capability of CNC machines, 2) the limited flexibility of the CNC controller, 3) the relatively large dynamic errors encountered in CNC operations, 4) sensor noises, and 5) the inconsistency between machines, halted widespread implementation [11]. Many studies attempted to overcome these limitations by finding and utilizing various sensor technologies and signal-processing techniques.

Tool-condition Monitoring Studies

Tool-condition monitoring methods can be classified into direct and indirect methods, depending on the source of signals collected by sensors. Direct methods sense tool conditions by direct measurement of the tool. Direct methods include optical, radioactive, and electrical resistance. Alternatively, indirect methods sense the tool conditions by measuring secondary effects of the cutting process, such as acoustic emission (AE), sound vibrations, spindle- and feed-motor current, cutting force, and machining vibrations. Direct methods are beneficial because they take close readings directly from the tool itself. In contrast, indirect methods must rely on conditions other than the tool itself to judge tool conditions. However, direct methods are limiting because the machining process must be interrupted to make the direct measurements [12-14]. As a result, machine downtime increases, as do costs for tool-condition monitoring, which is contrary to the purpose of the TCM system. Researchers, therefore, have preferred indirect methods to study in-process tool-condition monitoring systems.

Because indirect methods do not require access to the tool itself to measure the tool conditions, signals that indicate the tool condition can be gathered in real-time, while the machine is running. However, despite the benefits of in-process measurement, indirect methods also have some disadvantages. Because the information (or signal) is collected by sensors which do not measure the tool conditions directly, additional components are required to correlate the indirect measurements with tool conditions. Additionally, indirect measurements are weakened by noise factors associated with the machining process and environments. Noise factors tend to weaken or totally eliminate relationships between the indirect information and actual tool conditions. For indirect, in-process measurements to be effective, methods that can identify significant signal components and eliminate the interfering noise are required.

In the many studies attempting to correlate indirect sensor signals with actual tool conditions, the following methods have been actively employed: 1) statistical regression techniques [9], [15-18], 2) fuzzy logic [10], [19], 3) artificial neural networks [20-25], and 4) fuzzy-neural networks [11], [26-28]. In many of the aforementioned studies, the relationships between indirect signals and tool condition were weak because unknown factors and noise factors diluted the signals collected by the sensors during machining. Some studies attempted to eliminate or minimize noise factors from the information collected by indirect sensors. Wavelet transform methods were used to remove noise factors from the information collected by the sensors [10], [29-31]. These studies showed that a wavelet transform process

can increase the correlation between the de-noised signals and tool conditions. However, these studies still could not separate the significant component of the indirect signals to provide a strong relationship with tool conditions.

A limited number of sensors have been adopted in most studies involving indirect sensing systems. The most widely adopted sensors are 1) dynamometers [9], [11], [32], [33], 2) acoustic emission (AE) sensors [3], [34], [35], 3) microphones [4], [36], and 4) accelerometers [2], [8], [18]. However, the limitations of the sensors must be considered in TCM studies, such as high cost, lack of overload protection, and noise integrity [37], [38]. Some studies showed improvements in tool-condition recognition by combining multiple sensing technologies [2], [28], [39-41].

From a review of previous studies, this study employed the following technologies to develop a TCM system: 1) a tri-axial accelerometer and condenser microphone for indirect sensors, 2) wavelet decomposition for signal processing, and 3) statistical analysis for signal components analysis and tool-condition prediction. The sensors employed provided relatively easy mounting methods with fairly low costs. The wavelet decomposition technique was employed not only to filter noise factors but also identify significant signal components for tool conditions. The statistical approach was employed for a relatively short model-development time and quick implementation into the machine. Figure 1 illustrates the overall process of this study.

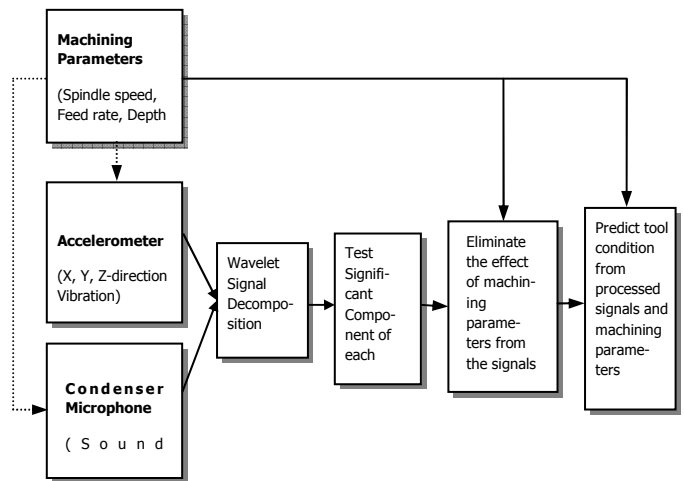


Figure 1. Illustration of Overall Process

Experimental Setup

For this study, a Hass SL-10 CNC Turning Center was employed. For simultaneous multi-directional vibration signal collection, an ICP tri-axial accelerometer, model

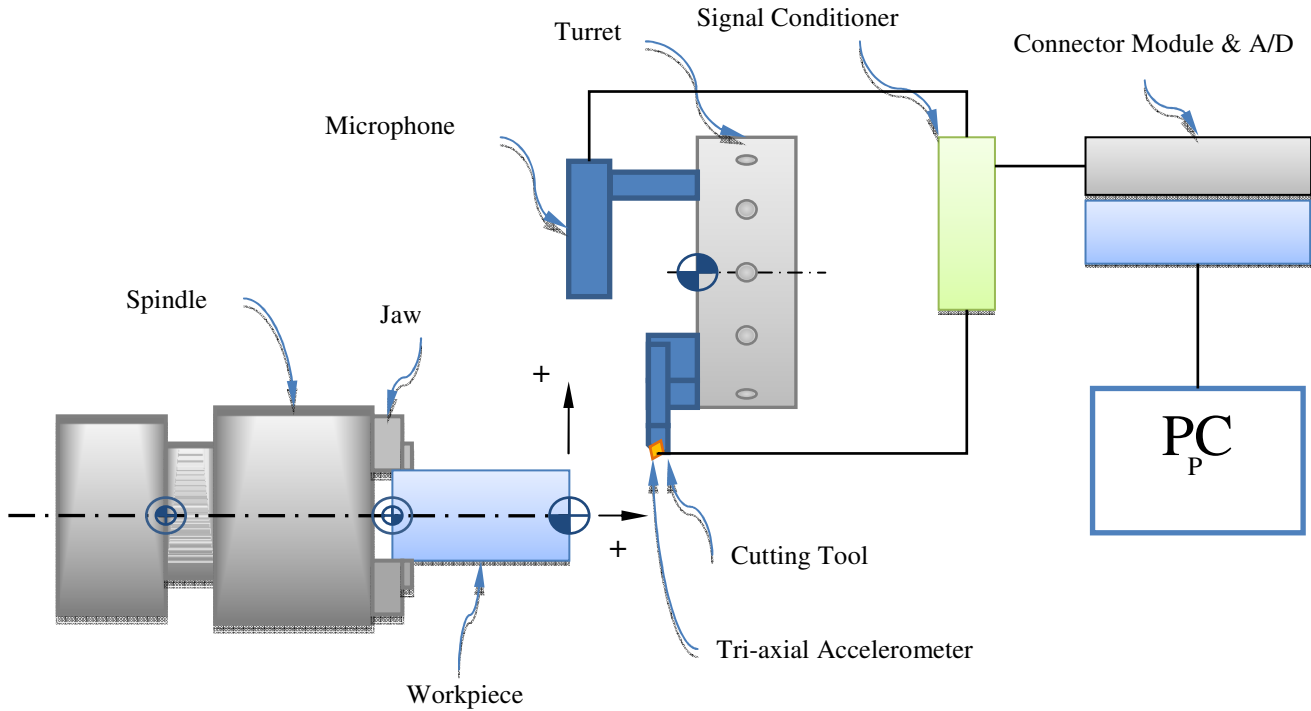


Figure 2. Illustration of Experimental Setup

356B21 from PCB Piezotronics, was employed. Its response frequency range (2 to 2000Hz) and high sensitivity (10mV) allowed for the exploration of various signal components. For sound signal collection, a PCB condenser microphone, model 377B02 from PCB Piezotronics, and a preamplifier, model 426E01 from PCB Piezotronics, were employed. The condenser microphone provided a wide range of frequencies (3.15 ~ 20,000Hz), which was crucial for this study as it allowed for the exploration of various frequency-screening windows. For signal conditioning, an ICP Sensor Signal Conditioner, model 482A22 from PCB Piezotronics, was adopted. It provided four input and output channels simultaneously with significantly lower noise. The signals passed through the signal conditioner were sent to a data-acquisition system. For the data-acquisition system, a DaqBook 2005 A/D converter and DBK85 input module from IOtech were employed. DaqView data-acquisition software was also employed in this study to record data on a PC. A series of post processes, including signal processing and data analysis, were performed on a PC. Figure 2 shows the illustration of the experimental setup.

There were three directions of vibrations measured in this experiment: the positive x (+X) direction, defined as the radial direction from the center of the work piece to the tool tip; the positive z (+Z) direction, defined as the longitudinal

direction from the work piece holder to the tool holder; and, the positive y (+Y) direction, the tangential direction, which was assigned using the right-hand rule. This study employed the straight cut (a major cutting type in turning operations), with hardware setup that included a general-purpose indexable insert tool, a befitted shank, and a tool holder for the indexable insert tool. To ensure a stable cutting operation, the cutting tool was aligned with a radial line of the work piece.

In this study, the tri-axial accelerometer was mounted under the shank, which was determined to be an efficient position for detecting the vibration from the cutting tool during machining. The condenser microphone was mounted in the machine, aiming the contact point between the cutting tool and specimen. To avoid direct contact with chips, a customized fixture was designed and inserted in the turret of the machine. Figure 3 shows the schematic illustration of the microphone and the fixture in the turret.

The goal of this study was to develop a tool condition monitoring system using the signals detected by the two sensors with three machining parameters (spindle speed, feed rate, and depth of cut). To conduct the experiment, an experimental design was established. Two sets of data were designed for the development of a TCM system in this

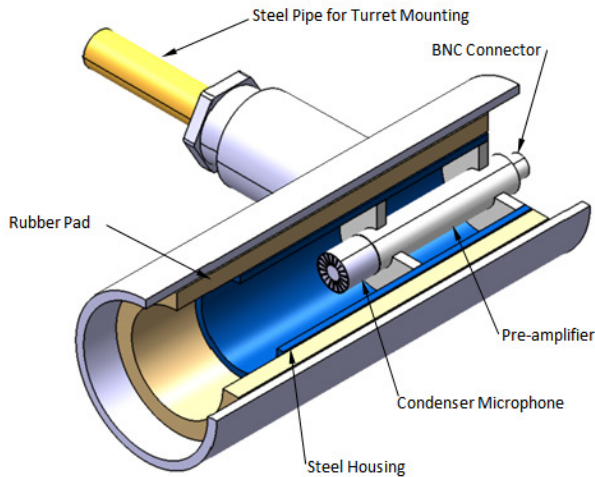


Figure 3. Microphone Fixture Design

study. The first set was designed to develop a TCM prediction model. Three different spindle speeds, feed rates, and depths of cut were determined. These machining parameters were determined based on the combination of the work piece material and cutting tool. Appropriate parameters are recommended by the machine-tool manufacturer to ensure the quality of the product and the life of the machine. In this study, general ranges of spindle speeds, feed rates, and depths of cut were chosen with combinations of the tools that have different amounts of wear. Machining behavior was determined by signals captured by the two sensors (tri-axial accelerometer and condenser microphone) under different combinations of tool and machining conditions. A second set was designed to test the TCM model, which shows its prediction capability of under the identical machining conditions of the first data set. The second data set also included two different spindle speeds, feed rates, and depths of cut, with machining conditions not included in the first data set. These data were included to test the flexibility of the TCM system. From the experiment, a total of 270 signal data were collected for model build and 151 signal data for system test.

Signal Processing and Post Process

Among the many statistical properties of the raw signals (such as mean value, maximum value, minimum value, standard deviation, etc.), several studies have suggested that the adjusted mean value or root mean square (RMS) of the signal data can be used to represent the characteristics of the raw signal [15], [42-44]. Based on these findings, this study utilized the adjusted mean values of each member in the data set to define the overall characteristics of the data from the experiment.

The raw signal obtained from the sensors contains not only the signal caused by the interactions of the tool and work piece, but also background “noise” signals from other sources, such as the hydraulic pump motor, feed motors, and environmental vibrations. Therefore, it is extremely difficult to detect or obtain any desired characteristic free of all the others. There is also no guarantee that detecting only the desired signals is an effective means of monitoring the tool condition.

Several studies employed a signal decomposition technique for TCM systems [10], [30], [31], [45], [46]. However, these studies utilized only the noise-cancellation aspect of the wavelet transform. Using this method, there is also no guarantee that the filtered signals, obtained after canceling the signals categorized as noise, are sufficient for monitoring the tool condition. Therefore, it is necessary to analyze each signal component obtained by the signal-decomposition process to find those most suitable to the task of detecting the tool condition.

Data from each raw signal were transferred to Matlab and decomposed into six components. For the decomposition process, the 4-level Daubechies decomposition scheme was employed [47]. After the decomposition, the adjusted mean value of each component was stored for further data analysis. This study employed Matlab and its add-on wavelet toolbox to decompose the signal.

The outcome of the decomposition process of the raw data was six component signals from each of the raw signal data. The adjusted mean value of each signal component was calculated and utilized as the statistical property of each component. To find the most significant component related to tool conditions, a simple statistical analysis was performed using a multivariate test using JMP from SAS. Correlation factors of each signal component to tool wear amounts were determined. The test results are shown in Table 1.

Table 1. Correlation factors of tool wear and signal components

Signal	Org	Cmp1	Cmp2	Cmp3	Cmp4	Cmp5	Cmp6
X	.0523	.0008	.0246	.0793	.3043	.2414	.4944
Y	.1035	.0167	.0233	.0314	.0753	.0831	.3808
Z	.0090	.0240	.0436	.0503	.1929	.2013	.4716
S	.0186	.0973	.0895	.0604	.0800	.0293	.0506

The test revealed that the 6th component of the three direction vibration signals had the most significant relationship to tool wear. Compared with the original signals, dra-

matic increases of correlations with tool wear were found. Results from microphone signal analysis showed that the 1st component had a more significant relationship with the tool wear than the other components. From the test results, the 6th component of each vibration signal and the 1st component of the sound signals were employed to represent each of the signals for further analysis.

To develop a tool-condition prediction model, this study employed a statistical multiple regression analysis. The independent variables in this analysis were: different machining conditions; the combinations of spindle speed, feed rate, and depth of cut; and, the signals obtained from the two sensors. The dependent variable was the amount of tool wear under each cutting condition. However, strong interactions were expected between the machining parameters and signals employed as independent variables. This crossed relationship among independent variables is referred to as multicollinearity. The existence of multicollinearity can be interpreted as the duplicated effects of some independent variables on the other independent variables. All of the independent variables were used to predict the dependent variables.

The following sections introduce the method used to test multicollinearity among the independent variables, which are machining parameters and signals. Additionally, these sections describe the method used to eliminate the effect of the variables of machining parameters from the variables of signals. To find the existence of the duplicated effects of independent variables on dependent variables, a multivariate test was performed. The Pearson correlation factors of each of the variables were calculated based on the following equation.

$$r = \frac{\sum (x - \bar{x})(y - \bar{y})}{\sqrt{\sum (x - \bar{x})^2} \sqrt{\sum (y - \bar{y})^2}} \quad (1)$$

where r = Pearson correlation factor of variables x and y
 \bar{x}, \bar{y} = mean of variables x and y

Table 2 summarizes the test results showing the significant relationships among the machining parameters (S: spindle speed, F: feed rate, D: depth of cut), three vibration signals (V_x, V_y, V_z), and the sound signals (S_m). The existence of a relationship between the machining parameters and two sensor signals was observed. In other words, the existence of multicollinearity among independent variables was found.

To eliminate the effects of machining parameters from the vibration signals of the three directions and sound signals, the following assumption was applied:

$$S_i = f_i(SP_i, FR_i, DC_i) + E_i + e_i \quad (2)$$

where S_i = measured signals from a sensor
 SP_i = spindle speed
 FR_i = feed rate
 DC_i = depth of cut
 E_i = effect of other factors during machining
 e_i = error

Table 2. Pearson correlation factors between machining parameters and sensor signals

	V_x	V_y	V_z	S_m
S	-0.1290	-0.4066	-0.2663	-0.2847
F	-0.0179	-0.0974	-0.0776	-0.4340
D	.0144	.0358	.0167	-0.0725
S × F	-0.0648	-0.3102	-0.1932	-0.4570
S × D	-0.0938	-0.3074	-0.2016	-0.3515
F × D	-0.0387	-0.0540	-0.0636	-0.2994
S × F × D	-0.0803	-0.2729	-0.1811	-0.4279

This assumption allowed a multiple regression analysis with interaction terms to be used to eliminate the effects of the spindle speed, feed rate, and depth of cut from the raw signals. In the analysis, each signal was tested as an independent variable, and the machining parameters were employed as the dependent variables. By subtracting the predicted values of each signal from the observed values and the machining parameters, a new signal value was obtained. Finally, the new signal values can be assumed not to have the effects of machining conditions, spindle speed, feed rate, and depth of cut.

Based on the ANOVA test results of each signal, four prediction models of each signal could be determined. Each signal model employed the spindle speed (S), feed rate (F), and depth of cut (D) as independent variables. Hence, the vibration signals (V_x, V_y, V_z) and the sound signal (V_s) could be transformed by the following equations based on each predicted signal (\hat{V}_x : predicted x-direction vibrations; \hat{V}_y : predicted y-direction vibrations; \hat{V}_z : predicted z-direction vibrations; \hat{V}_s : predicted sound signals):

$$\begin{aligned} V'_x &= V_x - \hat{V}_x = V_x - .012547 + .000001 S_i - .332111 F_i \\ &- .9671704 D_i - .0000667 S_i F_i + .000526 S_i D_i + 38.12174 F_i D_i \\ &- .0170011 S_i F_i D_i \end{aligned} \quad (3)$$

$$V'_{zi} = V_{zi} - \hat{V}_{zi} = V_{zi} - .020332 + .000002S_i - .0471871F_i - 1.0568589D_i - .0001165S_iF_i + .000764S_iD_i + 32.24364F_iD_i - .018725S_iF_iD_i \quad (4)$$

$$V'_{si} = V_{si} - \hat{V}_{si} = V_{si} - .055719 - .0007262S_i - 3.9698506F_i - 38.315946D_i + .021779S_iF_i + .04836S_iD_i + 961.2863F_iD_i - 1.3856094S_iF_iD_i \quad (5)$$

$$V'_{yi} = V_{yi} - \hat{V}_{yi} = V_{yi} - .0197943 + .0000072S_i - .2256959F_i - 1.8819465D_i + .000179S_iF_i + .001592S_iD_i + 45.37295F_iD_i - .0343189S_iF_iD_i \quad (6)$$

Statistical TCM System

To test the benefit of the decomposition process, two statistical models were developed. One model employed significant signal components obtained from the decomposition process, and the other model employed raw signals obtained from the sensor. Statistical multiple regression models with interactions among the independent variables were developed, employing the raw signals of the vibration and sound sensors (Model A). As shown in Table 3, the R^2 value of the model that employed the raw signal data without a decomposition process was 0.733, which indicates that 73.3 % of the observed variability of the tool wear can be explained by the independent variables. Because a full factorial analysis was performed, 128 (2^7) terms for the multiple regression models were obtained from the seven independent variables.

Table 3. Summary of the model with raw signal data (Model A)

R^2	Adjusted R^2	Observations	Root Mean Square Error	Mean of Response
.733	.439	243	.002895	.016071

Source	Df	Sum of Squares	Mean Square	F	Sig.
Model	121	.00265198	.000021	2.4909	<.0001
Error	115	.00096408	.000008		
C. Total	242	.00361607			

In the same manner, another model was developed, employing the significant components of the vibration and sound signals found in the decomposition process (Model B). The statistical test results are shown in Table 4. Accord-

ing to the test, the R^2 value of the model was 0.818, which indicates that 81.8 % of the observed variability of the tool wear can be explained by the independent variables. Because the model also employed a full factorial analysis, it had 128 (2^7) terms from the seven variables. From the comparison of its R^2 values, the model with a signal decomposition process showed 12.6% improved prediction performance over the model without the signal decomposition process.

Table 4. Summary of the model with significant signal component data (Model B)

R^2	Adjusted R^2	Observations	Root Mean Square Error	Mean of Response
.818	.617	243	.002391	.016071

Source	Df	Sum of Squares	Mean Square	F	Sig.
Model	121	.00295844	.000023	4.0735	<.0001
Error	115	.00065763	.000006		
C. Total	242	.00361607			

A statistical test was also performed to further test the significance of the improvement of Model B, which employed the significant signal components from the decomposition process, versus Model A, which employed raw signals. The following hypothesis was tested: $H_0: \phi_{Model A} = \phi_{Model B}$, $H_1: \phi_{Model A} \neq \phi_{Model B}$, where $\phi_{Model A}$ = deviation of Model A in the data set, and $\phi_{Model B}$ = deviation of Model B in the data set. From the test results shown in Tables 5, the hypothesis was rejected, which means that the mean deviation values of Model B were significantly smaller than the mean deviation values of Model A. These test results proved that there is a significant benefit of adopting a signal decomposition process in the development of a multiple regression model for the TCM system.

Table 5. Comparison of test results of Model A and Model B

	N	Mean	Standard Deviation	Standard Error Mean
Deviation Model A	243	.0015517	.0012514	.0000803
Deviation Model B	243	.0011655	.0011131	.0000714

Levene's Test for Equality of Variance		t-Test for Equality of Means				
F	Sig.	t	df	Sig. (2-tailed)	Mean Difference	Std. Error Difference
5.275	.022	3.595	484	.000	1.383E-4	8.9E-5

Results and Discussion

The model developed (Model B) was tested with a new set of data. The test included 151 data with various tool wear amounts and independent variable values. The prediction capability of the model was tested based on the criterion of detecting the rejecting tool condition, (STOP-GO), which has a practical applicability in actual manufacturing situations [39], [48]. The amount of tool wear to reject was set to 0.2mm or more. This threshold represents the maximum practical amount of flank wear in a turning operation for precision machining. This threshold for flank wear is smaller than the value suggested by ISO 3685 (0.3mm) for general machining [39], [49], [50]. Table 6 shows the results of the TCM model with 151 tests, including 62 sharp tools and 89 worn tools based on the criterion of a flank wear size larger than 0.2mm. From the 62 sharp tool tests, 10 samples were predicted to be worn tools (type II error), 83.87 % accuracy in sensing sharp tools. From the 89 worn tool tests, 5 samples were predicted to be sharp tools (type I error), 94.38% accuracy in sensing worn tools. Overall, the TCM system developed showed a 90.07% (136 out of 151) accuracy in identifying the tool conditions based on the criterion of a 0.2mm flank wear size.

Table 6. Summary of test results

		Predicted		
		Sharp Tool	Worn Tool	Total
Observed	Sharp Tool	52	10	62
	Worn Tool	5	84	89
	Total	57	94	151

Despite the increasing need for in-process tool-condition monitoring systems in metal-cutting manufacturing industries to eliminate or minimize the defective parts caused by tools that fail to be identified as “worn tools,” a limited number of studies showed the economical yet successful integration capacity of the systems proposed [51], [52]. In this study, a tri-axial accelerometer and condenser microphone, one of the most cost-effective and accessible sensors

on the market, were proposed as the sensors for an in-direct tool-monitoring system. To minimize the disadvantage of the in-direct sensing method for tool-condition monitoring—the higher integration of noise factor from the signals obtained—a series of signal-processing and statistical techniques were proposed. Following is a summary of the findings of this study.

1. By eliminating the effects of the machining parameters (spindle speed, feed rate, and depth of cut) from each vibration and sound signal, a 12.6% increase in the prediction capability was found from the statistical multiple regression model compared with the data found when disregarding the machining parameter effects on the signals.
2. The statistical multiple regression model developed showed 90.07% accuracy in detecting tool conditions from 151 tests when it was adopted as a “STOP-GO” tool with a reject flank wear amount of 0.2mm or greater.

This study showed the successful development of an in-process tool-condition monitoring system. However, there are limitations that must be resolved to integrate the tool-condition monitoring systems into current CNC technologies. The following are recommendations for further study of the tool-condition monitoring system development in CNC machines to resolve the limitations.

1. The adoption of a tri-axial accelerometer and a condenser microphone showed successful results. However, there is a need for further study for sensor mounting and shield method to eliminate the interference of chips created during the cutting process.
2. In this study, the raw signals were decomposed into six components. To test the performance of the variable ranges of signal components, testing the decompositions with different numbers of components and the correlations between the components with tool conditions is recommended.
3. In this study, limited tool conditions, machining parameters, and work piece materials were utilized. To practically use the system in industry, enlarging the number of tool conditions and machining parameters with various materials is recommended to build a larger database for the tool-condition monitoring system.

References

- [1] Singh, N. (1996). *Systems Approach to Computer-Integrated Design and Manufacturing*. New York: Wiley.
- [2] O'Donnell, G., Young, P., Kelly, K., & Byrne, G. (2001). Toward The improvement of tool-condition monitoring systems in the manufacturing environment. *Journal of Materials Processing Technology*, 119, 133-139.
- [3] Park, K.S., & Kim, S.H. (1998). Artificial intelligence approaches to determination of CNC machining parameters in manufacturing: a review. *Artificial Intelligence in Engineering*, 12, 127-134.
- [4] Purushothaman, S., & Srinivasa, Y.G. (1994). A backpropagation algorithm applied to tool wear monitoring. *International Journal of Machine Tools & Manufacture*, 34(5), 625-631.
- [5] Raj, K.H., Sharma, R.S., Srivastava, S., & Patvardhan, C. (2000). Modeling of manufacturing processes with ANNs for intelligent manufacturing. *International Journal of Machine Tools & Manufacture*, 40, 851-868.
- [6] Willow, C. (2002). A feedforward multi-layer neural network for machine cell information in computer integrated manufacturing. *Journal of Intelligent Manufacturing*, 13, 75-87.
- [7] Venkatesh, K., Zhou, M., & Caudill, R.J. (1997). Design of artificial neural networks for tool wear monitoring. *Journal of Intelligent Manufacturing*, 8 (3), 215-226.
- [8] Li, X., Dong, S., & Venuvinod, P.K. (2000). Hybrid learning for tool wear monitoring. *International Journal of Advanced Manufacturing Technology*, 16, 303-307.
- [9] Lee, J.H., Kim, D.E., & Lee, S.J. (1998). Statistical analysis of cutting force ratios for flank-wear monitoring. *Journal of Materials Processing Technology*, 74, 104-114.
- [10] Xiaoli, L., & Zhejun, Y. (1998). Tool wear monitoring with wavelet packet transform – fuzzy clustering method. *Wear*, 219, 145-154.
- [11] Chen, J. (2000). An effective fuzzy-nets training scheme for monitoring tool breakage. *Journal of Intelligent Manufacturing*, 11, 85-101.
- [12] Bradley, C., & Wong, Y.S. (2001). Surface texture indicators of tool wear – a machine vision approach. *International Journal of Advanced Manufacturing Technology*, 17, 435-443.
- [13] Karthik, A., Chandra, S., Ramamoorthy, B., & Das, S. (1997). 3D tool wear measurement and visualization using stereo imaging. *International Journal of Machine Tools & Manufacture*, 37(1), 1573-1581.
- [14] Kassim, A.A., Mannan, M.A., & Jing, M. (2000). Machine tool condition monitoring using work piece surface texture analysis. *Machine Vision and Applications*, 11, 257-263.
- [15] Bonifácio, M.E.R., & Diniz, A.E. (1994). Correlating tool wear, tool life, surface roughness and tool vibration in finish turning with coated carbide tools. *Wear*, 173, 137-144.
- [16] Choudhury, S.K., & Kishore, K.K. (2000). Tool wear measurement in turning using force ratio. *International Journal of Machine Tools & Manufacture*, 40, 899-909.
- [17] Jennings, A.D., & Drake, P.R. (1997). Machine tool condition monitoring using statistical quality control charts. *International Journal of Machine Tools & Manufacture*, 37(9), 1243-1249.
- [18] Jun, C.H., & Suh, S.H. (1999). Statistical tool breakage detection scheme based on vibration signals in NC milling. *International Journal of Machine Tools & Manufacture*, 39, 1733-1746.
- [19] Ming, L., Xiaohong, Y., & Shuzi, Y. (1999). Tool wear length estimation with a self-learning fuzzy inference algorithm in finish milling. *International Journal of Advanced Manufacturing Technology*, 15, 537-545.
- [20] Chen, S.L., & Jen, Y.W. (2000). Data fusion neural network for tool condition monitoring in CNC milling machining. *International Journal of Machine Tools & Manufacture*, 40, 381-400.
- [21] Choudhury, S.K., Jain, V.K., & Rao C.V.V. (1999). On-line monitoring of tool wear in turning using a neural network. *International Journal of Machine Tools & Manufacture*, 39, 489-504.
- [22] Dimla, D.E., Jr., Lister, P.M., & Leighton, N.J. (1997). Neural network solutions to the tool condition monitoring problem in metal cutting – A critical review of methods. *International Journal of Machine Tools & Manufacture*, 37(9), 1219-1241.
- [23] Hong, G.S., Rahman, M., & Zhou, Q. (1996). Using neural network for tool condition monitoring based on wavelet decomposition. *International Journal of Machine Tools & Manufacture*, 36(5), 551-566.
- [24] Özel, T., & Nadgir, A. (2002). Prediction of flank wear by using back propagation neural network modeling when cutting hardened H-13 steel with chamfered and honed CBN tools. *International Journal of Machine Tools & Manufacture*, 42, 287-297.
- [25] Purushothaman, S., & Srinivasa, Y.G. (1994). A backpropagation algorithm applied to tool wear monitoring. *International Journal of Machine Tools & Manufacture*, 34(5), 625-631.
- [26] Balazinski, M., Czogala, E., Jemielniak, K., & Leski, J. (2002). Tool condition monitoring using artificial

- intelligence methods. *Engineering Applications of Artificial Intelligence*, 15, 73-80.
- [27] Chungchoo, C., & Saini, D. (2002). On-line tool wear estimation in CNC turning operation using fuzzy neural network model. *International Journal of Machine Tools & Manufacture*, 42, 29-40.
- [28] Kuo, R.J. (2000). Multi-sensor integration for on-line tool wear estimation through artificial neural networks and fuzzy neural network. *Engineering Applications of Artificial Intelligence*, 13, 249-261.
- [29] Al-Habaibeh, A., & Gindy, N. (2001). Self-learning algorithm for automated design of condition monitoring systems for milling operations. *International Journal of Advanced Manufacturing Technology*, 18, 448-459.
- [30] Tansel, I.N., Mekdecı, C., & McLaghlin, C. (1995). Detection of tool failure in end milling with wavelet transformations and neural networks (WT-NN). *International Journal of Machine Tools & Manufacture*, 35(8), 1137-1147.
- [31] Wu, Y., & Du, R. (1996). Feature extraction and assessment using wavelet packet for monitoring of machining process. *Mechanical Systems and Signal Processing*, 10(1), 29-53.
- [32] Ertune, H.M., & Loparo, K.A. (2001). A decision fusion algorithm for tool wear condition monitoring in drilling. *International Journal of Machine Tools & Manufacture*, 41, 1347-1362.
- [33] Stein, J.L., & Huh, K. (2002). Monitoring cutting forces in turning: a model-based approach. *Journal of Manufacturing Science and Engineering*, 124, 26-31.
- [34] Li, X. (2002). A brief review: acoustic emission method for tool wear monitoring during turning. *International Journal of Machine Tools & Manufacture*, 42, 157-165.
- [35] Liang, S.Y., & Dornfeld, D.A. (1989). Tool wear detection using time series analysis of acoustic emission. *Journal of Engineering for Industry*, 111, 199-205.
- [36] Silva, R.G., Reuben, R.L., Baker, K.J., & Wilcox, S.J. (1998). Tool wear monitoring of turning operations by neural network and expert system classification of a feature set generated from multiple sensors. *Mechanical Systems and Signal Processing*, 12(2), 319-332.
- [37] Li, X. (2001). Real-time tool wear condition monitoring in turning. *International Journal of Production Research*, 39(5), 981-992.
- [38] Dimla, D.E.,Sr. (2000). Sensor signals for tool-wear monitoring in metal cutting operations – a review of methods. *International Journal of Machine Tools & Manufacture*, 40, 1073-1098.
- [39] Dimla, D.E., Jr., Lister, P.M., & Leighton, N.J. (1998). Automatic tool state identification in a metal turning operation using MLP neural networks and multivariate process parameters. *International Journal of Machine Tools & Manufacture*, 38(4), 343-352.
- [40] Quan, Y., Zhou, M., & Luo, Z. (1998). On-line robust identification of tool-wear via multi-sensor neural-network fusion. *Engineering Applications of Artificial Intelligence*, 11, 717-722.
- [41] Schefer, C., & Heyns, P.S. (2001). Wear monitoring in turning operations using vibration and strain measurements. *Mechanical Systems and Signal Processing*, 15(6), 1185-1202.
- [42] Abu-Mahfouz, I. (2003). Drilling wear detection and classification using vibration signals and artificial neural network. *International Journal of Machine Tools & Manufacture*, 43, 707-720.
- [43] Amick, H. (1998). Vibration Data Representation for Advanced Technology Facilities. Proceedings of 12th ASCE Engineering Mechanics Conference, La Jolla, California, May 17-20, 1998, pp. 306-309
- [44] Liang, S.Y., Kwon, Y.K., & Chiou, R.Y. (2004). Modeling the effect of flank wear on machining thrust stability. *International Journal of Advanced Manufacturing Technology*, 23, 857-864.
- [45] Klocke, F., Reuber, M., & Kratz, H. (2000). Application of a wavelet-based signal analysis for evaluating the tool state in cutting operations. *Industrial Electronics Society. IECON 2000, 26th Annual Conference of the IEEE*, 3, 1967-1972.
- [46] Wang, L., Mehrabi, M.G., & Kannatey-Asibu, E., Jr. (n.d.). Tool wear monitoring in reconfigurable machining system through Wavelet analysis, Ann Arbor: University of Michigan, Engineering Research Center for Reconfigurable Machining Systems.
- [47] Daubechies, I. (1978). Orthonormal bases of wavelets with finite support-connection with discrete filters. In J.M. Combes, A. Grossman & P.H. Tchamichian (Eds.), *Wavelets*. Berlin, NY: Springer
- [48] Dimla, D.E.,Sr., & Lister, P.M. (2000). On-line metal cutting tool condition monitoring. II: tool-state classification using multi-layer perceptron neural networks. *International Journal of Machine Tools & Manufacture*, 40, 769-781.
- [49] Kopač, J., & Šali, S. (2001). Tool wear monitoring during the turning process. *Journal of Materials Processing Technology*, 113, 312-316.
- [50] Pavel, R., Sinram, K., Combs, D., Deis, M., & Marinescu, I. (2002). Surface Quality and Tool Wear in Interrupted Hard Turning of 1137 Steel Shafts. *Proceedings of the American Society for Precision Engineering 17th Annual Meeting*. St. Louis, MO.

-
- [51] Chen, J.C. & Chen, J.C. (2002). An artificial-neural-networks-based in-process tool wear prediction system in milling operations with a dynamometer. *International Journal of Advanced Manufacturing Technology*, 25(5-6), 427-434.
- [52] Jemielniak, K. (1999). Commercial Tool Conditioning Monitoring Systems. *The International Journal of Advanced Manufacturing Technology*, 15(10), 711-721.

Biographies

SAMSON S. LEE received the B.S. degree in Naval Architecture and Ocean Engineering from Inha University, Incheon, Korea, in 1996, the M.S. and Ph.D. degree in Industrial Education and Technology from Iowa State University, Ames, Iowa, in 1999 and 2006, respectively. Currently, he is an Assistant Professor of School of Engineering and Technology at Central Michigan University. His research involves CNC machines, sensor technologies, signal processing, and artificial neural-networks. His teaching includes Engineering Graphics, Computer-Aided Design and Analysis, Computer-Aided Manufacturing, Computer Numerical Control, Tool Design, and Geometric Dimensioning & Tolerancing. Dr. Lee may be reached at samson.lee@cmich.edu

OVERVIEW AND DESIGN OF NEAR-NET FORMED SPHERICAL INVOLUTE STRAIGHT BEVEL GEARS

Haris Ligata, American Axle & Manufacturing; Henry H. Zhang, Purdue University

Abstract

Near-net formed straight bevel gears are used extensively in the automotive industry today. The design is mostly made by using tools developed for cut straight bevel gears. In this study, the forged (near-net formed) and cut straight bevel gears are compared in terms of their design, gear blank form, manufacturing process and durability (strength). In addition, current design methodology was reviewed and the necessary steps for the proper design of straight bevel differential gears (cut or net-formed) were proposed. Influence of the number of pinions, loading type (fully-released, or fully-reversed) and gear blank form on durability of the gears was investigated. Finally, modifications to the existing design approach were proposed to account for the specific shape of the forged gear blank form.

Introduction

Straight bevel gears are used for transmission of power between intersecting shafts positioned at, or close to, 90° angles. They are mostly used in relatively low-speed applications. Their most important application is in the field of automotive differentials.

Unlike other types of gears, straight bevel gears can be forged to a finished tooth shape. The forged gears have several distinct advantages over their counterparts produced by cutting. Such gears have considerably higher material properties due to the undisturbed grain flow and additional support (webbing), they are much cheaper (in production environment) and faster to manufacture, they can be of higher quality, and the geometry of their teeth is not limited by the tooling or existing tooth-generation methods.

Forging of straight bevel gears starts with the blank design, followed by the surface geometry (and micro-geometry) definition. In the next step, the die is defined as the negative of the gear surface. Finally, the hot or warm billets are forged into the gears. A process chart of straight bevel gear forging is shown in Figure 1.

This process has several challenges. First, the geometry of teeth must be accurately defined as no additional machining of teeth will be performed after forging. Next, the coordinates of the gear surface must be modified to account for thermal distortion, elastic spring-back of material and pattern ease-off. The coordinates are then exported in the appropriate form to the CNC machines used in the manufacturing of dies, or electrodes used in die production. Finally, due to the risk of thermal distortion and die wear, the theoretical and actual gear-tooth geometry must be frequently compared.

coordinates of the gear surface must be modified to account for thermal distortion, elastic spring-back of material and pattern ease-off. The coordinates are then exported in the appropriate form to the CNC machines used in the manufacturing of dies, or electrodes used in die production. Finally, due to the risk of thermal distortion and die wear, the theoretical and actual gear-tooth geometry must be frequently compared.

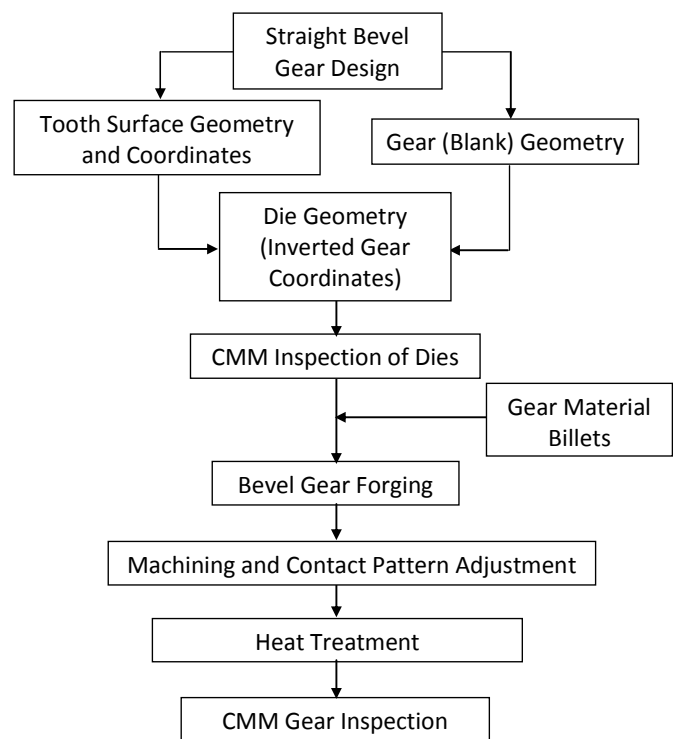


Figure 1. Process chart of straight bevel gear forging

Comparison of Cut and Near-net Formed (Forged) Straight Bevel Gears

Comparison of Design Processes

Both of the processes follow the same preliminary design, originally intended for cut gears. The process will be described in more detail in the next section. The design

stage of the cut gears finishes with the design summary, which also contains cutting-machine setup. Tooth form of the forged gears is obtained in an additional step in which specialized software is used to provide the coordinates of the surface points. The coordinates are used to design solid models of the gears, to perform contact analysis and, finally, to design and manufacture forging dies.

Comparison of Production Processes

Cutting of straight bevel gears is a natural extension of the process used in the manufacture of other types of gears. The material from the blank is generally removed by using circular cutters [1]. While the gear teeth in parallel-axis applications (spur and helical) have involute tooth forms, such a tooth form is not easily applicable to the production of straight bevel gears. The cutters for involute straight bevel gear applications would have to have slightly curved blades instead of straight ones used in the production of spur and helical gears. For that reason, the straight bevel gears are usually manufactured by using different tooth forms, most often ones being Coniflex® (with octoidal tooth form) [1-3], and Revacycle® (with circular tooth form) [1-3]. Cutting of straight bevel gears in production requires specialized machines and cutters, and blanks either forged or cut from a solid. When a small number of gears are required (prototypes), it is possible to use general milling machines for production of cut bevel gear prototypes [4].

Dies used in straight bevel gear forging are generally manufactured by using two methods, graphite electrode electro-discharge machining and direct milling. In EDM machining, a graphite electrode (shaped as a gear) is fed into the solid block of material to produce a cavity for the die. Direct milling uses end-milling on CNC milling machines. Direct milling is regarded as a more accurate process of production [5] due to the fact that it requires fewer steps for gear forging. Finally, forged bevel gears are produced by hot or cold forming of cylindrical billets in a two-part die. Cold forming yields better accuracy, but requires much larger forging presses and is usually used for smaller-sized gears. For improvement of accuracy in hot forming, cold forming (only minor deformation) can be added as an additional finishing step.

Both of the aforementioned processes (cutting and forging) are followed by additional machining that excludes toothed portion of the gears (spline broaching or rolling, pinion-bore machining and sizing, back-face machining). The final operation is heat treatment, followed by scale cleaning.

Production cycle time for the manufacture of a straight bevel gear is much shorter when forging process is used. Generally, cutting would require 4 or more seconds per tooth [6] (yielding at least 40 seconds per gear in addition to mounting and dismounting time), while forging requires approximately the same time for the manufacture of the whole gear. This advantage, in addition to the strength improvements to be mentioned later, makes the forging process a clear choice for straight bevel gear manufacture in a production environment. On the other hand, bevel gear prototypes are more efficiently produced by gear cutting, where small changes are easily implemented. The forging process often requires more than one iteration (more than one die) to properly account for heat distortion and desired contact pattern.

Comparison of Durability

An increase in strength is the biggest advantage of forged over cut gears. The bending-fatigue-strength (durability) benefit of gear forging was observed throughout history, with test results ranging widely. The two main reasons for the improvement of durability come from the favorable microstructure of the forged material and, possibly, adding webbing (reinforcement) to the forged gears.

Grain structure of the material remains mostly randomly oriented during the cutting process. Flow of the material (grain flow) during forging creates a favorable grain structure that is capable of resisting higher loads. The estimates of bending-fatigue-life benefits of forged spur gears range widely – from 30% [7], to over two times [8], to more than seven times longer [9]. The contact-fatigue improvement is also expected due to the compressive residual stress at the surface of the teeth.

The shape of the gear blanks produced by these two processes is rather different. This can be observed in Figures 2 and 3, showing cut and forged gear pairs. While the tooth surfaces of both gear pairs must remain the same to properly transfer power, the forged gear pair has additional material (web) added to its back (heel) and front (toe) portion. This additional material lowers the bending stresses further by 8 - 10% (according to FEA analyses of gears with and without webbing), which translates to up to 2 times longer bending-fatigue life. Cut gears cannot have such form because the reinforcement (webbing) would be removed during cutting.

Figure 3 compares the shape of toe and heel portions of the cut and forged gears. Closer examination of the toe portions of pinion and gear reveals another potential problem with cutting of straight bevel gears. Namely, cut parts in the

figure have very thin toe portions ($\sim 0.3\text{mm}$) and could not be used in a practical application. The possible ways to increase thickness of a toe (front) portion of the cut gears include reducing face width and reducing contact ratio. Reduction in face width increases stresses, while a decrease in contact ratio leads to a rougher transfer of power and possible premature failures due to dynamic (impact) loading.

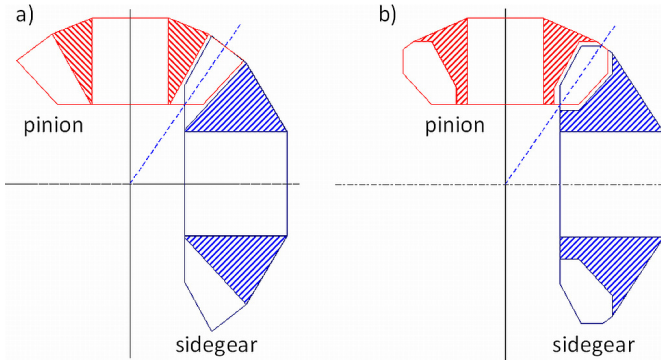


Figure 2. Example of a) cut and b) forged straight bevel gears

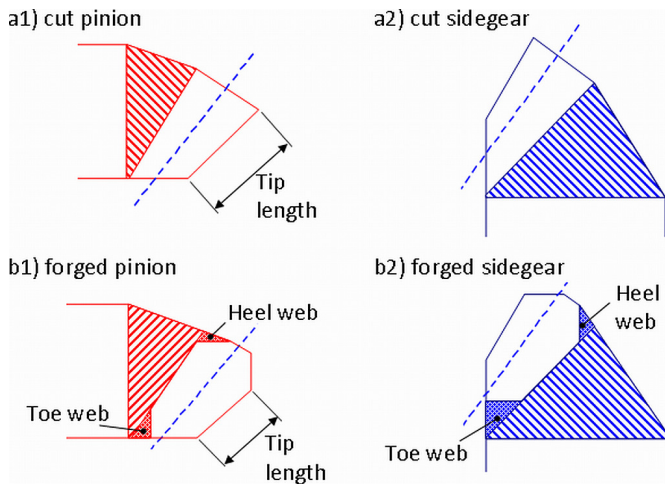


Figure 3. Comparison of the front (toe) and back (heel) portions of a) cut straight bevel gears, and b) forged straight bevel gears

In addition, forging offers more freedom in choosing the shape of the gear root region, which can lead to further benefits in terms of strength. It can also prevent or at least delay undercutting, which becomes a limiting factor for gears with long face widths.

Figure 3 shows that the length of the gear-tooth tip (tip length) on the cut gears is usually larger than the corresponding length on forged gears. In order to decrease bending stresses, designers are tempted to further decrease the

outside diameter of the gears to make more space for the reinforcement (webbing) on the back of the mating gear. This causes higher contact stresses at the tip and root regions of the gears, which can lead to premature failure due to contact fatigue (pitting and spalling). In such cases, the tip length should be extended and heel (back) webbing either reduced or completely removed.

In summary, there are considerable differences between cut and forged gears in terms of design procedures, production procedures, blank shape and performance. Forged gears have considerable benefits in almost all of these categories, and that makes forging the preferred production process in industry today. Unfortunately, a considerable portion of the existing design process was developed for cut gears. Changes to the design and development of analysis procedures will be addressed in the following parts of this work.

Design Procedure

Review of the Currently-used Design Procedures for Straight Bevel Gears

Straight bevel gears are traditionally designed by using either the Gleason program package or AGMA equations. The methods yield almost identical results, though with several differences which will be pointed out later in this section.

Gleason, as a main manufacturer of gear-cutting equipment and machines, offers a program package that, in addition to a gear blank (design geometry) summary, also offers machine setup and cutting summaries. The package consists of two main programs, A261 (used for Revacycle® design) and A201 (used for Coniflex® design). Both of the Gleason programs utilize optimization procedures based on desired bending-stress factors and tip-thickness ratios in a normal plane. Bending-stress factor is based on the general Stress-Life (S-N) curve and is used as a measure of the expected life ratio of the pinion and gear. The factors equal to 0 and 0.18 designate ‘equal stress’ (gear and pinion have equal bending stresses) and ‘equal life’ (gear and pinion have equal fatigue lives) concepts, respectively. In addition, the programs check if the gears are undercut, which is another limiting factor in the design. The undercut, as defined by Gleason, is a function of both gear and tool geometry, and for the forged bevel gears which do not use cutting tools the tool-related undercut does not play a role.

The AGMA procedure [10], [11] for design of straight bevel gears is similar to the Gleason Coniflex® straight bevel gears. The procedures yield very similar results.

Design of Straight Bevel Differential Gears

Several modifications should be made to properly apply these procedures to differential gears. They can be divided into two groups – modifications to account for the loading histories, and modifications to account for the specific geometry of the differential gears.

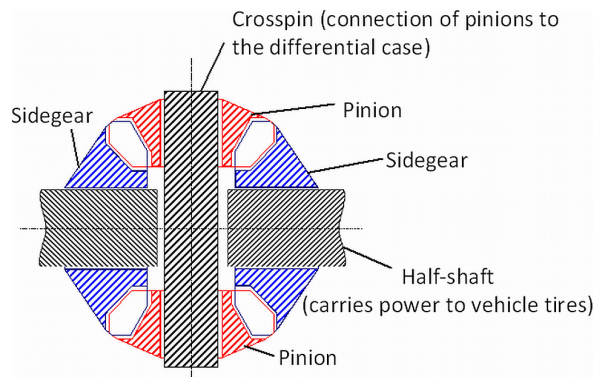


Figure 4. Straight bevel gears in a differential assembly (differential case not shown)

A typical differential consists of two side gears and at least two pinions (Figure 4). The Gleason and AGMA procedures, being written for a general application, consider a different arrangement in which one side gear and one pinion are in contact. Assuming that the gear ratio (number of side gear teeth divided by the number of pinion teeth) is equal to 1.5, such an arrangement would result in the gear-tooth load (stress) history shown in Figure 5a. The stress history of the gears in the differential assembly from Figure 4 would be represented by Figure 5b. Comparing loading of the side gears in the differential with two pinions experiences double the number of cycles. In the differential with four pinions (Figure 5c), the side gear would experience four times the number of cycles. This difference in the cycle count could simply be taken into consideration after obtaining results (stresses) from the design procedures. The modified number of cycles could be then used in the bending and contact fatigue analysis to predict the durability of the differential side gears.

Figures 5a and 5b show pinion-tooth loading histories with completely different characters. The pinion in a differential assembly contacts two side gears by the opposite sides (flanks) of the teeth. Such an arrangement results in a reversed loading (Figure 6b), which causes more damage in the root region of the teeth than the loading of the pinion in contact with one side gear (Figure 5a). Bending fatigue analysis must be evaluated by using a reversed loading cy-

cle for each pinion revolution. Due to the fact that it contacts two side gears with the opposite flanks, the differential pinion accumulates one contact fatigue cycle per rotation.

The above review of the loading histories shows that it is necessary to additionally process the results (stresses) obtained from the currently available design procedures.

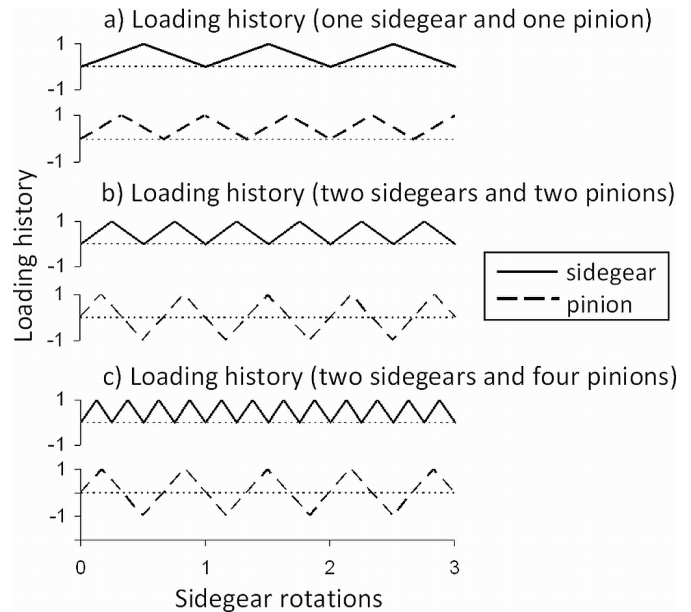


Figure 5. Loading history in the system with a) one side gear and one pinion, b) two side gears and two pinions, and c) two side gears and four pinions

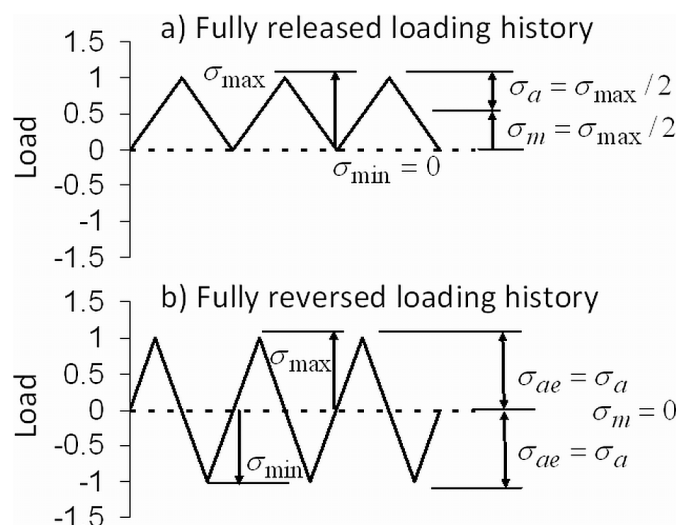


Figure 6. Example of a) fully released loading, and b) fully reversed loading

Traditionally, strength of pinion and side gear is judged by a calculating factor, proposed by Gleason,

$$F = \frac{\log\left(\frac{\sigma_g}{\sigma_p}\right)}{\log\left(\frac{N_{tg}}{N_{tp}}\right)} \quad (1)$$

where σ_g and σ_p are bending stresses on side gear and pinion, and N_{tg} and N_{tp} are their respective numbers of teeth. It is easy to show that the factor becomes equal to zero when the stresses on pinion and side gear are equal. Life of a component can be predicted by using Basquin's equation (2)

$$\sigma_{ai} = \sigma'_f (N_i)^b \quad (2)$$

$$\sigma_a = (\sigma_{\max} - \sigma_{\min}) / 2 \quad (3)$$

$$\sigma_m = (\sigma_{\max} + \sigma_{\min}) / 2 \quad (4)$$

Where N_i and σ_{ai} are predicted life (number of cycles) and alternating stress (number of cycles) of the component i , σ'_f and b are material properties, σ_a is alternating stress and σ_m is the mean stress component. Equation (2) is created by using *fully reversed loading* in which a test specimen is cyclically loaded in tension and compression (Figure 6b, $R = \sigma_{\min} / \sigma_{\max} = -1$, $\sigma_a = \sigma_{\max}$, $\sigma_m = 0$), but it can also be created by using load history with any other ratio, R . The material constants σ'_f and b determined from the tests are valid only for test stress ratio R . From the previous discussion, it is clear that the same SN curve cannot be used for pinions and side gears due to the different ratios of R of their load histories, and the stresses must first be converted to the *equivalent alternating stress* by using Goodman's equation

$$\sigma_{ae} = \frac{\sigma_a \sigma_u}{\sigma_u - \sigma_m} \quad (5)$$

where σ_u is the *ultimate tensile strength* of material. Now, σ_{ae} can be determined from Equation (2) for known (or desired) life, N_i . Assuming that ratio R is known, the maximum stress, which is also the result of the Gleason or AGMA procedures, can be obtained from

$$\sigma_{\max} = \frac{\sigma_{ae} \sigma_u}{\left(\frac{1+R}{2}\right) \sigma_{ae} + \left(\frac{1-R}{2}\right) \sigma_u} \quad (6)$$

The number of pinions in the differential assembly, n_p , can be taken into account by using Equation (7)

$$N_g = N_p n_p \left(\frac{N_{tp}}{N_{tg}} \right) \quad (7)$$

where N_g is the number of cycles that side gear teeth experience when the side gear is rotated while the differential case is held stationary (fixed). If the number of side gear revolutions with respect to differential case, $N_{g/c}$, is known, then the number of side gear cycles can be obtained as $N_g = N_{g/c} \cdot n_p$. Finally, Equation (7) can be used to calculate the number of pinion cycles for the desired number of side gear revolutions.

Equations (2), (5), (6) and (7) can be used to calculate the desired F factor by using Equation (1) and maximum stresses for side gear and pinion in place of σ_g and σ_p . As an example, let us use material 8620H (case) with properties $\sigma_f = 1790$ MPa, $\sigma_u = 1600$ MPa, and $b = -0.109$ [12].

These material properties were not correlated to the program and they are used here only for the illustration of the procedure. In general, the test results of already existing gears, preferably in a differential assembly, should be used to obtain the Stress-Life curve. The system in this example has side gear number of teeth $N_{tg} = 15$, pinion number of teeth $N_{tp} = 10$ and $n_p = 2$ number of pinions. For a desired life of 10×10^3 side gear revolutions with respect to case, the number of side gear cycles is 20×10^3 , and the number of pinion cycles is 15×10^3 (Equation (7)). Using Equation (2), the equivalent alternating stress for pinion and side gear becomes 608 MPa and 627 MPa, respectively. From Equation (6), and with ratio $R = -1$, the maximum stresses for side gear and pinion are found to be 881 MPa, and 627 MPa, respectively. Finally, the F factor for equal life of the gears is calculated to be 0.84. The value is rather high, and it could be considerably different with actual values for material (experimentally determined), and stress ratio R .

As shown in Figures 5b and 5c, the number of pinions has influence on the load history of the side gear and, accordingly, on the F factor. If the number of pinions is increased to $n_p = 3$ and $n_p = 4$, the F factor becomes 0.76 and 0.70, respectively.

It should be mentioned that the case with 4 pinions would not be used in this case because it would not be possible to place them equally (at 90° angle from each other). Generally, the possibility of equal spacing of pinions can be checked by using the following rule:

$$\frac{2N_{tg}}{n_p} = \text{integer} \quad (8)$$

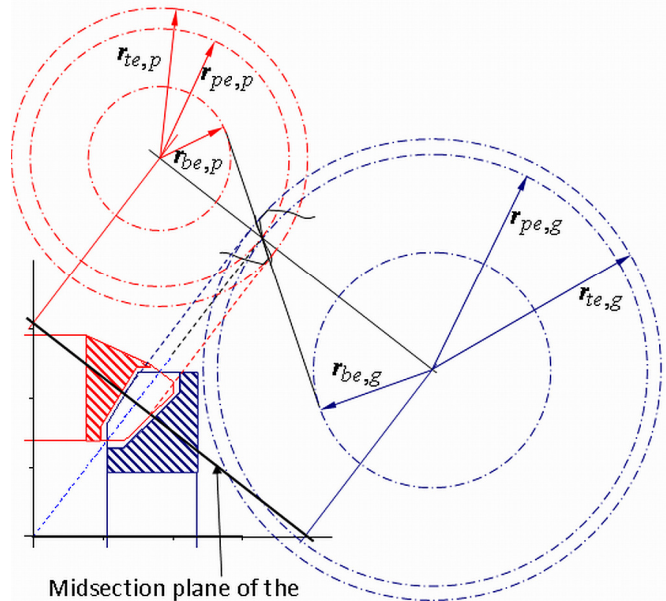
Differential gears have a considerable number of regions with high stress concentrations. For that reason, the bending stresses obtained in the design stage must be reviewed and verified by using an analytical tool capable of evaluating the effect of stress concentrations (e.g., FEM analysis). Cracks leading to premature failures often initiate in the thin, through-hardened sections at the front of the pinion and side gear or thin webbing portions at the back, where the stress state cannot be analyzed in the design stage.

Finally, the application of the currently-available design procedures comes from the root (fillet) radius of the near-net formed gears. These gears do not depend on the cutting tools and can have considerably different fillet radius from the cut gears. It would be preferable to use the actual fillet radius, which can be done by modifying the AGMA procedure [10], [11].

Contact stress on the differential gears is another important parameter in the differential gear design. These gears are heavily loaded and they rotate slowly, preventing proper elastohydrodynamic film formation. In such cases, the metal-to-metal contact leads to high contact stresses and failure due to spalling. Generally, contact stress depends on three parameters: contact line length, relative curvature (used in Hertzian contact pressure calculations) and applied load. Differential gears usually have reduced outside diameter to reduce the size requirement of the differential case window through which the gears are placed into the case. In addition, as shown in Figure 3, the tip length of the forged gears is generally shorter than the length of their cut counterparts to make space for webbing reinforcement. Neither the Gleason nor the AGMA procedures take into account the influence of shorter tip (i.e., contact line) length on the contact stresses. Both of the procedures calculate the stress factor (Gleason), or stress (AGMA) at the *Lowest Point of Single Tooth Contact (LPSTC)* or *Highest Point of Single Tooth Contact (HPSTC)*. The applied load above LPSTC or below HPSTC is carried by a single tooth. Two teeth share the load outside these borders, so it is expected that the contact stress would get lower. At the same time, the radius of curvature of a tooth surface gets progressively smaller when moving from tip towards the root. With the low tip length and small curvature radius, it is possible to obtain very high contact stress at the place where the tip of one gear touches the mating gear (*Start of Active Profile* or SAP). The contact stresses of unmodified surfaces can be calculated based on the profiles of *equivalent spur gears* (Figure 7). The curvatures, as well as sliding and rolling velocities of the equivalent spur gear teeth surfaces, can be calculated at several points along the profile [13-15] and used to understand the influence of tooth truncation and geometry on the contact stresses. Table 1 shows that the contact line (close to the

pinion root) is reduced, and contact stresses are increased when the outside diameter of the side gear is reduced from 104.8 to 93mm.

- $r_{te,p}, r_{te,g}$: equivalent tip circle radius for pinion and gear
- $r_{pe,p}, r_{pe,g}$: equivalent pitch circle radius for pinion and gear
- $r_{be,p}, r_{be,g}$: equivalent base circle radius for pinion and gear

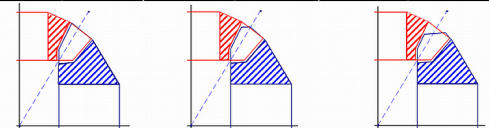


Midsection plane of the overlapping face width of pinion and gear

Figure 7. Definition of the equivalent spur gear at the midsection of the overlapping face width of pinion and gear

Table 1. Influence of the side gear outside diameter on the contact stresses

	Sidegear outside diameter [mm]					
	104.8		100		93	
	Contact stress, [GPa]	Contact length [mm]	Contact stress, [GPa]	Contact length [mm]	Contact stress, [GPa]	Contact length [mm]
Pinion SAP	2.58	15	2.85	12.3	3.47	8.3
Pinion LPSTC	2.72	18.7	3.01	17.9	3.66	13.8
Pitch line	1.5	21.9	1.5	21.9	1.64	18.1
Pinion HPSTC	2.17	17.8	2.17	17.8	2.17	17.8
Pinion EAP	1.69	15.3	1.69	15.3	1.69	15.3



Conclusion

Straight bevel gears produced by using two methods, cutting and forging, were compared in this study. Special

attention was given to straight bevel differential gears. Current design procedures were reviewed and modifications were recommended to account for the factors that influence durability of the differential gears, namely, number of planets, blank shape and root geometry. Modification of the contact analysis procedure was proposed to account for modified blank geometry (reduced outside diameter of the gears).

References

- [1] Cutting Tools for Bevel Gears”, Gleason Works, Rochester NY, 2007 (available at http://ru.gleason.com/pdfs/brochures/CutToolsBevelGears_2007_03_16_engl_000.pdf)
- [2] “Straight Bevel Gear Design”, SD3160A, Gleason Works, Rochester NY, October 1980.
- [3] Guide for Bevel Gears”, SD4155, Gleason Works, Rochester NY, 1981.
- [4] Özel, C., Inan, A., Özler, L., “An Investigation on Manufacturing of the Straight Bevel Gear Using End Mill by CNC Milling Machine”, Journal of Manufacturing Science and Engineering, 127(3), 2005.
- [5] Kawasaki, K., Shinma, K., “Design and Manufacture of Straight Bevel Gear for Precision Forging Die by Direct Milling”, Machining Science and Technology, 12(2), 2008.
- [6] Stadtfeld, J. H., “Better Bevel Gearing”, Gear Solutions Magazine, December, 2009.
- [7] Kobyskovsky, N. F., Shorochov, G. D., Socrishin, J. P., “Forging of Spur Gears on a High Speed Forge.”, Kuznechno-shtamp. Proizv. No. 8, 1967
- [8] Miller, R. C., “Pneumatic Mechanical Forging – state of the art.” The First International Conference of the Centre for High Energy Forming, University of Denver, Estes Park, Colorado, June 1967
- [9] Parkinson, F. L., “Evaluation of High Energy Rate Forged Gears With Integral Teeth.”, Western gear Corporation, Lynwood, California, U.S. Army Contract DA44-177-AMC-321(T), 1964
- [10] “Rating the Pitting Resistance and Bending Strength of Generated Straight Bevel, ZEROL Bevel and Spiral Bevel Gear Teeth”, American Gear Manufacturers Association, ANSI/AGMA 2003-B97, 2003
- [11] “Design Manual for Bevel Gears”, American Gear Manufacturers Association, ANSI/AGMA 2005-D03, 2003.
- [12] Material properties for constant amplitude stress-life analysis available from <https://www.efatigue.co>.
- [13] Colbourne, J. R., “The Geometry of Involute Gears”, Springer-Verlag, New York, 1987.
- [14] Litvin, F. L., “Gear Geometry and Applied Theory”, PTR Prentice Hall, New Jersey, 1994.
- [15] Lawcock, R., “Rolling Contact Fatigue of Surface Densified PM Gears”, Gear Solutions, 2006.

Biographies

HARIS LIGATA earned his PhD degree in 2007 from Ohio State University (Gear and Power Transmission Research Laboratory) for his work on influence of manufacturing errors on performance of planetary gear sets and transmissions. The same year he joined American Axle & Manufacturing in Detroit to work on design and development of parallel axis and bevel gears. In 2008 he was sponsored by the same company to conduct research project at Purdue University (Mechanical Engineering Technology) on design, analysis and inspection of near-net formed straight bevel gears. Since 2009, he has been back to American Axle & Manufacturing.

H. HENRY ZHANG is an Assistant Professor of Mechanical Engineering Technology at Purdue University. He has a BS degree in Mechanical Engineering (1983), first MS degree in Mechanical Engineering (Hydraulic Control, 1986), second MS degree in Mechanical Engineering (Neural Network, 1991), and PhD degree in Mechanical Engineering (1996), and third MS degree in Electrical & Computer Engineering (2007). Before he joined Purdue University, he spent 13 years in Chrysler working as a Senior Specialist of Automatic Transmission Engineering. His research interests are Mechatronics, Precision Machine Design, Digital Hydraulics, High Efficiency Hydraulics, Electric Vehicle, Powertrain / Automatic Transmission Design and Control, Time-delay System Control in Manufacturing Processes, and Multidisciplinary Correspondence Methodology Based Design.

BIT-ERROR AWARE LOSSLESS IMAGE COMPRESSION

Li Tan, Purdue University North Central; Liangmo Wang, Nanjing University of Science and Technology, China

Abstract

In this study, the authors investigated simple bit-error aware lossless compression algorithms for the compression and transmission of image data under the bit-error environment. The authors focused on enhancing two-stage lossless compression algorithms. The first stage uses a simple linear predictor, whereas at the second stage, the authors applied bi-level block coding, interval entropy coding, and standard entropy coding. The key coding parameters of the predictor, bi-level block coding, or entropy coding parameters are protected by the use of a forward error-correction scheme such as (7,4) Hamming coding. The residues from bi-level block coding or the residue offsets from Huffman coding are not protected to compromise the performance of compression ratio. These compression experiments demonstrated that when the bit-error rate (BER) in the channel is equal to or less than 0.001, the lossless compressed image can be recovered with good quality.

Introduction

Lossless image compression methods are usually required for compression and transmission of image data whenever a lossy compression approach cannot be applied. Such systems include medical imaging, remote sensing, and high-cost archiving systems. Especially in the medical data transmitting and archiving system, the usage of lossy compressed images for diagnostic purposes is prohibited by law in many countries. It is also preferred for the image data of mechanical fault diagnosis to be lossless compressed. In general, a lossless compression algorithm consists of two stages [1-6]. The first stage performs predictions to remove data correlation in order to produce residue data. The resultant residues have reduced amplitudes and are assumed to be statistically independent with an approximate Laplacian distribution [1-3]. The second stage further compresses residue data using an entropy coding algorithm—that is, Huffman coding or arithmetic coding [1-6]. Much research work has been conducted to improve the compression ratio using a more complex predictor as well as either adaptive Huffman or arithmetic coding with increased algorithm complexity. In addition, the use of lossless image compression could improve transmission throughput if the compressed image data is transmitted over a network system. However, if bit errors occur in a noisy channel during transmission or in the storage media, the recovered image will be damaged and will become useless. This outcome results from the fact

that a standard entropy coder generates instantaneous codes, which are sensitive to bit errors. Although this problem can be cured by applying a forward error-control scheme [7], adding additional bits required by the error-correction coding can significantly degrade the performance of the compression ratio and may even cause the expansion of image files. For example, if an 8-bit grayscale image is lossless compressed to 5 bits per pixel, using a (7,4) Hamming code (adding three parity bits for every 4 data bits for a single bit-error correction) for bit-error protection will increase the compressed data size by 75%; that is, 8.75 bits per pixel, which indicates image file expansion.

This study investigated two new, simple algorithms: predictive bi-level block coding and predictive interval entropy coding for bit-error aware lossless image compression. To gain a compromised compression ratio, only the prediction parameter, bi-level block coding and interval entropy coding parameters are protected by the (7,4) Hamming codes. The standard predictive entropy coding with bit-error correction was also included for comparison purposes. The authors evaluated and compared the algorithm performances in terms of the compression ratio and the peak signal-to-noise ratio (PSNR) versus the bit-error rate (BER).

Bit-error Aware Two-stage Lossless Image Compression

Figure 1 shows a block diagram of a bit-error aware two-stage lossless compression algorithm. For the first predictive stage, up to three neighboring pixels were used, as depicted in Figure 2: the left-hand neighbor (A), the upper neighbor (B), and the upper-left neighbor (C). X is the predicted pixel.

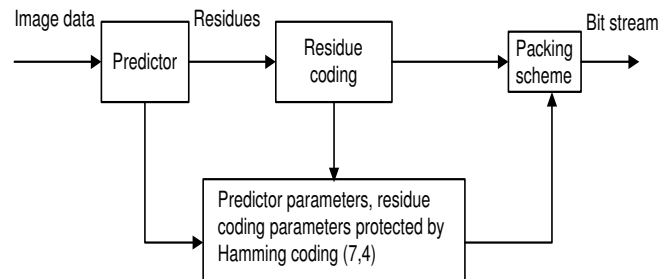


Figure 1. Bit-error Aware Two-stage Lossless Image Compression Scheme

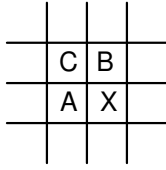


Figure 2. Neighboring Pixels for the Predictor in an Image

Predictive coding is a simple and effective method for removing redundancy of image signals [1-3]. Lossless JPEG [3], [8] contains simple predictors that use the neighboring pixels in Figure 2. The JPEG-LS standard [1] contributes an improvement to lossless JPEG prediction by adding the median filtering process. In addition, the CALIC algorithm [2] offers slightly better performance of the compression ratio by significantly increasing the amount of computational complexity. For this study, the authors adopt a linear predictor [3], which is expressed as

$$P(X) = (3A + 3B - 2C) / 4 \quad (1)$$

This predictor is effective for error resilience since the predictor output is essentially a weighted sum of neighboring pixels with coefficients less than 1. The predictor parameters required to be stored include the predictor type (3 bits), and the image pixels in the first column and first row each with an 8-bit pixel size. These parameters are further protected using the feed-forward error-correction scheme—the (7,4) Hamming coding.

As shown in Figure 1, the second stage is a residue coding stage. The authors applied bi-level block coding and interval entropy coding methods [9] to encode image residue data line by line. In each line, the key coding parameters are protected using the error control scheme and the residue samples are left as they are to gain a compromise of the compression efficiency. Therefore, the recovered image is no longer lossless when bit errors are introduced by a transmission channel.

Second-stage Residue Coding

For the residue image obtained from the prediction at the first stage, it was assumed that the redundancy of image signals was removed. The residue samples were assumed to be uncorrelated and to follow the Laplacian distribution approximately. The objective here was to develop residue coding schemes so that they would be less sensitive to the bit-error environment.

Bi-level Block Coding for Prediction Errors

The authors first applied a bi-level block coding scheme [9]. Although it is not as efficient when compared to an entropy coder in terms of lossless compression, it is more robust to bit-errors. Furthermore, after applying the feed-forward error-control scheme, the authors were able to achieve better compression efficiency since the bi-level block coder requires a smaller number of bits by the bit-error protection algorithm than the amount required by the entropy coder. Assuming that the authors code the image residue sequence line by line, the coding rules are given in Table 1.

Table 1. Bi-level Block Coding Rules

1. Divide a line of residue data with a length of $n = m \times x$ into m blocks, in which each block consists of x samples; that is, x is the block size. There are two types of blocks: the level-0 block and the level-1 block.	
$N_1 \times x + 1$ bits x data samples a. Level-1 block	$N_0 \times x + 1$ bits x data samples b. Level-0 block
2. For a level-1 block, any sample in the block requires only N_1 bits ($N_1 < N_0$ [original sample size]) to encode. Encode each sample using N_1 bits and add the prefix “1” to designate the block as the level-1 block.	
3. For a level-0 block, at least one of the samples in the block needs more than N_1 bits to encode. Encode each sample in the block using N_0 bits and add the prefix “0” to indicate the level-0 block.	

As shown in Table 1, there are two types of residue blocks, as indicated by a prefix “1” (level-1 block) and prefix “0” (level-0 block), respectively. In the level-1 block, the authors assume that each sample in the block requires N_1 bits to encode, whereas for the level-0 block, it is assumed that at least one data sample would require N_0 bits, where $N_1 < N_0$. The authors expect that the probability of level-1 blocks is much greater than the probability of level-0 blocks. Hence, the block size x and level-1 sample size of N_1 has to be determined optimally to achieve coding efficiency. Considering that the probability of the level-1 block is $P_1 = p^x$, the probability of the level-0 blocks becomes $P_0 = 1 - P_1 = 1 - p^x$, where $p = 1 - p_0$ is the probability of a

data sample requiring less than or equal to N_1 bits needing to be encoded, and p_0 (which is close to zero) is the probability of a data sample requiring more than N_1 bits and less than or equal to N_0 bits to encode. For an image residue sequence containing m blocks in which there are k level-1 blocks and $(m-k)$ level-0 blocks, the coding length and its probability are, respectively:

$$L(k) = m + N_0 x(m-k) + N_1 xk \quad (2)$$

$$P(k) = \binom{m}{k} P_1^k (1-P_1)^{m-k} = \binom{m}{k} p^{xk} (1-p^x)^{m-k} \quad (3)$$

One can obtain the average total length L_{ave} as

$$L_{ave} = \sum_{k=0}^m P(k)L(k) = (m + N_0 xm) - (N_0 - N_1) x m p^x \quad (4)$$

By minimizing the average length for a fixed N_1 , the optimal coding parameters for x^* and N_1 can be searched according to the algorithm listed in Table 2. The derivation of the algorithm is given by Tan et. al. [9].

Table 2. Algorithm for Searching the Optimal Coding Parameters

<p>1. Find N_0 for a given data sequence. Initially, set $N_1 = N_0 - 2$ and $x^* = 4$.</p> <p>2. For $N_1 = 1, 2, 3, N_0 - 1$</p> <p> Estimate p_0, the probability of the sample requiring more than N_1 bits to encode, and calculate the optimal block size:</p> $x^* = 1 / \sqrt{(N_0 - N_1) p_0}$ <p> Round up the block size to an integer value.</p> <p> If $x^* \times p_0 \leq 0.3$, calculate the average bits per sample:</p> $(L_{ave} / n)_{\min} = 2\sqrt{(N_0 - N_1) p_0} + N_1$ <p> Record N_1 and x^* values for the next comparison</p> <p> End loop</p> <p>After completing search loops, select N_1 and x^* corresponding to the smallest value of $(L_{ave} / n)_{\min}$.</p>
--

The data format of predictive bi-level block coding is proposed in Figure 3. As shown in Figure 3, the packing scheme packs the predictor type and coding parameters, which are further protected using the (7,4) Hamming codes as a header. After prediction, the residue coding process

operates line by line. Similarly, the bi-level block coding parameters are protected by Hamming coding followed by the unprotected encoded residue bit stream.

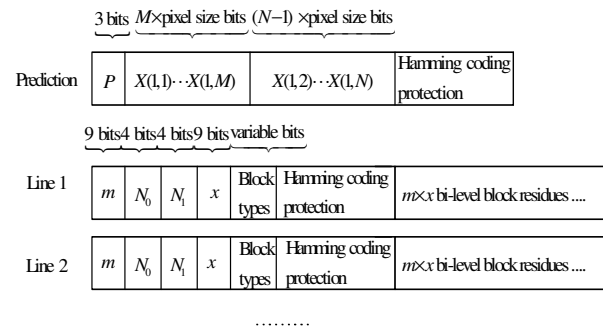


Figure 3. Data Format of Predictive Bi-Level Block Coding

Interval Entropy Coding for Prediction Errors

The interval Huffman coding (its arithmetic version can similarly be developed) can be considered as an alternative method for the second-stage image residue coding. For interval entropy coding, the authors divided each residue into the residue interval and defined its offset portion (residue offset) as

$$q(n) = \text{floor}[r(n) / 2^{(N_0 - N_1)}] \quad (5)$$

$$\text{offset} = r(n) - 2^{(N_0 - N_1)} \times q(n) \quad (6)$$

where each interval (symbol) $q(n)$, which is quantized from a residue $r(n)$, is entropy-encoded and error-protected like the coding parameters, leaving the offset bits as they are. Function $\text{floor}(x)$ runs x into the nearest integer towards negative infinity. It has been shown that the entropy coding can only compress approximately one to two bits per sample of a perfect Laplacian sequence [6]. The authors assumed that the entropy coder used in this study would achieve $N_0 - \beta$ bits per pixel, where $\beta \approx 1-2$ bits. Assuming that $q(n)$ follows a perfect Laplacian distribution, choosing the smaller symbol size N_1 for the interval entropy coder would gain approximately the same compression performance. In this study, the authors chose $N_1 = 3$, since it yielded the best experimental results. The interval Huffman codes are listed in Table 3. The data format for predictive interval Huffman coding is depicted in Figure 4.

Table 3. Interval Huffman Codes

q(n)	Interval codes	q(n)	Interval codes
0	1	+2	01011
-1	00	-3	010100
+1	011	+3	010110
-2	0100	-4	0101011

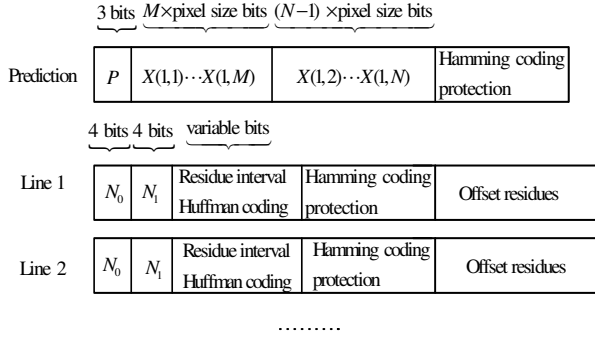


Figure 4. Data Format of Predictive Interval Entropy Coding

Standard Huffman Coding for Prediction Errors

For comparison purposes, the authors also included a standard Huffman coding scheme, as shown in Table 4, for residue coding. These Huffman codes coincide with the first nine (9) lines in the baseline JPEG algorithm for compressing the DC coefficients [8], [10]. Each image residue was encoded using a prefix for code word size, as shown in Table 4, cascaded by the binary amplitude bits. For example, to encode $-3, -2, +2$, and $+3$, the authors have **01100**, **01101**, **01110**, and **11111**, respectively. For experimental purposes, the only codeword size bits were protected using (7, 4) Hamming codes. The data format is similar to that of Figure 4.

Table 4. Huffman Codes

Code size (No.bits)	Amplitude code	Code size (No.bits)	Amplitude code
00 (0)	0	110 (5)	-31, ..., -16, +16, ..., +31
010 (1)	-1, +1	1110 (6)	-63, ..., -32, +32, ..., +63
011 (2)	-3, -2, +2, +3	11110 (7)	-127, ..., -64, +64, ..., +127
100 (3)	-7, ..., -4, +4, ..., +7	111110 (8)	-255, ..., -128, +128, ..., +255
101 (4)	-15, ..., -8, +8, ..., +15	111110 (9)	-512, ..., -256, +256, ..., +512

Performance Evaluation and Comparisons

The authors applied their proposed bit-error aware lossless compression algorithms to eight-bit grayscale images (“Lena” and “Boat”), each with the image size of 512x512 pixels. To evaluate the performances for the bit-error environment, in addition to using the average bits per pixel

(ABPP) and compression ratio (CR), the authors also used the peak signal-to-noise ratio (PSNR in dB) as an error metric for measuring the recovered image quality. The PSNR is defined as

$$\text{PSNR dB} = 20 \times \log_{10} \left(\frac{255}{\text{RMSE}} \right) \quad (7)$$

where RMSE is the root mean squared error given by

$$\text{RMSE} = \sqrt{\frac{1}{M \times N} \sum_{i=1}^N \sum_{j=1}^M [X(i, j) - \hat{X}(i, j)]^2} \quad (8)$$

Note that $X(i, j)$ represents the original pixel, while $\hat{X}(i, j)$ is the recovered pixel. Figure 5 shows the typical experimental results for compressing the “Lena” image in this study using each algorithm under the bit-error rate (BER) = 5×10^{-3} . Figure 6 depicts the compression results for the “boat” image. It can be seen that the recovered image from predictive bi-level block coding matches well with pixel levels when compared to their respective original images.

Typical compression results at BER = 10^{-3} for the ABPPs, CRs, and PSNRs are listed in Table 5. For compressing the “Lena” image, the predictive bi-level block coding offers the lowest ABPP of 5.73 bits, the highest CR of 28.38%, and the highest PSNR of 34.24 dB. Similar results were achieved for compressing the “boat” image. However, the standard predictive Huffman coding essentially has a data expansion with 8.02 bits per pixel instead of compression.

Figures 7 and 8 show experimental results of the PSNRs versus the BER for coding the “Lena” and “boat” images, respectively. The authors obtained the final PSNR based on an average of ten (10) independent runs at the given BER. When the BER > 10^{-3} , the predictive bi-level block coding algorithm offers the highest PSNR, hence producing the best signal quality. On the other hand, when the BER < 10^{-3} , the predictive interval Huffman coding and predictive Huffman coding algorithms tend to gain a better image quality at the same PSNR level. However, the predictive bi-level block coder still offers a good quality of the recovered image with the highest compression ratio. Similar results were obtained for compressing other types of images in the database used in this study.



Figure 5. Compression results using predictive bi-level block coding, predictive interval Huffman coding, and predictive Huffman coding for “Lena” Image at $BER = 5 \times 10^{-3}$

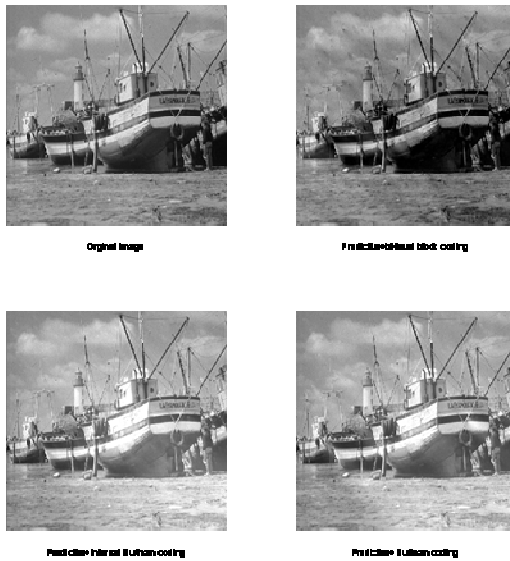
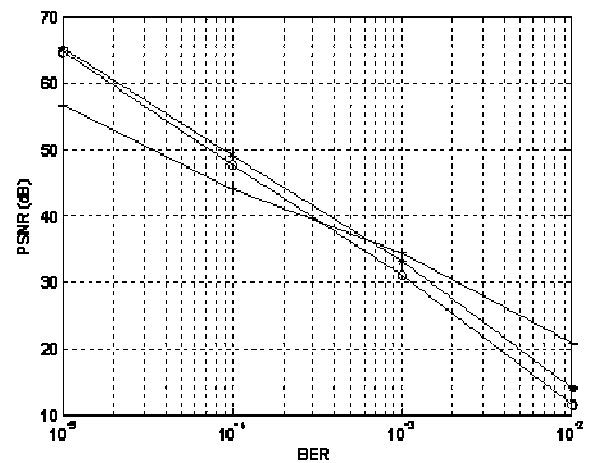


Figure 6. Compression results using predictive bi-level block coding, predictive interval Huffman coding, and predictive Huffman coding for “boat” Image at $BER = 5 \times 10^{-3}$

Table 5. Performance Comparisons of Lossless Compression at $BER = 10^{-3}$ (Each PSNR is in dB and is obtained by averaging 10 independent runs)

Algorithms	Image: Lena	Image: Boat
Predictive bi-level block coding	ABPP: 5.73 bits CR: 28.38% PSNR: 34.24 dB	ABPP: 6.12 bits CR: 23.5% PSNR: 31.72 dB
Predictive interval Huffman coding	ABPP: 6.63 bits CR: 17.13% PSNR: 30.89 dB	ABPP: 7.10 bits CR: 11.25% PSNR: 28.98 dB
Predictive Huffman coding	ABPP: 7.39 bits CR: 7.63% PSNR: 33.04 dB	ABPP: 8.02 bits CR: Expansion PSNR: 29.97 dB



+ : predictive bi-level block coding;
o : predictive interval Huffman coding;
* : standard predictive Huffman coding

Figure 7. PSNR Performances Versus the Bit-Error Rate for “Lena” Image

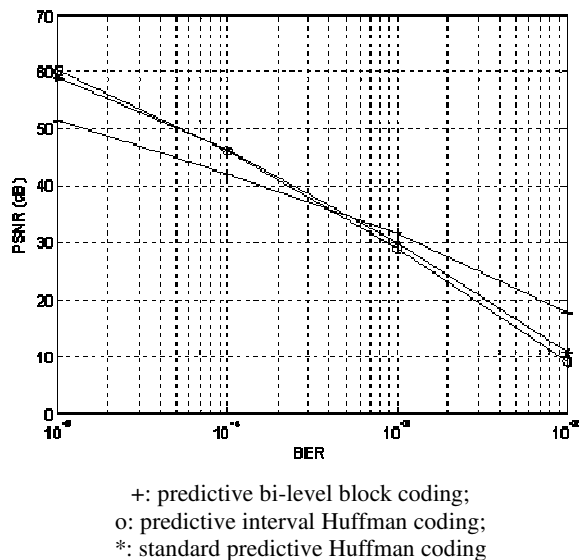


Figure 8. PSNR Performances versus the Bit-error Rate for "boat" Image

Conclusion

The authors developed the predictive bi-level block coding and interval Huffman coding algorithms for bit-error aware lossless image compression. The prediction parameters at the first stage and the bi-level block coding and interval Huffman parameters are protected by adding (7,4) Hamming error correction codes, thus leaving residues or offset residues as they are to gain a compromised compression ratio. When the bit-error rate is larger than 0.001, the developed predictive bi-level block coder offers better signal quality, as well as the highest compression ratio. On the other hand, when the bit-error rate is less than 0.001, the developed predictive interval Huffman coding tends to achieve higher signal quality. However, the predictive bi-level block coding can still maintain a commendable signal quality with a higher compression ratio.

References

- [1] M. Weinberger, G. Seroussi and G. Sapiro, "The LOCO-I Lossless Image Compression Algorithm: Principles and Standardization into JPEG-LS," *IEEE Transactions on Image Processing*, Vol. 9, No. 8, August 2000.
- [2] X. Wu and N. Memon, "Context-based, Adaptive, Lossless Image Coding," *IEEE Transactions on Communications*, Vol. 45, No. 4, April, 1997.
- [3] R. Starrosolski, "Simple Fast and Adaptive Lossless Compression Algorithm," *Softw. Pract. Exper.*, Vol.

- 37, pp. 65-91, 2007.
- [4] S. D. Stearns, L. Tan, and N. Magotra, "Lossless compression of waveform data for efficient transmission and storage," *IEEE Transactions on Geoscience and Remote Sensing*, Vol. 31, No. 3, pp. 645-654, May 1993.
- [5] S. D. Stearns, "Arithmetic Coding in Lossless Waveform Compression," *IEEE Transactions on Signal Processing*, Vol. 43, No. 8, pp. 1874-1879, 1995.
- [6] S. D. Stearns, L. Tan, and N. Magotra, "A Bi-Level Coding Technique for Compressing Broadband Residue Sequences," *Digital Signal Processing*, Vol. 2, No. 3, pp. 146-156, July 1992.
- [7] S. Lin, D. Jr. Costello, *Error Control Coding: Fundamentals and Applications*. Prentice Hall, Inc., Englewood Cliffs, NJ, 1983.
- [8] Z. Li, M. S. Drew, *Fundamentals of Multimedia*. Prentice Hall, Upper Saddle River, NJ 07458, 2004.
- [9] L. Tan, J. Jiang, Y. Zhang, "Bit-error Aware Lossless Compression of Waveform data," *IEEE Signal Processing Letters*, Vol. 17, No. 6, pp. 547-550, June 2010.
- [10] L. Tan, *Digital Signal Processing: Fundamentals and Applications*. Elsevier/Academics, 2008.

Biographies

LI TAN is currently with the College of Engineering and Technology at Purdue University North Central, Westville, Indiana. Previously, he was a full professor at DeVry University, Atlanta, Georgia. Dr. Tan is a senior member of IEEE. His research interests are in the areas of active noise control, digital signal processing, digital communications, and mechanical systems and signal processing. He authored and coauthored three textbooks: *Digital Signal Processing: Fundamentals and Applications* (Elsevier/Academic Press, 2008), *Fundamentals of Analog and Digital Signal Processing* (AuthorHouse, 2008), and *Analog Signal Processing and Filter Design* (Linus Publications, 2009). He is the holder of a granted US patent. Dr. Tan may be reached at lizhetan@pnc.edu

LIANGMO WANG is currently a professor at School of Mechanical Engineering, Nanjing University of Science and Technology, Nanjing, China. His research interests are in the areas of vehicle dynamics and control, structural optimization, structural dynamics, and signal processing. He has many years of working experience in the automobile industry. Dr. Wang may be reached at liangmo@mail.njust.edu.cn

ANALOG BREAKTHROUGH DETECTION USING LASER-INDUCED, THERMAL DIFFUSION SHOCK WAVES

Jun Kondo, University of Hartford; Saeid Moslehpour, University of Hartford; Hisham Alnajjar, University of Hartford

Abstract

The efficiency of a jet engine is improved by increasing the temperature in the engine combustion components. Combustion-chamber temperatures have increased up to 1600°C over the past decade [1]. Therefore, jet-engine combustion components must deal with high temperatures. Free-air-flow cooling holes are critical for cooling the components. But the process of drilling cooling holes has numerous problems, and “back wall strike” is the major problem that must be solved. This project presents innovative approaches to designing controllers for the laser percussion-drilling process to determine the exact moment of breakthrough to eliminate “back wall strike”, which damages the adjacent surface of jet-engine turbine components. The PCB 106B pressure sensor was used to measure thermal diffusion shock waves, and National Instruments LabVIEW software was used to establish control algorithms. The test results clearly indicated that the second derivative of the PCB 106B pressure sensor output was positive at the heating stage of the laser percussion-drilling process, and negative at the cooling stage of the drilling process. Therefore, it was concluded that the second derivative of the pressure sensor output indicated nothing but temperature conditions of the sample during the laser percussion-drilling process. Right after the exact moment of breakthrough, the temperature of the sample dramatically decreased. Therefore, the moment of breakthrough was precisely determined by processing the output of the PCB 106B pressure sensor, which was used for measuring thermal diffusion shock waves.

Introduction

The laser percussion-drilling process at the Connecticut Center for Advanced Technology (CCAT) is shown in Figure 1. The laser beam was generated by the neodymium-doped yttrium aluminum garnet (Nd: YAG) laser of the Convergent Prima P-50 laser drilling machine at CCAT. The laser beam passed through the center of the copper nozzle, and impinged upon the surface of a Waspalloy steel plate sample. The angle between the laser and sample was 20 degrees, which is the standard for cooling hole drilling for jet-engine turbine blades. After a few percussion-drilling operations, the laser beam started penetrating the sample and making a small diameter hole on the sample surface;

this process is known as “partial breakthrough.” At the next laser shot, the laser beam completely penetrated the sample; this process is known as “full breakthrough.” But subsequent laser shots continuously drilled the adjacent sample surface after full breakthrough in the laser percussion-drilling process of actual jet engine turbine blades. This unavoidable process is known as “back wall strike.” In order to diminish the effect of back wall strike, Loctite Hysol 7901 polyamide hot melt might be injected in cavities of jet-engine turbine blades. But the adjacent sample surface might receive serious surface damage despite the existence of the hot melt.

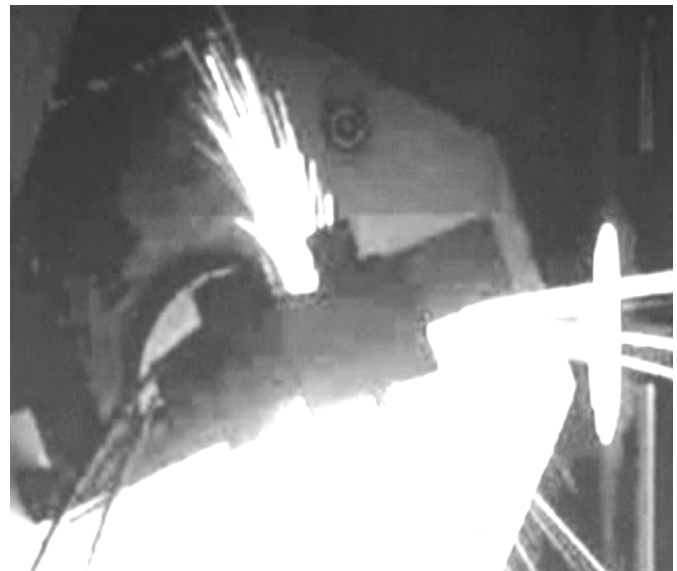


Figure 1. Laser Percussion-drilling Process at Connecticut Center for Advanced Technology (CCAT)

In order to solve this problem, the exact moment of full breakthrough must be detected by the sensor, and the controller must turn off the laser immediately after the exact moment of full breakthrough. Many approaches have been developed to minimize the effect of back wall strike. Full breakthrough can be detected by frequency changes of the drilling sound signatures using the Fast Fourier Transform (FFT). Also, it can be detected by spectrum changes of the percussion-drilling arc. It can also be detected by a video camera, which is mounted to view the area being drilled through a path coaxial with the drilling laser beam [2]. In this project, the PCB-106B pressure sensor was used to

measure “Laser-induced, Thermal Diffusion Shock Waves” to monitor temperature conditions of the sample in order to detect the exact moment of full breakthrough. The output of the PCB-106B pressure sensor was differentiated twice to show more detailed information about the pressure sensor output. The objective was to show the distinct signal, which indicated the clear evidence of the exact moment of full breakthrough when the laser beam completely penetrated the sample.

Related Research

The effects of Laser-induced, Thermal Diffusion Shock Waves have been investigated and the fundamental equations were established by Sorasak Danworaphong, Gerald J. Diebold and Walter Craig in the book “Laser Induced Thermal Diffusion Shock Waves.” When a neodymium-doped yttrium aluminum garnet (Nd: YAG) laser induces a thermal diffusion shock wave, the thermodynamic properties—speed U , density ρ , and pressure P —are dramatically different before the shock front and after the shock front. The figure of the shock front is shown in Figure 2 [3].

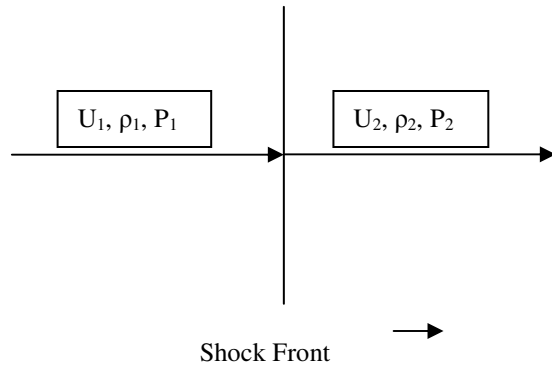


Figure 2. “Shock Front”

Thermal diffusion shock waves have several properties identical to fluid shock waves generated by supersonic flight [4]. The difference between thermal diffusion shock waves and fluid shock waves is as follows [4]:

1. Thermal diffusion shock waves depend on the existence of externally-imposed temperature gradients, while fluid shock waves have no such requirement.
2. Thermal diffusion shock waves always appear as a pair of identical shock fronts that propagate in opposite directions.
3. The dissipating force is viscous damping and mass diffusion in thermal diffusion shock waves. Therefore, the speed of thermal diffusion shock waves will be eventually equal zero even in the absence of mass diffusion.

The thermal diffusion shock waves and the mass diffusion shock waves are governed by the following equation [4]:

$$\frac{\partial c(z,t)}{\partial t} = \alpha \frac{\partial}{\partial z} \{c(z,t)[1 - c(z,t)] \cos z\} + \frac{\partial^2 c(z,t)}{\partial z^2} \quad (1)$$

The significance of this equation is stated as follows [4]:

1. The first term corresponds to thermal diffusion shock waves, and the second term corresponds to mass diffusion shock waves.
2. The sinusoidal function governs the first term that represents thermal diffusion shock waves.
3. α is the thermal diffusion factor that governs the dominance of thermal diffusion shock waves over mass diffusion shock waves, and expressed as follows:

$$\alpha = \frac{D' T_0}{D} \quad (2)$$

D = Mass Diffusion Constant
 D' = Thermal Diffusion Constant
 T_0 = Temperature

Initial Research

Temperature changes are directly related to the progress of the laser percussion-drilling process. The temperature of the sample dramatically increases when the laser impinges upon the sample surface, and it dramatically decreases right after full breakthrough. In order to prove the relationship between the output of the pressure sensor and temperature conditions of the sample, the following experiments have been conducted in a laboratory. A cigar lighter was ignited, and the flame was passed in front of the PCB106B52 pressure sensor, as shown in Figure 3. Then it was moved away from the sensor and extinguished. The results are shown in Figure 4, and summarized as follows:

1. When the flame was passed in front of the PCB106B52 pressure sensor, the output of the second derivative was positive.
2. When the flame was moved away from the PCB106B52 pressure sensor, the output of the second derivative was negative.

Therefore, it was considered that it might be possible to measure the thermal diffusion shock waves using a PCB106B series pressure sensor at the laser percussion-drilling process at CCAT. The major difference between this lab experiment and the laser percussion-drilling experi-

ment at CCAT was the magnitude of the thermal diffusion shock waves. The magnitude was approximately 3.6kPa in the lab experiment and approximately 81kPa in the laser percussion-drilling process at CCAT. The PCB-106B52 pressure sensor was used in this lab experiment instead of the PCB106B pressure sensor because the PCB-106B52 pressure sensor provides the highest sensitivity and the lowest resolution in the PCB-106 series of pressure sensors [5].



Figure 3. PCB106B52 Pressure Sensor Setup

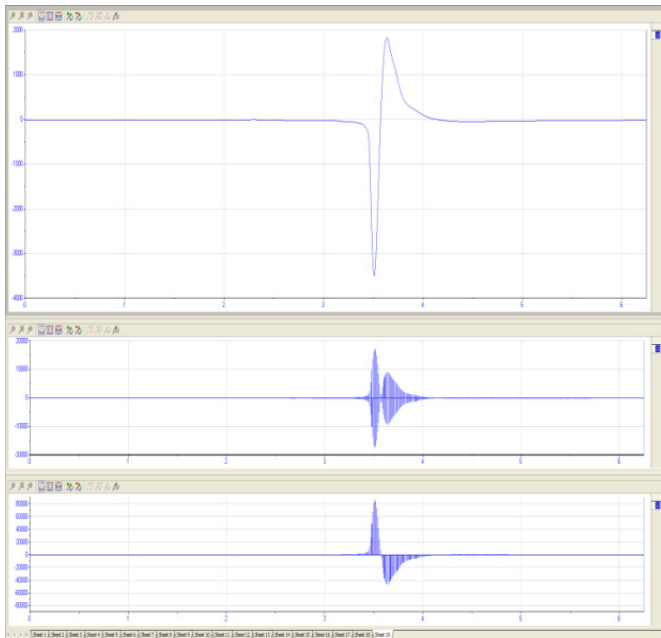


Figure 4. PCB106B 52 Pressure Sensor Output (top) First Derivative (middle) and Second Derivative (bottom) X Axis: Time in Second Y Axis: Sensor Output in Pa

Partial Breakthrough and Full Breakthrough

In the percussion-drilling process, the laser beam penetrates the sample after drilling repeatedly and makes a small diameter hole. This condition is called partial breakthrough. At the following laser shot, the laser beam completely penetrates the sample and makes a big diameter

hole. This condition is called full breakthrough. These conditions are shown in Figure 5. The diameters of these holes can be estimated using the diameter of calibration dots.

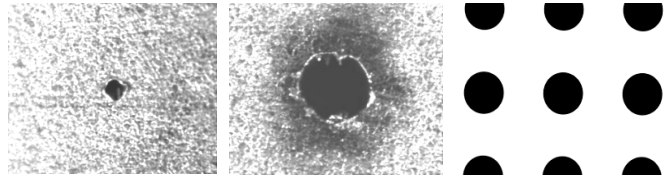


Figure 5. Partial Breakthrough, Full Breakthrough and Calibration Dots (0.25mmØ)

Methodology

The laser percussion-drilling process setup at CCAT is shown in Figure 6. The laser beam was generated by the neodymium-doped yttrium aluminum garnet (Nd: YAG) laser of the Convergent Prima P-50 laser drilling machine at CCAT. The laser beam passed through the center of the copper nozzle and impinged upon the surface of a Waspalloy steel plate sample. The thermal diffusion shock waves were measured by the PCB-106B pressure sensor that was placed under the sample. Also, the penetrating laser power was measured by the breakthrough detector that was placed above the sample in order to confirm the moment of breakthrough that was detected by the PCB-106B pressure sensor. After full breakthrough, subsequent laser shots continuously drilled the adjacent sample surface in the actual laser percussion-drilling process, and it is the major problem that must be solved. In order to eliminate the effect of “back wall strike”, the exact moment of full breakthrough must be detected by processing the output of the PCB-106B pressure

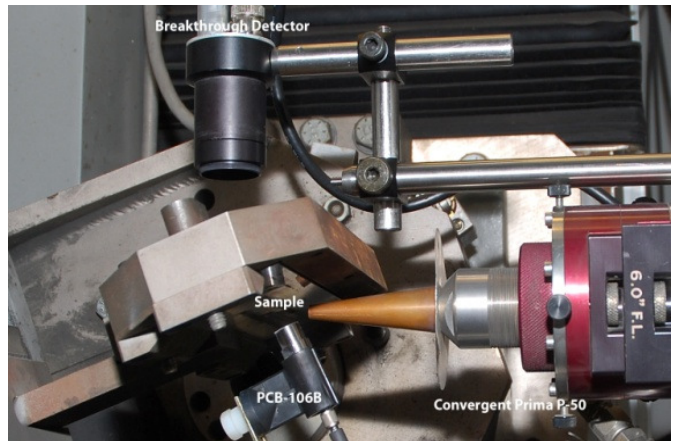


Figure 6. Laser Percussion-drilling Process Setup at Connecticut Center for Advanced Technology (CCAT) Breakthrough Detector (top) and PCB 106B Pressure Sensor (bottom)

sensor, and the controller must turn off the laser immediately after the exact moment of full breakthrough to prevent the excessive laser drilling process that damages the adjacent sample surface.

Apparatus

The analog approach uses LabVIEW to differentiate the PCB106B pressure sensor output twice to get the second-derivative output that indicates temperature conditions of the sample during the laser percussion-drilling process. When the laser beam impinges upon the sample surface, the sample is in the heating stage, and the second-derivative value becomes positive. When the laser beam completely penetrates the sample after full breakthrough, the sample is in the cooling stage, and the second-derivative value becomes negative. When the absolute value of the negative second-derivative value exceeds a predetermined threshold value, it is considered full breakthrough and the resulting signal shows a clear indication of full breakthrough to turn off the laser to prevent “back wall strike.” The National Instruments PXI-4462 Dynamic Signal Acquisition Device and PXIe-1062Q PXI Express Chassis were used for this purpose, and are shown in Figure 7.



Figure 7. National Instruments PXI-4462 Dynamic Signal Acquisition Device (the first module from the right) and PXIe-1062Q PXI Express Chassis

The LabVIEW Breakthrough Detection program is shown in Figure 8 and consists of the following four major DAQmx tasks:

1. “Timing” configures the number of samples to acquire.
2. “Start Task” transitions the task to the running state to begin the measurement.
3. “Read” reads the sampled data from the task. “Clear Task” clears the task. Also, it aborts the task if necessary.

This program differentiates the PCB-106B pressure sensor output twice, and the second derivative value is compared against the predetermined threshold value to detect the moment of full breakthrough. Also, it can record the following six signals in the Technical Data Management-Streaming (TDMS) format and save the data on the hard drive:

1. Output of the PCB-106B pressure sensor
2. First derivative of the output of the PCB-106B pressure sensor
3. Second derivative of the output of the PCB-106B pressure sensor
4. Results of the breakthrough detection function
5. Laser power output from the Convergent Prima P-50 laser drilling machine
6. Breakthrough detector output

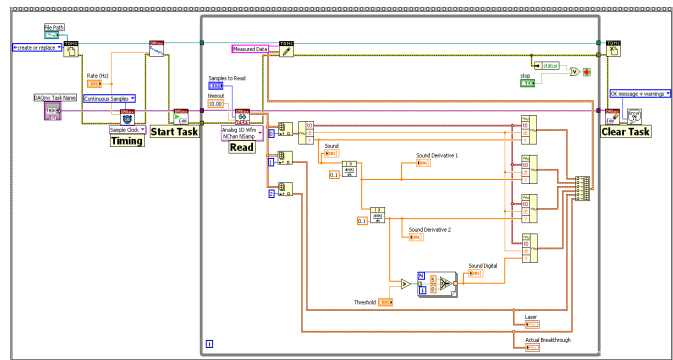


Figure 8. LabVIEW Breakthrough Detection Program

Results

Pressure Sensor Output

The pressure sensor output and the breakthrough detector output are shown in Figure 9. The top line indicates the output of the PCB106B pressure sensor in Pa. The bottom line indicates the output of the breakthrough detector in volts. The horizontal line indicates the time in seconds. In this experiment, the data were collected using a sampling rate of 10kHz. So signals above 5kHz, which was the frequency range of the system gas noise, were all eliminated according to the Nyquist-Shannon sampling theorem [6]. Therefore, system gas noise from the copper nozzle was not observed. The total number of laser shots was seven, and the laser power was 13 joules per shot. Partial breakthrough occurred at the third shot, and full breakthrough occurred at the fourth shot. The pressure sensor output shows the distinct vertical line which represents the thermal contact between the laser beam and the sample. At full breakthrough on the fourth shot, the vertical line disap-

pears. Therefore, the pressure sensor output directly indicates the moment of full breakthrough without any analysis tools.

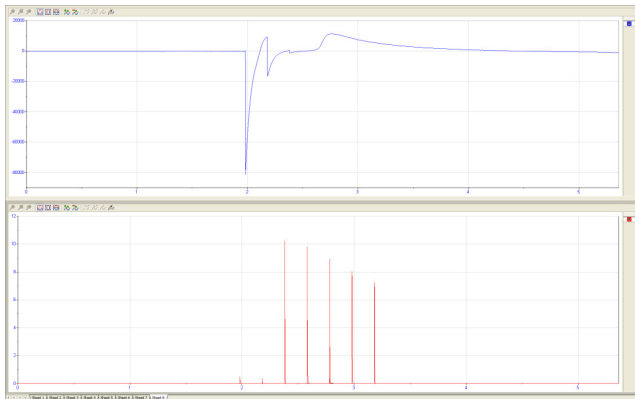


Figure 9. Pressure Sensor Output (top) and Breakthrough Detector Output (bottom) X Axis: Time in Second Y Axis: Sensor Outputs in Pa (top) and Voltage (bottom)

The operations of the seven laser shots are summarized as follows:

1. The first laser shot impinged upon the sample surface and had the highest negative pressure.
2. The second laser shot had the second highest negative pressure.
3. The third laser shot partially penetrated the sample (partial breakthrough) and had the third highest negative pressure.
4. The fourth laser shot fully penetrated the sample (full breakthrough), and the pressure sensor did not show any vertical response.
5. The fifth laser shot cleaned up the existing hole, and the pressure sensor did not show any vertical response.
6. The sixth laser shot further cleaned up the existing hole.
7. The seventh laser shot further cleaned up the existing hole.

First Derivative of Sensor Output

The first derivative of the output from the PCB106B pressure sensor is shown in Figure 10. It is symmetrical against the horizontal axis, and the absolute value was consistently close to zero between the third shot (partial breakthrough) and the fourth shot (full breakthrough).

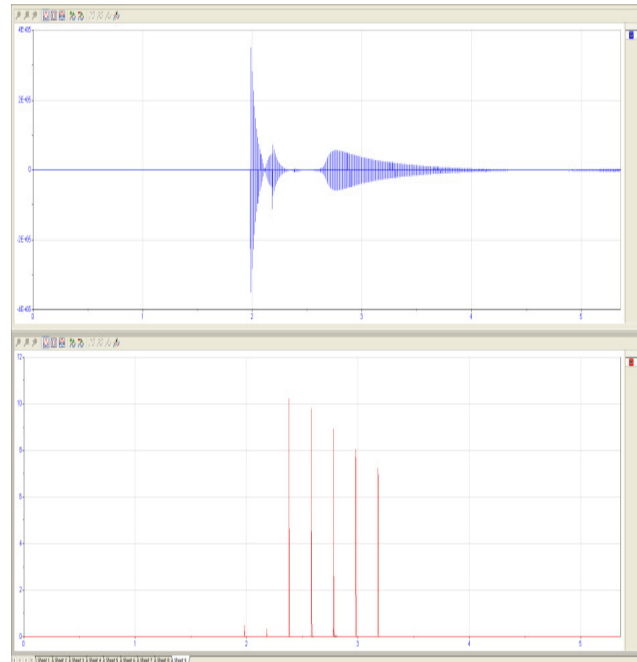


Figure 10. First Derivative (top) and Breakthrough Detector Output (bottom) X Axis: Time in Second Y Axis: Sensor Outputs in Pa and Voltage

Second Derivative of Sensor Output

The second derivative of the output from the PCB106B pressure sensor is shown in Figure 11. After the first distinct vertical line that represents the thermal contact between the laser beam and the sample, the sample temperature dramatically changes, and the output of the second derivative was positive at the heating stage and negative at the cooling stage. Therefore, the second derivative of the pressure sensor output was nothing but temperature conditions of the sample. Right after full breakthrough, the values of the second derivative gradually reached the minimum value. Therefore, the moment of full breakthrough can be detected when the output of the second derivative becomes less than a predetermined minimum threshold value. At this point, the output of the breakthrough detection circuit turns off the laser to prevent subsequent “back wall strike.” The LabVIEW breakthrough detection program, which is shown in Figure 8, was implemented using this approach and is particularly useful when the conditions of the laser percussion-drilling process are continuously changing. These conditions include the angle between the laser beam and the sample, the thickness of the sample, and the surface condition of the sample. Because the sensor output is based only on amplitudes of thermal diffusion shock waves during the laser percussion-drilling process, breakthrough detection is determined by the temperature conditions of the sample and is not affected by other factors.

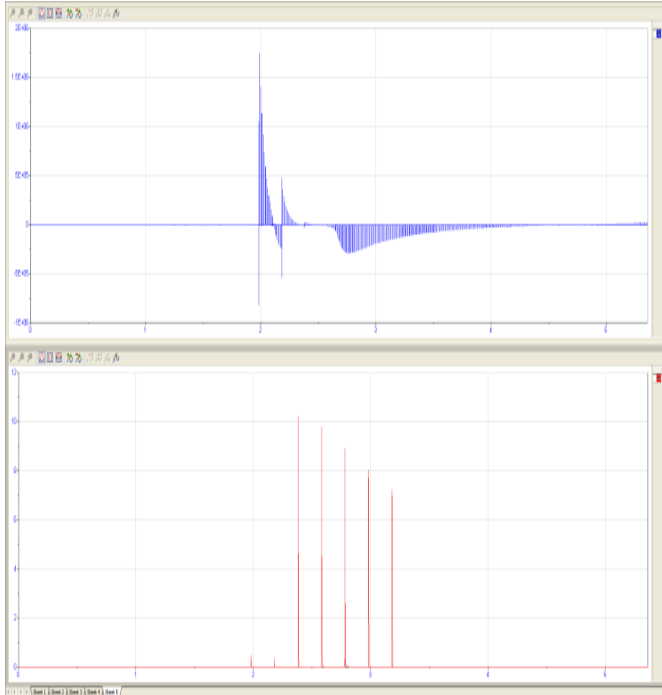


Figure 11. Second Derivative (top) and Breakthrough Detector Output (bottom) X Axis: Time in Second Y Axis: Sensor Outputs in Pa and Voltage

Discussion

Overload Condition

The results of the experiments with laser-induced, thermal diffusion shock waves are often mistaken to be the results of overload conditions. An overload condition occurs when the power supply of the sensor is not able to supply sufficient voltage to the sensor. When the PCB106B pressure sensor is used with the National Instruments PXI-4462 dynamic signal acquisition device, the power supply can provide up to 5 volts for the PCB106B pressure sensor. The power supply voltage consumption at the first laser shot in Figure 9 was calculated as follows:

Sensitivity of the PCB106B pressure sensor: 43.5 mV/kPa
 Maximum negative pressure in Figure 9: -81.099kPa
 Maximum supply voltage required to operate the PCB106B sensor: $43.5 \text{ mV/kPa} * 81.099\text{kPa} = 3,528\text{mV} = 3.528\text{V}$

It was under 5 volts. Therefore, it was proven that the acquisition device supplied adequate voltage to the PCB106B pressure sensor. An example of an overload condition is shown in Figure 12. The sampling rate was 100k samples/second, and the frequencies below 50KHz,

which was the major frequency range of system gas noise. The power supply voltage consumption at the first laser shot in Figure 12 was calculated as follows:

Sensitivity of the PCB106B52 pressure sensor: 725mV/kPa
 Maximum negative pressure at the first laser shot in Figure 12: -13.316kPa
 Maximum supply voltage required to operate the PCB106B-52 sensor: $725 \text{ mV/kPa} * 13.316\text{kPa} = 9,654\text{mV} = 9.654\text{V}$

It was over 5 volts. Therefore, it was proven that the acquisition device did not supply adequate supply voltage to the PCB106B52 pressure sensor, and an overload condition occurred.

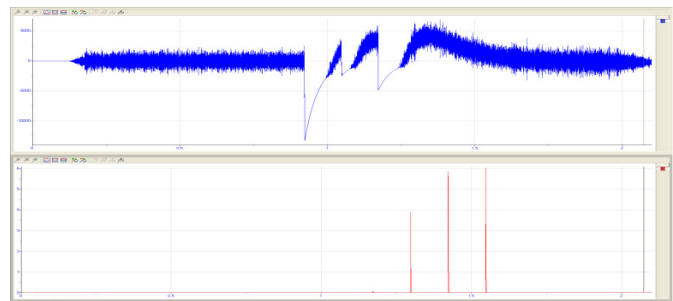


Figure 12. Overload Condition; PCB106B5 Pressure Sensor Output (top) and Breakthrough Detector Output (bottom)

Pressure Sensor versus Microphone

The PCBD20 ICP array microphone had been used since 2006. But it was damaged by high pressure caused by the percussion-drilling process in the summer of 2007. Therefore, the PCB106B-series pressure sensors were recommended by PCB engineers. They decisively said that pressure caused by the percussion-drilling process was beyond the microphone's measurement range. A system based on a microphone was inappropriate for the percussion-drilling process because the maximum pressure reaches 81.099kPa at 1 inch from the sample. This pressure is approximately 80 percent of the theoretical limit pressure of 101.325kPa at 1 atmosphere environmental pressure [7]. Even if the distance is increased twice to decrease the pressure to 20.275kPa, it is still over the allowable maximum pressure, 15.9kPa, of the PCB377A12 microphone that has a sensitivity of 0.25mV/Pa [5]. In addition, PCB377A12 does not provide high sensitivity for the laser-induced, thermal-diffusion shock waves as the PCB106B pressure sensor does. The PCB377A12 microphone is one of the lowest sensitivity microphones made by PCB and is used in a high-pressure environment. Therefore, the pressure sensor must be used in the laser percussion-drilling process at CCAT to provide

both the high-pressure resistance and the high sensitivity for the laser-induced, thermal-diffusion shock waves to establish a consistently reliable control system that works under any conditions.

Cleanup Shots

After full breakthrough, the resolidified material might be left in the hole. A photograph of resolidified material is shown in Figure 13. The size of it can be estimated using the diameter, 0.25mm, of the calibration dots. In order to take out the resolidified material from the hole, cleanup shots are required after full breakthrough. But cleanup shots also continuously drill the adjacent sample surface after full breakthrough; it is yet to be determined whether or not the laser shots should be continued at that point. Therefore, the minimum amount of laser power, which is required to take out the resolidified material from the hole, is predetermined, and should be consumed for cleanup shots after full breakthrough.

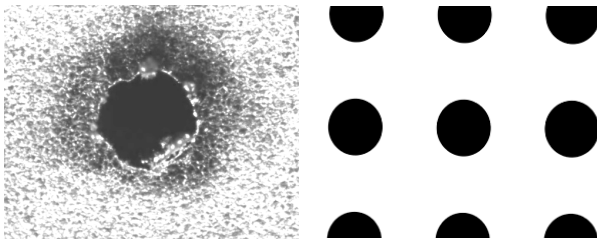


Figure 13. Resolidified Material and Calibration Dots (0.25mm Ø)

Next Research Phases

The first fundamental experiments have been accomplished in a limited time period to prove that this method is feasible. The future objectives of this project are as follows:

Pattern Matching Algorithm

In this project, the moment of breakthrough was simply determined using the threshold function, which is shown in Figure 8. The moment of breakthrough can be also determined using the National Instruments pattern matching algorithm. Mr. Michael Callahan of the University of Illinois at Urbana-Champaign successfully controlled his patient's wheelchair using a similar approach in 2005 [8]. He interpreted his patient's nerve impulse signals as appropriate control signals for his wheelchair.

Various Conditions

In the actual laser percussion-drilling process, the turbine blade is always rotating and all parameters are continuously changing. But the exact moment of breakthrough has to be determined, regardless of these unsteady conditions. Only 20-degree angle shot has been used in this project. So varieties of angles will be tested. The tested Wasp alloy samples have a thickness of only 0.05 inches. So thicker samples will be also tested. It is known that the thermal coating on the sample surface dramatically increases the sound signature. So thermal coated samples will be tested.

Summary

The PCB106B pressure sensor output showed distinctive patterns before partial breakthrough, at partial breakthrough, at full breakthrough, and after full breakthrough, as shown in Figures 9 – 11. Therefore, the system successfully detected the moments of breakthrough using the analog approach. Also, these results proved that breakthrough can be detected using a simple threshold value and also complex algorithms to analyze the second derivative value. Because all drilling conditions are constantly changing during actual fabrication of jet-engine turbine blades, samples will be tested under many different conditions to prove a consistently reliable control system that works under any conditions.

References

- [1] K. Verhoeven, "Modelling Laser Percussion Drilling," Eindhoven University, Netherlands, 2004. <http://alexandria.tue.nl/extra2/200412856.pdf>
- [2] T. Vanderwert, Terry, "Breakthrough Detection," Industrial Laser Solution, 2006, 12.
- [3] S. Danworaphong, G. Diebold, and W. Craig, "Laser Induced Thermal Diffusion Shock Waves," VDM Verlag Dr. Müller, Saarbrücken, Germany, 2008.
- [4] S. Danworaphong, W. Craig, V. Gusev, and G. Diebold. "Thermal Diffusion Shock Waves," Brown University, Providence, RI, 2008. <http://www.math.mcmaster.ca/craig/SoretIIBNew.pdf>
- [5] "PCB Piezotronics," PCB, Depew, NY. <http://www.pcb.com/products/>
- [6] "Nyquist-Shannon Sampling Theorem," Wikipedia. http://en.wikipedia.org/wiki/Nyquist-Shannon_sampling_Theorem
- [7] "Sound Pressure," Wikipedia. http://en.wikipedia.org/wiki/Sound_pressure

-
- [8] “UIUC Innovators Develops Mind-Computer Interface Using NI LabVIEW,”
<http://zone.ni.com/devzone/cda/pub/p/id/178>

Biography

JUN KONDO received his Master of Business Administration and Master of Engineering in Mechanical Engineering from University of Hartford in 1998, his Master of Engineering in Electrical Engineering from University of Hartford in 2010. Presently, he is pursuing his Ph.D. degree in Electrical Engineering at the University of Connecticut. He may be reached at kondo@hartford.edu.

SAEID MOSLEHPOUR is an Associate Professor in the Electrical and Computer Engineering Department in the College of Engineering, Technology, and Architecture at the University of Hartford. He holds PhD (1993) from Iowa State University and Bachelor of Science, Master of Science (1990), and Education Specialist (1992) degrees from University of Central Missouri. His research interests include logic design, CPLDs, FPGAs, electronic system testing and distance learning. He may be reached at moslehpu@hartford.edu.

HISHAM ALNAJJAR is a Professor of Electrical and Computer Engineering at the University of Hartford, Connecticut (USA), where he is also the Associate Dean of the College of Engineering, Technology, and Architecture (CETA). Before he served for nine years as the Chair of the Electrical & Computer Engineering Department at the University of Hartford, he received Ph.D. from Vanderbilt University, M.S. from Ohio University. His research interests include sensor array processing, digital signal processing, power systems in addition to engineering education. He may be reached at alnajjar@hartford.edu.

A CUSTOM VIBRATION TEST FIXTURE USING A SUBWOOFER

Dale H. Litwhiler, Penn State Berks

Abstract

There are many engineering applications for a source of controlled vibrational excitation. Popular applications include fatigue testing of mechanical components and ruggedness and survivability testing of electronic assemblies for harsh environments. Other applications include vibrational energy-harvesting device testing, and accelerometer testing and calibration. There exist several piezoelectric-based energy-harvesting devices that are designed to capture random and/or single-frequency vibrational energy. Testing of these devices requires a source of controllable vibration. The static characteristics of micro electromechanical system (MEMS) accelerometers can often be tested using the earth's gravity or centrifuge apparatus. Testing the dynamic characteristics, however, requires the application of known vibrational acceleration inputs. Single-frequency acceleration inputs are very useful for characterizing the performance of accelerometers. The applied frequency can also be swept to determine the frequency response performance of the device under test. Commercial vibration systems, often called shakers or shaker tables, typically use an electromagnetic voice-coil assembly to move the test fixture. Voice coils can also be found in common audio loudspeakers. The construction of automobile subwoofers is particularly rugged. A very useful vibration test fixture can be created by modifying a subwoofer to include a table area to which a reference accelerometer and the component under test can be mounted. This paper describes the design, construction and application of a subwoofer-based vibration testing system in an undergraduate engineering technology education environment. Some experimental results from the testing of energy-harvesting devices and low-g MEMS accelerometers are also discussed. System component selection, performance and future enhancements are also presented.

Introduction

As part of an investigation into vibrational energy-harvesting devices, the need arose for a controllable source of vibration. Initially, some salvaged automobile sound-

system speakers were evaluated for their performance as transducers for creating the controlled vibrations. From this evaluation, it was determined that with the proper speaker and driving signal, a useful, inexpensive vibration test system could be created. Therefore, a custom vibration system using a car stereo subwoofer as the transducer was designed, built and implemented in an undergraduate engineering technology laboratory.

Figure 1 shows the custom vibration system equipment diagram. Automobile audio subwoofer speakers are robust acoustic transducers with performance capabilities well-suited for low-frequency vibration excitation. An area to which test specimens can be mounted was glued onto the speaker cone. The excitation signal was produced by a laboratory function generator. A unity-gain power amplifier was used to provide the current required to drive the low impedance of the subwoofer. A wideband accelerometer was used as the reference acceleration measurement device. An oscilloscope was used to measure and display the accelerometer output signal.

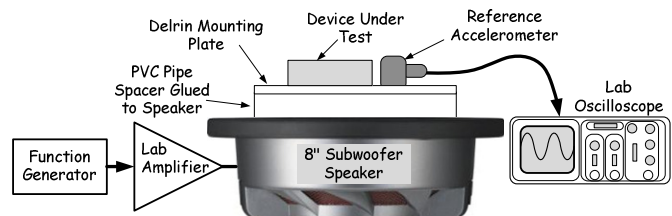


Figure 1. Vibration System Equipment Diagram

System Construction

The shaker table was fabricated using an automobile audio subwoofer speaker as the transducer element. The frequency response range of a subwoofer is appropriate for the desired range of the vibration table. A subwoofer was chosen for its large size and rugged construction. The suitability of the speaker cone area for accepting the intended modifications was also an important consideration. In particular, the Pioneer® model TS-SW841D, 8-inch subwoofer was selected. Some key specifications of this subwoofer are

given in Table 1 [1]. Figure 2 shows the subwoofer before modification.

Table 1. Pioneer Subwoofer Specifications

Music Power, Max	500W
Nominal Power Handling	120W
Frequency Response	30 – 1500 Hz
Nominal Impedance	4Ω
Dimensions	8-7/8" x 3"

The subwoofer was modified to create a flat shaker-table surface. First, a short length (about 1 inch) of 3-inch diameter PVC pipe was bonded directly to the speaker cone material with Goop® adhesive. Goop adhesive bonds well to PVC and the speaker cone material. The PVC spacer helps to raise the test surface above the recessed cone area and also provides separation from the influence of the speaker's very strong magnet.



Figure 2. Pioneer Subwoofer Speaker

A 0.25-inch thick disk of Delrin® acetal resin was used as the shaker-table mounting surface. The disk was fastened to the PVC pipe using eight machine screws arranged in a bolt circle around the edge. The Delrin disk provides an interchangeable and replaceable surface with excellent stiffness and machining properties. The device to be tested was mounted to the shaker table using machine screws as needed.

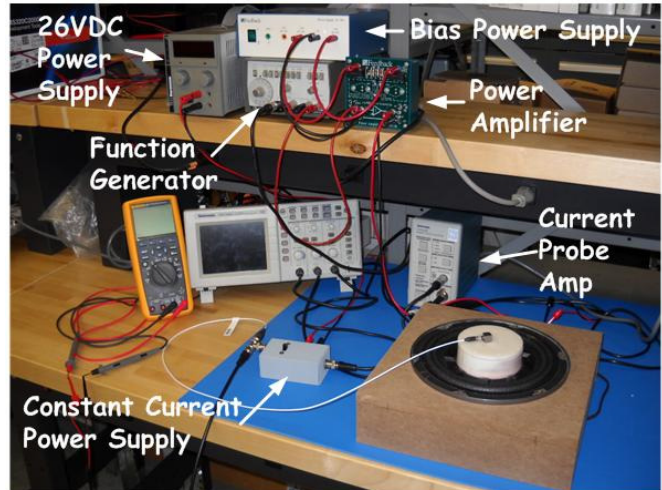


Figure 3. Vibrational Test System

Figure 3 shows a photograph of the completed vibration system. The subwoofer is shown mounted in a custom cabinet constructed of medium-density fiberboard (MDF). Figure 4 shows a close-up photograph of the vibration-table area to reveal the construction details.



Figure 4. Subwoofer Shaker-table Detail

The vibration amplitude of the shaker table was measured by a calibrated reference accelerometer. The PCB Piezotronics model 333B30 accelerometer was chosen for this application due to its low cost, sensitivity and small size and mass. The 333B30 can be seen mounted to the shaker-table surface in Figure 4. Table 2 shows an excerpt from the 333B30 datasheet [2].

Table 2. 333B30 Accelerometer Specifications

<u>PARAMETER</u>	<u>ENGLISH</u>	<u>SI</u>
Sensitivity($\pm 10\%$)	100 mV/g	10.2 mV/(m/s ²)
Measurement Range	± 50 g pk	± 490 m/s ² pk
Freq. Range($\pm 5\%$)	0.5 to 3000 Hz	0.5 to 3000 Hz
Resonant Frequency	≥ 40 kHz	≥ 40 kHz
Excitation Voltage	18 to 30 VDC	18 to 30 VDC
Constant Current Excitation	2 to 20 mA	2 to 20 mA
Output Bias Voltage	7 to 12 VDC	7 to 12 VDC

The accelerometer requires a constant-current power supply with a compliance voltage between 18 and 30VDC. The accelerometer then produces an output DC level of 7 – 12VDC. The dynamic acceleration output signal was superimposed on the DC bias output. The power supply was also custom-designed and built in the engineering technology laboratory. Figure 5 shows the schematic diagram of the constant-current power supply.

As shown in Figure 5, the current-regulator diode, 1N5306, provided the required constant-current bias for the accelerometer. In operation, the DC input voltage was set to 26VDC, while the DC output voltage was monitored with a DVM. The DC output voltage typically settles at about 10.9VDC. When the DC output voltage settles, the accelerometer is ready for use. The 10 μ F capacitor allows only the AC part of the accelerometer output to pass to the oscilloscope input. The user can also access the combined DC and AC output of the accelerometer at the port, which is normally connected to the DVM, as shown.

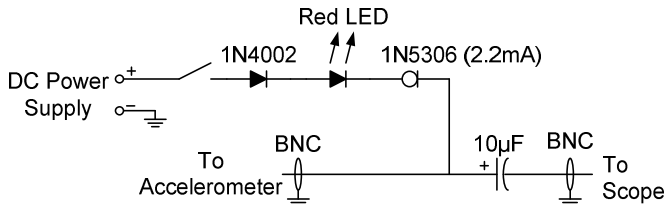


Figure 5. Constant-current Power Supply Schematic

The magnitude and frequency of vibration was controlled by a function generator. The function generator was set to produce a sinewave output with zero offset. A power amplifier was needed to provide the current drive required

by the low impedance of the subwoofer. The vibration system will find application at frequencies below the audio band; therefore, a DC-coupled amplifier was desired. The Feedback® model TK2941B unity-voltage-gain power amplifier was used. The amplifier was part of an educational sensors package already in use in the engineering technology laboratories.

System Performance

To characterize the performance of the subwoofer vibration system, the frequency response of the table acceleration versus speaker input voltage was measured. The input voltage was held nearly constant at about 400mV_{rms} for each frequency tested. Figure 6 shows a plot of the measured frequency response. The data shows a distinctive resonant peak near 45Hz. Therefore, care must be taken when applying signals with frequency components around 45Hz. The frequency response also indicates that the system is useful above of 180Hz.

The input impedance frequency response was also measured. A Tekronix® active current probe was used to measure the subwoofer input current. The speaker input voltage was measured using a standard voltage probe. Again, the input voltage was held nearly constant at 400mV_{rms}. The frequency response of the magnitude ratio of measured speaker input voltage to input current (input impedance) is shown in Figure 7. The input impedance data indicates a distinct, high-Q, electrical resonance near 42Hz.

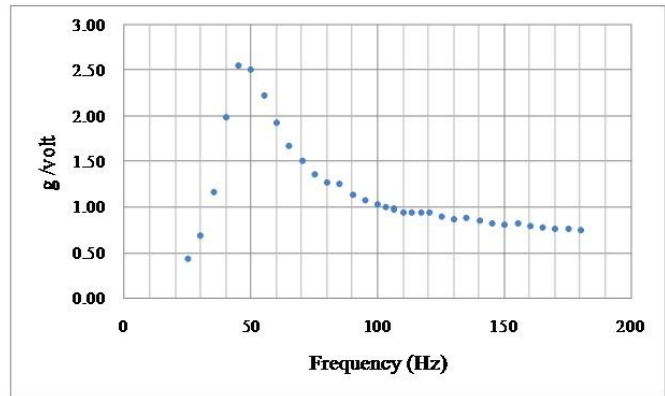


Figure 6. Vibration Table Acceleration Frequency Response

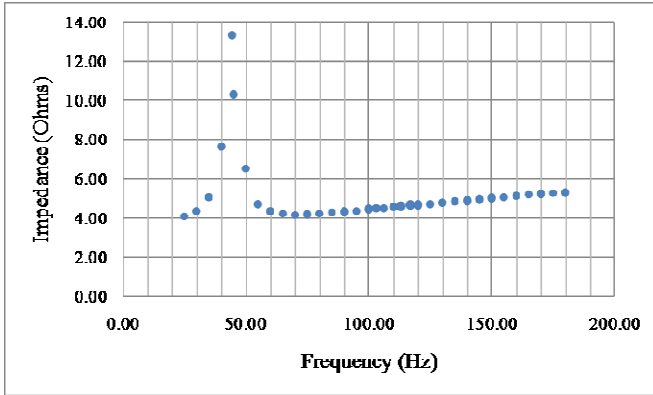


Figure 7. Subwoofer Input Impedance Frequency Response

Example Applications

Energy Harvesting

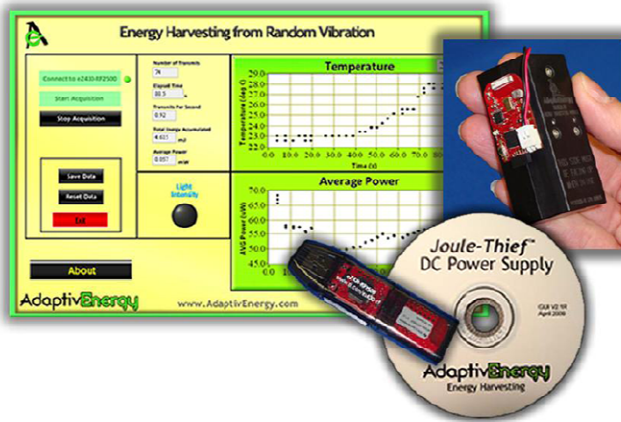


Figure 8. Joule-Thief™ JTRA-e5mini Evaluation Kit

The Joule-Thief™ JTRA-e5mini energy-harvesting module manufactured by AdaptivEnergy is a random vibrational energy-capturing and storage device. It finds application in vehicular vibration-powered sensor systems. The JTRA-e5mini contains a tuned cantilever spring-mass system with an integral piezoelectric generator. To investigate the performance of this device, the evaluation kit was used. As shown in Figure 8, the evaluation kit contains a micro-power wireless communication board, USB communication dongle and application software. The evaluation kit allows the user to remotely monitor and chart the average power output of the JTRA-e5mini [3].

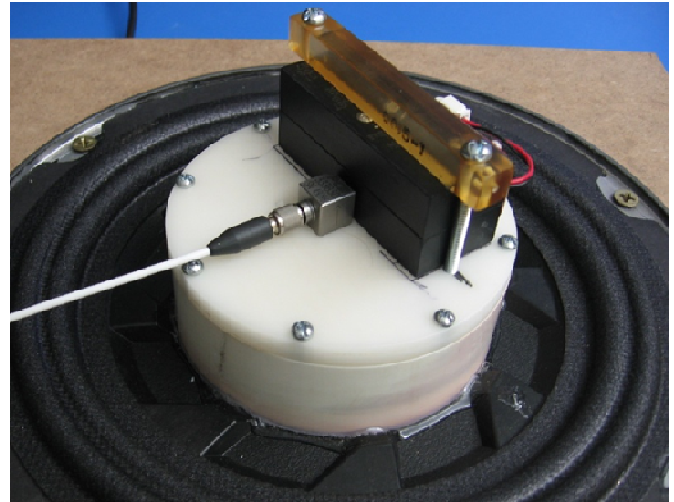


Figure 9. Joule Thief JTRA-e5mini Mounted to Shaker Table.

The Joule Thief JTRA-e5mini energy-harvesting unit was mounted to the subwoofer shaker table using a top-clamping bar arrangement, as shown in Figure 9. The performance of the energy harvester was evaluated for several levels of sinusoidal vibration at about 15Hz. The output of the reference accelerometer was measured using a digital oscilloscope to determine the vibration level. Figure 10 shows a plot of the data obtained from this test.

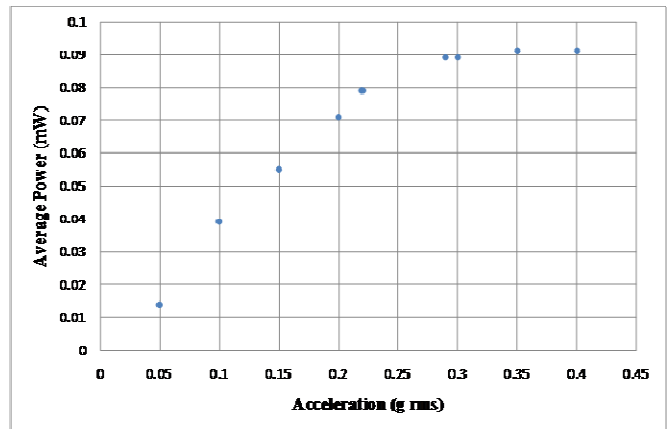


Figure 10. Joule Thief JTRA-e5mini Evaluation Data Plot

MEMS Accelerometers

A custom centrifuge system for the evaluation of the static performance of MEMS low-g accelerometers was presented by Litwhiler [4]. To evaluate the dynamic performance, the accelerometers were mounted to the subwoofer shaker table. The output for each accelerometer was

compared with that of the reference accelerometer. The Freescale MMA2201D ($\pm 40g$) and MMA2260D ($\pm 1.5g$) MEMS accelerometers were tested. Figure 11 shows the test setup for the MEMS devices.

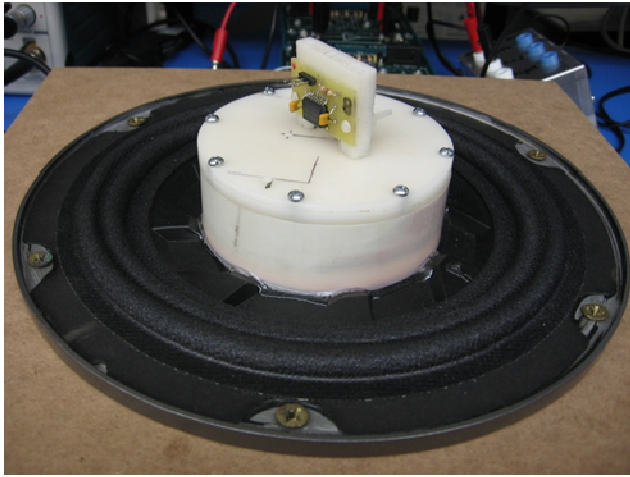


Figure 11. MEMS Accelerometer Test Setup

The MMA2201D has a nominal sensitivity of 50mV per g. The acceleration output signal was superimposed on a zero-g bias voltage of 2.5V when powered from 5V. The frequency response of the MMA2201D versus the reference accelerometer is shown in Figure 12. The MMA2201D was found to have a very flat frequency response with excellent bandwidth.

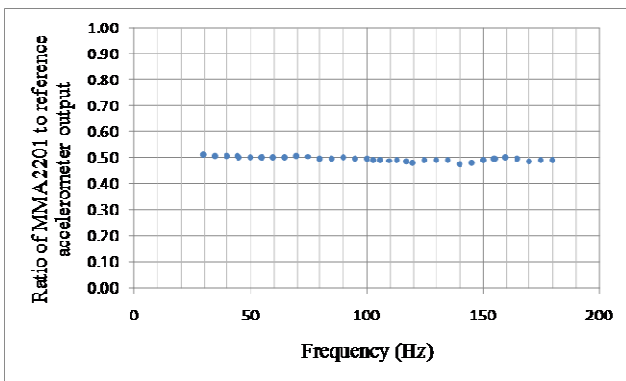


Figure 12. Frequency Response Data for MMA2201D

The MMA2260D has a nominal sensitivity of 1.2V per g. The acceleration output signal was superimposed on a zero-g bias voltage of 2.5V when powered from 5V. The frequency response of the MMA2260D versus the reference accelerometer is shown in Figure 13. The MMA2260D was found to have a bandwidth of about 50Hz which is the nominal value given in the manufacturers datasheet.

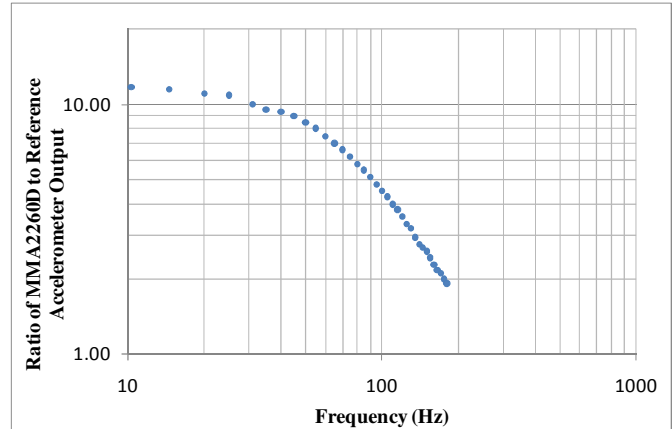


Figure 13. Frequency Response Data for MMA2260D

Future Work

Work continues with making the vibration test system more useable by students with less supervision. This includes developing LabView software to create the subwoofer input signals from a USB sound-card device. This software will allow for the creation of complex waveforms and vibration profiles.

Some nonlinear vibrational behavior was observed at lower frequencies, especially those below 10Hz. Work is continuing to test various methods of correcting the nonlinear behavior to obtain more repeatable acceleration waveforms.

Summary

A vibration test apparatus using a modified subwoofer speaker was designed and fabricated. The modifications were quite simple and inexpensive. The vibration system was characterized and found to have very acceptable performance. The system was used to evaluate the performance of an energy-harvesting device. MEMS accelerometers were also tested using the system with excellent results.

Acknowledgements

The author would like to thank Jordan Waite for his help in developing hardware and software for this project. Jordan is a third-year student in the electromechanical engineering technology program at Penn State Berks.

References

- [1] Pioneer Electronics TS-SW841D subwoofer datasheet available: <http://www.pioneerelectronics.com/PUSA/Products/CarAudioVideo/Subwoofers/Shallow/TS-SW841D?tab=B>
- [2] PCB Piezotronics 333B30 accelerometer datasheet available: http://www.pcb.com/spec_sheet.asp?model=333B30&item_id=9183
- [3] AdaptivEnergy JTRA-e5mini datasheet available: http://www.adaptivenergy.com/docs/WP_AE_01_RandomVibeWSN.pdf
- [4] Litwhiler, D. H., "MEMS Accelerometer Investigation in an Undergraduate Engineering Technology Instrumentation Laboratory," Proceedings of the American Society for Engineering Education Annual Conference and Exposition, 2010.

Biography

DALE LITWHILER is an Associate Professor at Penn State, Berks Campus in Reading, PA. He received his B.S. from Penn State University, his M.S. from Syracuse University, and his Ph.D. from Lehigh University, all in electrical engineering. Prior to beginning his academic career, he worked with IBM Federal Systems and Lockheed Martin Commercial Space Systems as a hardware and software design engineer. Dr. Litwhiler may be reached at dale.litwhiler@psu.edu

BORDER GATEWAY PROTOCOLS

Sadeta Krijestorac, Morehead State University; Marc Beck, University of Louisville; Jonathan Bagby, Florida Atlantic University

Abstract

A Border Gateway Protocol is a path vector routing protocol that coordinates the routing of packets through multiple administrative domains by computing routes between every IP address the packet passes. Certain routers, called BGP speakers, are assigned to run the protocol. BGP speakers across different Autonomous Systems (AS) are interconnected in order to exchange routing information. BGP supports a feature called multihoming, which means connecting to multiple ISPs from different routers or points in the network. However, BGP still have several serious security vulnerabilities, which are currently being addressed. We discuss Pros and Cons of BGP and possible security enhancements.

Introduction

The Border Gateway Protocol (BGP) can be seen as the core interdomain routing protocol of the Internet. It is an inter-autonomous system routing protocol designed for TCP/IP networks which maintains a table of IP network prefixes that designate network reachability among autonomous systems. BGP is a path vector protocol which makes routing decisions based on paths and network policies instead of using conventional Interior Gateway Protocol (IGP) metrics. The main role of a BGP system is to exchange network reachability information with other BGP systems. In this paper we provide an overview of how BGP works, its purpose, and how it interacts with other components of the Internet as well as advantages and disadvantages of BGP alternative protocols.

Overview of Operation

The Internet is a very large-scale decentralized network, consisting of smaller networks. When a packet is sent across the Internet it may pass through multiple networking administrative domains, so-called Autonomous Systems (AS). The interdomain routing of all AS's on the Internet is coordinated by the Border Gateway Protocol (BGP) running on routers that connects the AS's. The task of BGP is to compute routes between every AS and every IP address that a packet is passing on its way from one computer to another [1]. BGP is the interdomain routing protocol used to exchange reachability information between AS's on the Internet. To choose best routes, BGP allows each AS to override distance based metrics with policy based metrics [1].

Model and Terminology

Figure shows the Chart of BGP Between AS's. The Internet Engineering Task Force (IETF) created BGP as RFC 1771 and service providers first introduced it in the early 1990s as a scalable, standardized scheme to route traffic between the AS's of their customers and other service providers [2]. In order to create a BGP network, certain routers need to be assigned to run the protocol. Because they speak the BGP "language", these routers are referred to as BGP speakers. To actually create the BGP internetwork, the BGP speakers bordering each AS are physically connected to one or more BGP speakers in other AS's, ignoring any topological differences. The direct connection between them permits them to exchange information about AS's to which they belong. BGP speakers are most often connected to multiple other speakers, which provide more direct paths to different networks for better efficiency. This also offers redundancy, allowing the Internet to deal with either device or connection failure. It is likely for a BGP speaker to have neighbor relationship with other BGO speakers both within and outside its own AS [2].

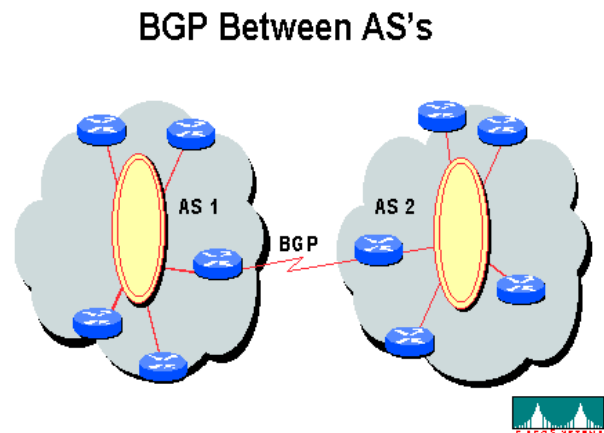


Figure 1. Initial Research Configuration with Commercial Devices

Initialization of Routes

In network-layer reachability information (NLRI) aggregation, routing data to a given network in a given AS is passed along by BGP speakers in a chain domain. Each

BGP speaker in the chain appends information about its own identity and the preceding AS in the chain. As the AS routing data passes through the Internet, augmented by the list of AS's that have been passed so far, BGP forms an AS path to prevent routing loops. Once the desired topology has been defined, network administrator can determine the optimal paths and begin to set policies establishing which network destinations and communities of network destinations can exchange information [3].

Properties of the Protocol

BGP is a path vector routing protocol. Each route description has several components, such as the list of prefixes being withdrawn or added, the AS path to be followed in reaching the prefix, and the address of the next router along the path [4]. The initial data-flow across a BGP backbone fills the complete BGP routing table and it gets updated incrementally when the routing tables of the other routers change. A BGP speaker must retain the current version of all of its peers' BGP routing table and only updates changes instead. Routers periodically send keepalive messages to verify that connections are still working. BGP nodes communicate via the Transmission Control Protocol (TCP). BGP guarantees that networks within an external AS are reachable before exchanging any information by using a combination of internal BGP peering among the AS's routers and by redistributing BGP routing information to its interior gateway protocols [4].

Performance Evaluation

For cost or performance reasons, it is often necessary for AS's to control the flow of their interdomain traffic. The technique of AS-Path prepending is actually useful to point out that a backup link should best be avoided if possible, but it is not easy to use it for balancing incoming traffic. AS-Path prepending is used for multihoming, which means connecting to multiple ISPs from different routers or points in the network. Quoitin, Pelsser, Bonaventure, and Uhlig have used large-scale simulations to evaluate the BGP decision process and AS-Path prepending in the Internet [5]. They found out in their simulation that the tie-break rules of the BGP decision process account for the selection of 30-50% of the routes in the global Internet. In order to control the flow of incoming packets accurately, an AS needs to be able to predict which route a distant AS will select. This prediction is very difficult to make, because the AS's knowledge of the entire Internet topology and the routing policies if often insufficient. Even if the complete topology was known, predicting the outcome of the tiebreak rules of the BGP decision process would still be very complicated.

Based on this analysis, the current BGP-based technique seems not to be appropriate to control the incoming packet flow. It is suggested that changes to the Internet architecture might be necessary to achieve this kind of control [5].

Performance Measure

Packet delivery is the most important performance measure for routing protocols, since this is the primary purpose of routing. The hop count can also be used as performance measure for BGP to determine the end-to-end path.

The path with the fewest links between a source and a destination will be chose. An ideal routing protocol should adapt rapidly to any change in topology and deliver packets as long as any path to the destination is available. Zhang et al. examined the packet delivery performance in a network running the BGP proposals when a destination may be disconnected from time to time [6]. Existing BGP proposals to improve convergence could negatively impact delivery during transient failure [6]. Most currently available routing protocols usually take seconds, or even up to several minutes, for converging after a failure. In that time, some packets may already be on their way to their destinations and new packets might have been sent. These packets can encounter routing loops, delays, and losses. There is currently not much information available about how many of them actually arrive at their destination and how many get lost during routing convergence periods [7].

Pros

One of the greatest advantages of BGP is that corporate users can set up flexible connections between their corporate network and multiple Internet Service Providers (ISPs). For, example, enterprise users can multihome and they can also set up BGP routers to automatically reroute traffic among two or more ISPs for load-sharing or backup purposes. Two major features distinguish BGP from other routing protocols:

- It uses aggregation as a way of disseminating NLRI across routers.
- It uses path attributes for implementing routing policies [8].

Cons

BGP has been found to be vulnerable to attacks and miss configurations [9]. The cause of this problem is that BGP depends on information to update routing tables that is difficult to verify. Corrupted routers can add false information to the messages they transmit which other routers then use and further propagate when uncorrupted routers send extensions

of these forged messages. It is easy to image how many serious problems a successful compromise of a router can cause throughout the Internet [9].

Optimal Applications (Topology, Architecture, Layer 1 Medium)

BGP is able to connect any internetwork of AS's no matter what topology these systems use. It can handle any possible topology (full mesh, partial mesh, chain, etc.) as well as change to the topology that may occur over time when systems connect or disconnect. The only requirement is that at least one router in each AS is able to run BGP and that this router is connected to at least one other AS's BGP router. BGP is completely unaware about what happens within the AS because it is autonomous. This means each AS has its own internal topology and set of routing protocols that it uses to make its own decision to determine routes. BGP takes only data that it receives from an AS and shares it with other AS's.

Conclusion

BGP has been an integral part of the Internet architecture for almost two decades now. It has evolved since then in order to adapt to changes in technology, performance requirements, and security concerns. A great amount of effort has been undertaken to add new features to the original specifications. That show that even new additions can be made and existing problems can be solved. Despite proposals for findings a replacement it seems that BGP will most likely evolve further in years to come in order to meet the demands of it users.

References

- [1] S. Agrawal, C.C.Chuan, S. Bhattacharyya, C. Diot, "The Impact of BGP Dynamics on Intra-Domain Traffic," ACM SIGMETRICS Performance Evaluation Review Vol.32, Issue 1, June 2004, <http://reserch.microsoft.com/~sagrawal/sigmetrics04.pdf>.
- [2] T.G. Griffin, G. Wilfong, "An Analysis of BGP Convergence Properties," Computer Communication Review, a publication of a ACM SIGCOMM, Vol. 29, No. 4 October 1999, pp 277-288.
- [3] M. Zhao, S. W. Smith, D.M. Nicol, "Aggregated Path Authentication for Efficient BGP Security," Dartmouth Computer Science Technical Report, TR2005-541, May 2005 <http://www.ists.dartmouth.edu/library/175.pdf>
- [4] J.Kim, S. Y.Ko, D.M. Nicol, X. A. Dimitropoulos, G.F.Riley, "A BGP Attack against Traffic Engineering," Simulation Conference, 2004. Proceedings of the 2004 Winter, V1, Issue 5, December 2004, pp 318-326.
- [5] B. Quoitin, C. Pelsser, O. Bonaventure, S. Uhlig, "A performance evaluation of BGP-based traffic engineering," Intl. Journal of Network Management, Vol. 15, Issue 3, May 2005, pp. 177-191.
- [6] B. Zhang, V. Kambhampati, M. Lad, D. Massey, L. Zhang, " Identifying BGP Routing Table Transfers," Conference Proceedings of the 2nd ACM SIGCOMM Workshop on Internet Measurement, 2002, pp243, www.cs.arizona.edu/~bzhang/paper/05-minenet-mct.pdf
- [7] A. Khan, "Border Patrol-BGP," Packet Magazine Arhives, 1998, <http://www.cisco.com/warp/public/784/packet/oct98/6.html>
- [8] C.M. Kozierok 2005 TCP/IP guide, No Starch Press
- [9] D. Pei, L. Wang, D. Massey, S. F. Wu, L. Zhang, "A study of packet delivery performance during routing convergence," Dependable Systems and Networks, 2003. Proceedings of IEEE International Conference on Dependable Systems and Networks, 22-25, June 2003, pp 183-192.

Biographies

SADETA KRIJESTORAC is an assistant professor in Applied Engineering and Technology Department at Morehead State University in Morehead, KY. She instructs graduate and undergraduate computer engineering and networking courses, directs graduate research, and performs research involving Wireless Communications, Data Networking and Microprocessor Based Design courses. Specific projects involve digital communications, signal processing, and intelligent instrumentation. Dr. Krijestorac may be reached at s.krijestor@moreheadstate.edu

MARC BECK is a PhD student in the Computer Science and Computer Engineering department at J.B. Speed School of Engineering at the University of Louisville in Louisville, KY. He received a B.S. in Computer Science from Brescia University in Owensboro, KY, and a M.S. in Industrial Technology from Morehead State University in Morehead, KY. His interests include signal processing and robotics. Mr. Beck can be reached at mbbeck05@louisville.edu.

JONATHAN BAGBY, P.E., is an Associate Professor in Electrical Engineering at the Florida Atlantic University, Boca Raton, FL. His interests include electromagnetic computation, microwave design, fiber optic communications and computer networking. Professor Bagby may be reached at bagby@fau.edu

A MULTIPLE-ACCESS PROTOCOL FOR MULTIMEDIA TRANSMISSION OVER WIRELESS ATM NETWORKS

Hong Yu, Capitol College; Mohammed Arozullah, The Catholic University of America

Abstract

In this study, the authors developed and evaluated the performance of an advanced multiple-access protocol for transmission of a full complement of multimedia signals consisting of various combinations of voice, video, data, text and images over wireless networks. The protocol is called Advanced Multiple-Access Protocol for Multimedia Transmission (AMAPMT) and is to be used in the Data Link Layer of the protocol stack. The protocol grants permission to transmit to a source on the basis of a priority scheme that takes into account a time-to-live (TTL) parameter of all transactions, selectable priorities assigned to all sources and relevant channel state information (CSI), in that order. Performance of the protocol is evaluated in terms of quality-of-service (QoS) parameters like cell-loss ratio (CLR), mean cell-transfer delay (MCTD) and Throughput. Models can be simulated based on OPNET simulation software under various traffic loads with constant distributions, various mean arrival rates and transaction sizes. Results indicate whether performance is improved or not when this priority scheme is used.

Introduction

Wireless Networks can be used to transmit multimedia services consisting of voice, data, video, ftp, and text. These networks are required to provide desired qualities of service (QoS) to the various media with diverse flow characteristics [1]. For example, cell-loss ratio requirements for all loss-sensitive services such as email and cell-delay requirements for all delay-sensitive services such as voice are to be satisfied simultaneously and adequately. For a given input traffic load, a certain amount of resources (e.g., buffer space and link capacity) are needed to satisfy these QoS requirements. Thus, it is necessary to develop simple and efficient resource-management protocols for these networks that can provide better use of network resources. In this paper, such a protocol for multimedia transmission called Advanced Multiple-Access Protocol for

Multimedia Transmission Protocol (AMAPMT) is presented. Performance of this protocol is evaluated in terms cell-loss ratio (CLR), mean cell-transmission delay (MCTD) and throughput under various traffic loads with constant but

varying mean arrival rates and transaction sizes. The protocol uses parameters like time to live (TTL) of transactions, priority of individual media and relevant channel-state information (CSI) in order to grant permission to the sources to transmit. Performance is evaluated by implementing a simulation test bed using OPNET simulation software. In this test bed, a wireless network consisting of a selectable number of source stations, mobiles and a base station has been implemented. The performance of the AMAPMT protocol is evaluated by using this test bed. Results for CLR, MCTD and throughput are obtained and presented in tabular and graphical forms for various combinations of the aforementioned parameters. Also, performance of this protocol was compared to that of a currently-available multiple-access protocol called Adaptive Request Channel Multiple-Access (ARCMA) and AMAPMT protocol was shown to out-perform the ARCMA protocol [2].

Service Types of Multimedia Signals

A multimedia signal may consist of some or all of the five service categories: constant bit rate (CBR), real-time variable bit rate (RT-VBR), non-real-time variable bit rate (NRT-VBR), available bit rate (ABR) and unspecified bit rate (UBR) [3]. Constant bit rate (CBR) services generate output at a constant bit rate and require time synchronization between the traffic source and destination as well as predictable response time and a static amount of bandwidth for the lifetime of a connection with low latency. Real-Time Variable Bit Rate (RT-VBR) services compressed video stream or mobile Internet access application generate information at a rate that is variable with time, requires time synchronization between the traffic source and destination and that the delay be less than a specified maximum value and a variable amount of bandwidth. Non-Real-Time Variable Bit Rate (NRT-VBR) services that include file transfer and image applications generate variable bit-rate traffic for which there is no inherent requirement on time synchronization between the traffic source and destination and require no guaranteed delay bound. Available Bit Rate (ABR) is a best-effort service, where neither data rate nor delay is guaranteed. The minimum and maximum rates are guaranteed, as is a bound on cell loss rate. This service includes data and allows wireless systems to fill their channels to maximum capacity when CBR or VBR traffic is low. Unspecified Bit Rate (UBR) services are similar to NRT-VBR but

without a guaranteed minimum rate or bound on the cell loss rate. It is used for connections that transport variable bit-rate traffic for which there is no requirement on time synchronization between the traffic source and destination, file transfer, back-up transfer and email without delay guarantee.

Wireless Networks

Introduction

A typical Wireless network consists of a base station, a number of mobiles and source stations. Each mobile is connected to a number of source stations. The source stations may be of different types such as voice stations, data stations, ftp stations and email stations. In this network, the source stations generate and save information (voice, video, data, ftp, email). The source stations send Request Access (RA) packets to the relevant mobiles to ask permission to send information. The mobiles forward these requests to the base station. The base station considers all such requests for a time frame and grants permission to transmit information, according to some multiple-access protocol, to the source stations via relevant mobiles. Performance of the protocol is measured in terms of some desired qualities of service.

Available Multiple-Access Protocols: Their Applicability and Shortcomings

Three multiple-access protocols are available. These are Packet Reservation Multiple-Access (PRMA) [4], Distributed Queuing Request Update Multiple-Access (DQRUMA) [5] and Adaptive Request Channel Multiple-Access (ARCMA). The currently available multiple-access protocols deal with voice and data and not a full complement of multimedia signals. Further, these protocols do not assign explicit priority to the different types of information, namely, voice and data. There is a need for multiple-access protocol for handling a full complement (CBR, RT-VBR, NRT-VBR, ABR and UBR) of multimedia signals. Some of the media may be delay-sensitive while others are loss-sensitive. However, the problem with priority assignment according to the type of the media type only is that some lower priority media may have to wait too long and the information may become stale. Also, the stations have limited buffer space, so some of the information may be lost due to buffer overflow and discarding traffic coming through channels with inferior transmission quality can improve processing and transmission times for other traffic coming through channels with superior transmission qualities. Thus, consideration of explicit priorities, Time to Live (TTL) of transac-

tions, and Channel State Information (CSI) parameters may improve the situation [6]. A protocol that assigns priorities on the basis of TTL, explicit priorities for the various media and CSI is proposed and evaluated in the next section.

The Advanced Multiple-Access Protocol For Multimedia Transmission (AMAPMA)

Introduction

In this study, a new multiple-access protocol for wireless network called Advanced Multiple-Access Protocol for Multimedia Transmission (AMAPMT) was developed and its performance evaluated. This protocol handles the full complement of multimedia signals and uses the time-to-live (TTL) parameter and explicit priority assignments to media types to improve its performance and to treat the various types of media fairly. It also uses channel state information (CSI) (e.g., bit error rate) in assigning access to media. Media received over a channel with unacceptably low channel state information (e.g., high BER) are denied access.

The Principle of Operation of the AMAPMT Protocol

In this protocol, the stations generate and save information (voice, video, data, ftp, email). The stations send Request Access (RA) packets to the relevant mobiles to ask permission to send information. The mobiles forward these RA packets to the base station over a reservation channel using a multiple-access protocol like slotted ALOHA and TDMA [7]. The base station acknowledges the requests and saves the RA packets for a period of time. The Request Access (RA) packets contain information on the source address, media type, bit rate, time to live, CSI and the requested quality of service (QoS) of the traffic to be transmitted. The base station processes the RA packets and grants permission to the relevant stations to transmit on a fair-queuing basis using the parameters contained in the RA packets in the order of TTL, CSI and traffic type.

The Flow Charts of Operation of the AMAPMT Protocol

The flow charts in Figures 1 - 5 describe the various aspects of operation of the AMAPMT multiple-access protocol. For the flow chart in Figure 1, the protocol for handling RA packets at the base station presents the way the base station handles the arriving Request Access (RA) packets from all

mobiles. All arriving RAs are saved at the buffer. The RAs are selected in ascending order of TTLs. The RAs with the lowest TTL are selected first. If there is only one RA with the lowest TTL then the mobile that generated this RA is given permission to transmit if the corresponding channel CSI is acceptable. Otherwise, this RA is rejected and RAs with the next TTL are selected. If there are multiple RAs with the same TTL, then the TTLs with unacceptable CSIs are discarded and the remaining RAs are sorted into individual queues of RAs from CBR, VBR, ABR and UBR sources. These queues are serviced in this order, one by one, according to the Serve Queue Function in Figure 2.

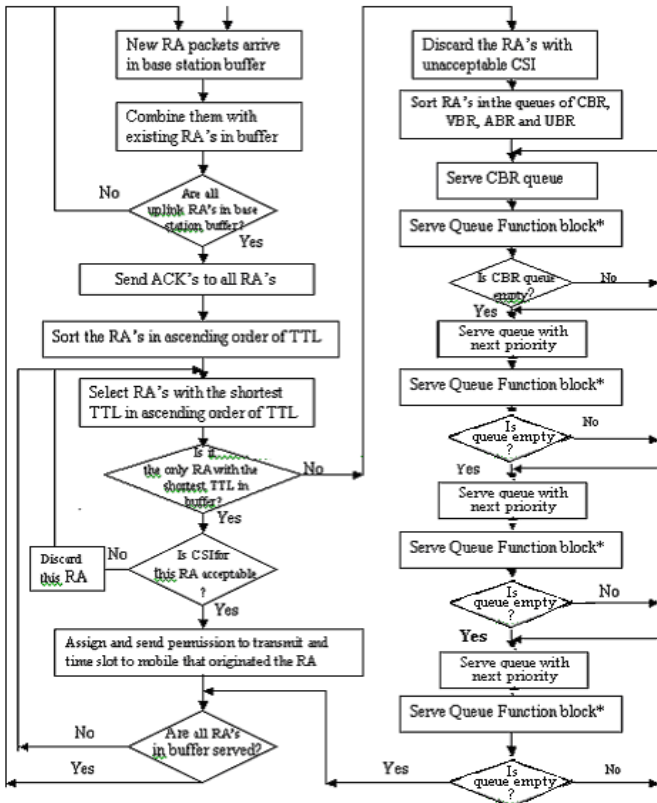


Figure 1. Protocols for the Handling of RA Packets at the Base Station

For the flow chart in Figure 2, the Serve Queue Function block at the base station presents the way the base station assigns time slots and Permission to transmit to the CBR, VBR, UBR and VBR mobiles according to FIFO queuing strategy. At the same time, the signal information with the lowest priority will be discarded by the base station of the network. The signal with the highest priority will receive the acknowledgment response to upload the information data.

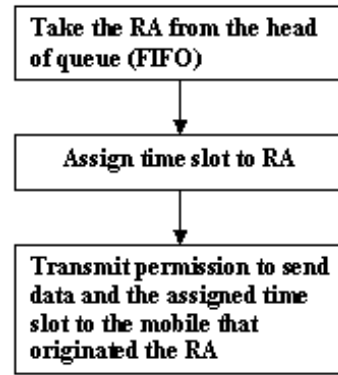


Figure 2. Serve Queue Function Block at the Base Station

The flow chart in Figure 3 shows the protocol for the handling of data packets at the base station presents the way the base station and assigns time slots and permission to transmit to the CBR, VBR, UBR and VBR mobiles. After a mobile is given permission to transmit, it transmits to the base station data packets requesting permission for transmission for further packets. If this is the first request for permission to transmit, then it sets the piggyback bit in the requesting data packet to 0; if it is a repeat request for permission to transmit, then it sets the piggyback bit in the requesting data packet to 1. The base station uses this piggyback bit to give preference to mobiles requesting permission to transmit for the first time, according to this protocol.

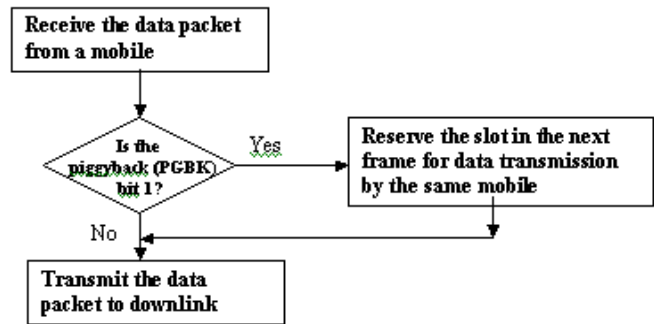


Figure 3. Protocol for the Handling of Data Packets at the Base Station

For the flow chart in Figure 4, the Protocol at the Mobiles for Handling RA Packets from Stations presents the way the mobiles assigns time slots and Permission to transmit to the CBR, VBR, UBR and VBR mobiles. RA packets arriving at the mobiles are queued in CBR, VBR, ABR and UBR queues and are served in this order according this protocol using the Data Packet Process Function at the Mobiles, as shown in Figure 5.

Simulation and Performance Evaluation of the AMAPMT Protocol

Introduction of the Network Simulation Model and Architecture

The wireless ATM network that is simulated consists of a base station, five mobiles, and four stations per mobile. The five traffic types—namely voice, video, data, ftp and email—are simulated in OPNET by using CBR for the voice, RT-VBR for video, NRT-VBR for ftp, ABR for data traffic and UBR for email. The performance of the protocol is evaluated under various combinations of operational conditions of relative priorities of various media, time-to-live (TTL) and channel state information (CSI) parameters. In each case, three performance metrics, namely, Cell Loss Ratio (CLR) and Mean Cell Transmission Delay (MCTD), are obtained and compared.

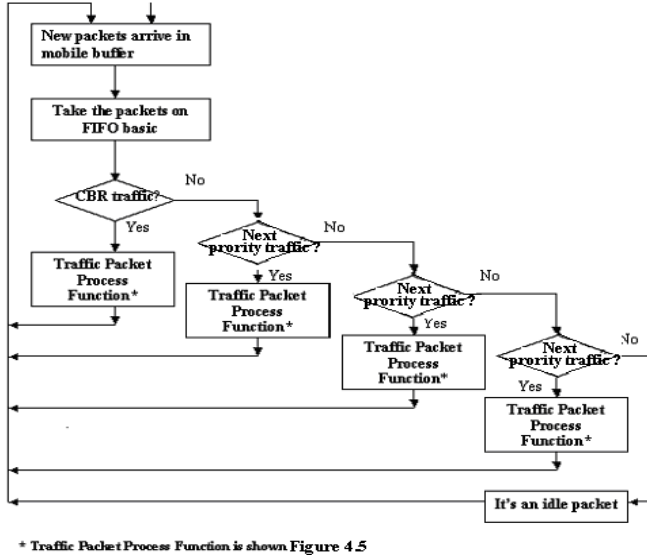


Figure 4. Protocol at the Mobiles for the Handling of RA Packets from the Stations

PGBK = Piggyback
 TA = Transmission Access
 ACK = Acknowledgement

For the flow chart in Figure 5, the Data Packet Process Function at the Mobiles presents the way the mobiles select and transmit the requests for service from stations.

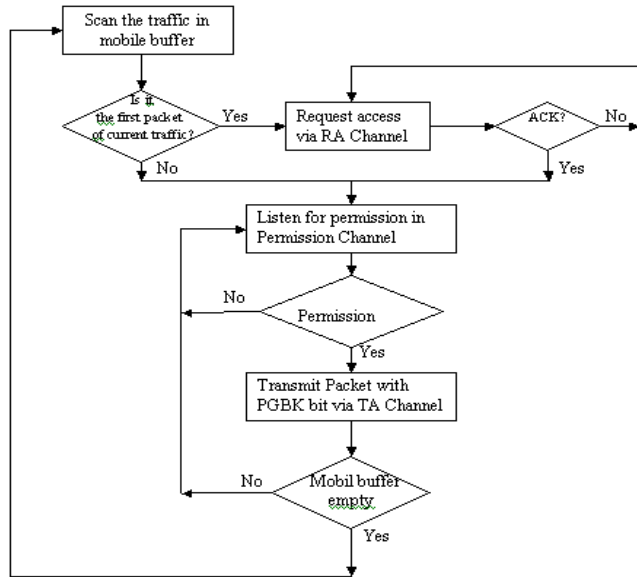


Figure 5. Data Packet Process Function at the Mobiles

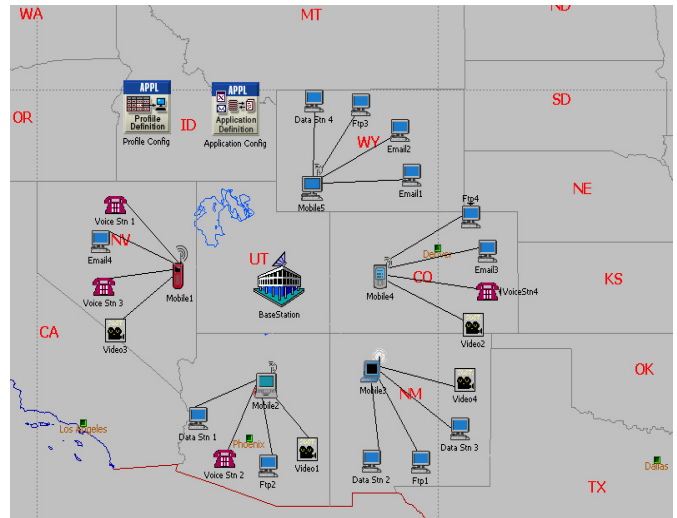


Figure 6. Simulation Model of a Wireless Network

The network model, shown in Figure 6, consists of a base station, five mobiles and four source stations per mobile. The source stations are of different types. In this network, the source stations generate and save information (voice, video, data, ftp, email). The stations send Request Access (RA) packets to the relevant mobiles to ask permission to send information. The mobiles forward these requests to the base station. The base station considers all such requests for a period of time and grants permission to the stations to transmit information according to the AMAPMT multiple-access protocol. A number of simulations are run and results are collected to evaluate the performance of the protocol in terms of Cell Loss Ratio (CLR) and Mean Cell Transmission Delay (MCTD).

Simulation Results for Performance Evaluation of the AMAPMT Protocol

Simulation results in terms of cell loss ratio (CLR), mean cell transfer delay (MCTD) and throughput are obtained and presented for the following combinations of different relative priorities of the various media, different TTL values of transactions and channel state information (CSI) for constant source generation rates.

- The sources have the same priority, same TTL and same CSI (BER=1E-06)
- The sources have different priorities, but the same TTL and same CSI (BER=1E-06)
- The sources have the same priority but different TTLs and the same CSI (BER=1E-06)
- The sources have different priorities, different TTLs and the same CSI (BER=1E-06)

The sources generate cells at a constant distribution rate with mean rates of up to 250,000 cells per second. The buffer size at the source stations is set to 512Kbytes. The buffer size at the mobile stations and the base station are assumed to be unlimited. The channel state information (CSI) is taken as bit error ratios (BER) of 1E-06 or 1E-12 with 1.54Mbps transmission rates [8]. The utilization factor, $\rho = .259$, obtained as the ratio of the average generation rate of 50Kbytes per second and the service rate of 1.54Mbps, is used in all cases. See Tables 1 - 4 for the various actual values of TTL, priorities and CSI used in the simulation.

Table 1. Parameter Values for Same TTL, Same Priorities and Same CSI

Station #		1	2	3	4	All Stations	All Stations
		TTL	TTL	TTL	TTL	PRIORITY	CSI (BER)
CBR	VOICE	10	10	10	10	Low Latency	10^{-6}
RT-VBR	VIDEO	10	10	10	10	16	10^{-6}
NRT-VBR	FTP	10	10	10	10	16	10^{-6}
ABR	DATA	10	10	10	10	16	10^{-6}
UBR	EMAIL	10	10	10	10	16	10^{-6}

Table 2. Parameter Values for Different Priorities, Same TTL and Same CSI

Station #		1	2	3	4	All Stations	All Stations
		TTL	TTL	TTL	TTL	PRIORITY	CSI (BER)
CBR	VOICE	10	10	10	10	Low Latency	10^{-6}
RT-VBR	VIDEO	10	10	10	10	16	10^{-6}
NRT-VBR	FTP	10	10	10	10	8	10^{-6}
ABR	DATA	10	10	10	10	4	10^{-6}
UBR	EMAIL	10	10	10	10	2	10^{-6}

Table 3. Parameter Values for Different TTL, Same Priorities and Same CSI

Station #		1	2	3	4	All Stations	All Stations
		TTL	TTL	TTL	TTL	PRIORITY	CSI (BER)
CBR	VOICE	10	35	60	85	Low Latency	10^{-6}
RT-VBR	VIDEO	15	40	65	90	16	10^{-6}
NRT-VBR	FTP	20	45	70	95	16	10^{-6}
ABR	DATA	25	50	75	100	16	10^{-6}
UBR	EMAIL	30	55	80	105	16	10^{-6}

Table 4. Parameter Values for Different TTL, Different Priorities and Same CSI

Station #		1	2	3	4	All Stations	All Stations
		TTL	TTL	TTL	TTL	PRIORITY	CSI (BER)
CBR	VOICE	10	35	60	85	Low Latency	10^{-6}
RT-VBR	VIDEO	15	40	65	90	16	10^{-6}
NRT-VBR	FTP	20	45	70	95	8	10^{-6}
ABR	DATA	25	50	75	100	4	10^{-6}
UBR	EMAIL	30	55	80	105	2	10^{-6}

The results, in terms of CLR, MCTD and Throughput for a Utilization factor of $\rho = .259$, a constant-source rate distribution generation, and BER=1E-06 are shown in Figures 7 - 9.

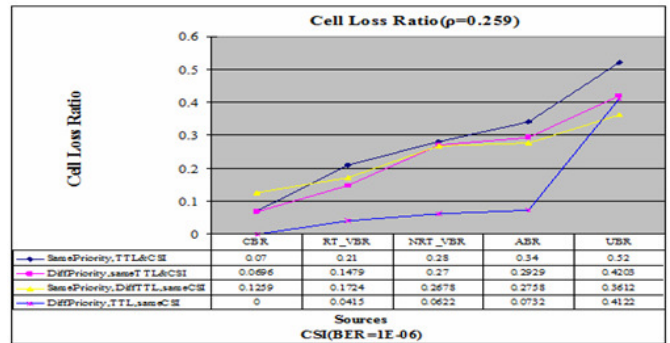


Figure 7. Comparison of CLR for a Number of Combinations of Priority, TTL and CSI

It can be seen from Figure 7 that the CLR is the highest for all media except CBR, when priorities are considered in granting permission to transmit. The CLR is slightly reduced in these cases. Finally, the CLR values are substantially reduced for all the media when priorities and TTLs are simultaneously considered, as proposed in the AMAPMT protocol. Thus, the AMAPMT protocol can be used to substantially improve the CLR performance for the various components of multimedia signals.

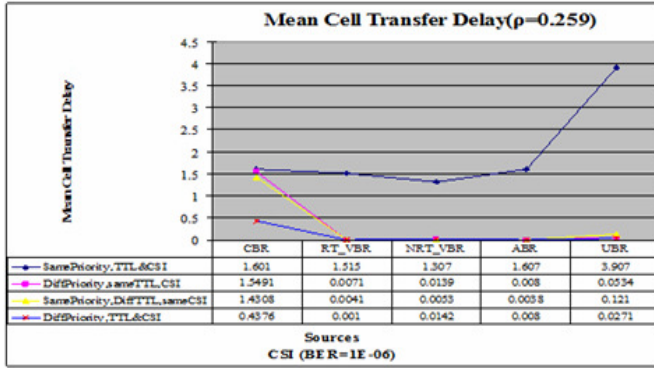


Figure 8. Comparison of MCTD for a Number of Combinations of Priority, TTL and CSI

It can be seen from Figure 8 that the MCTD is considerably reduced in cases where only priorities, but not TTLs, and when only TTLs and not priorities, and both priorities and TTLs are considered as proposed in the AMAPMT protocol. Thus, the AMAPMT protocol can be used to substantially improve the MCTD performance for the various components of multimedia signals.

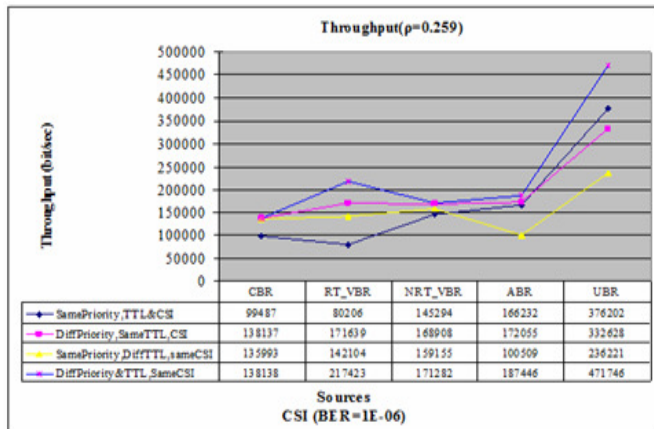


Figure 9. Comparison of Throughput for a Number of Combinations of Priority, TTL and CSI

It can be seen from Figure 9 that Throughput is the highest for all media when priorities and TTLs are simultaneously considered in assigning permission to transmit, as proposed in the AMAPMT protocol. Thus, the AMAPMT protocol can be used to improve Throughput performance for the various components of multimedia signals.

The results, in terms of CLR, MCTD and Throughput for a utilization factor of $\rho = .259$, a constant-source rate distribution generation, and BER = 1E-12 are shown in Figures 10 - 12.

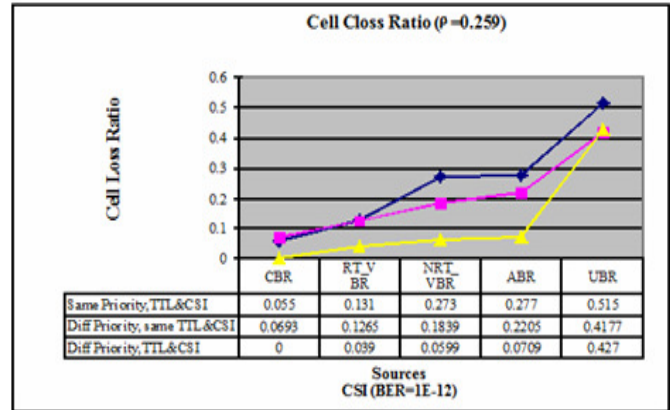


Figure 10. Comparison of Throughput for a Number of Combinations of Priority, TTL and CSI

It can be seen from Figure 10 that the CLR is slightly reduced in cases where only priorities, but not TTLs, are considered as proposed in the AMAPMT protocol, and the CLR values are substantially reduced for all the media when priorities and TTLs are simultaneously considered, as proposed in the AMAPMT protocol.

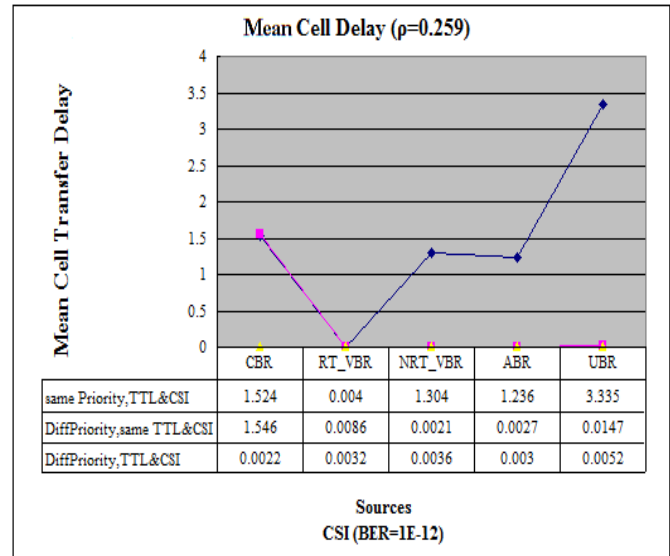


Figure 11. Comparison of MCTD for a Number of Combinations of Priority, TTL and CSI

It can be seen from Figure 11 that the MCTD is reduced in cases where only priorities, but not TTLs, are considered as proposed in the AMAPMT protocol. Finally, the CLR values are substantially reduced for all the media when priorities and TTLs are simultaneously considered, as proposed in the AMAPMT protocol. Thus, the AMAPMT protocol can be used to substantially improve the CLR performance for the various components of multimedia signals.

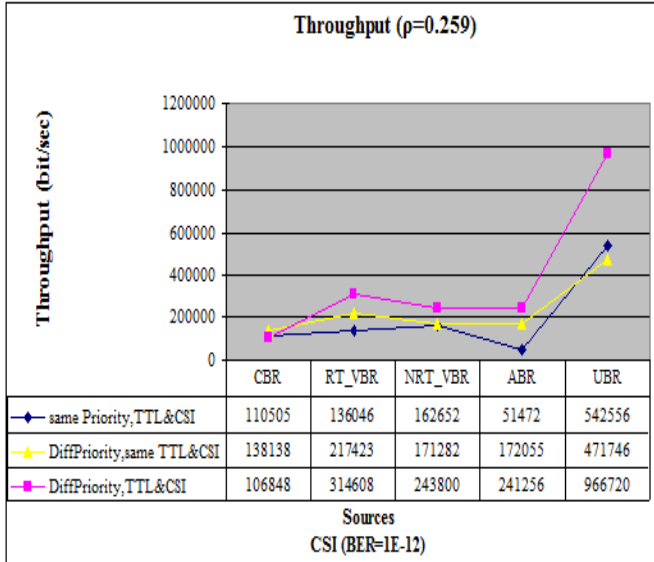


Figure 12. Comparison of Throughput for a Number of Combinations of priority, TTL and CSI

It can be seen from Figure 12 that Throughput is the highest for all media when priorities and TTLs are simultaneously considered in assigning permission to transmit, as proposed in the AMAPMT protocol. Thus, the AMAPMT protocol can be used to improve Throughput performance for the various components of multimedia signals.

Performance of ARCMA and AMAPMT protocols is evaluated and compared under the following set of parameter values, where LL stands for Low Latency.

Table 5. Parameter Values for ARCMA and AMAPMT Protocol Performance

Type	TTL	Priority of Signal types		CSI	Transaction size		Transmission rate
		Types	weight		Distribution	Mean	
ARCMA Protocol	same	CBR	16	same (BER=1E-06)	constant	500KB	DS1 (1.544Mbps)
		RT_VBR	1				
		NRT_VBR	1				
		ABR	1				
		UBR	1				
AMAPMT Protocol	different	CBR	LL	same (BER=1E-06)	constant	500KB	DS1 (1.544Mbps)
		RT_VBR	16				
		NRT_VBR	8				
		ABR	4				
		UBR	2				

The TTL and priority values used in Table 5 correspond to Figures 13 - 15. The ARCMA protocol CBR is assigned the highest priority and other media are assigned the same low priorities and the same TTL values. Sources with constant rate distribution generation are used. The results are shown in Figures 13 - 15.

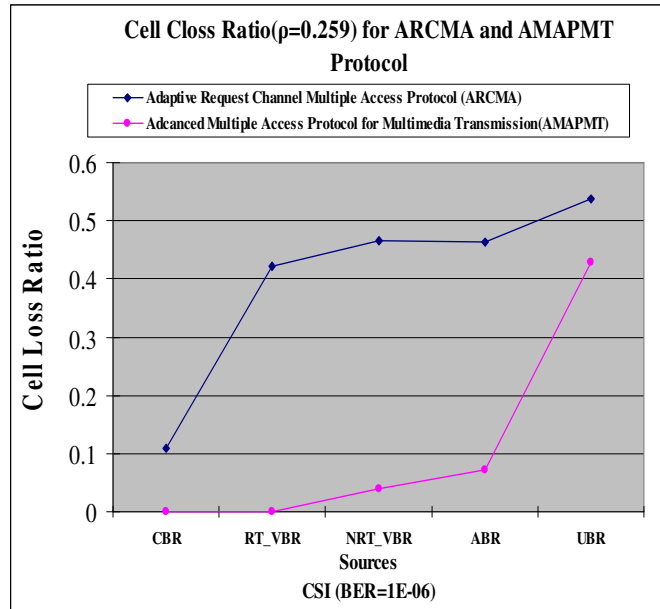


Figure 13. Comparison of CLR for ARCMA and AMAPMT Protocols

It can be seen from Figure 13 that the performance, in terms of CLR of the AMAPMT protocol, is much better than that of the ARCMA protocol for all the media of a multimedia signal. Thus, the AMAPMT protocol can be used to improve the CLR performance for the various components of multimedia signals.

It can be seen from Figure 14 that the performance, in terms of MCTD of the AMAPMT protocol, is much better than that of the ARCMA protocol for all the media of a multimedia signal except for RT-VBR. Thus, the AMAPMT protocol can be used to improve the MCTD performance for the various components of multimedia signals.

It can be seen from Figure 15 that the performance, in terms of Throughput of the AMAPMT protocol, is much better than that of the ARCMA protocol for all the media of a multimedia signal except for CBR. Thus, the AMAPMT protocol can be used to improve the throughput performance for the various components of multimedia signals.

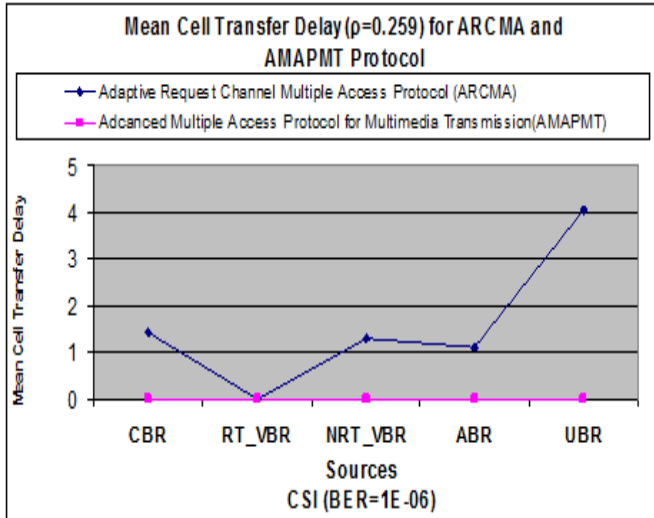


Figure 14. Comparison of MCTD for ARCMA and AMAPMT Protocols

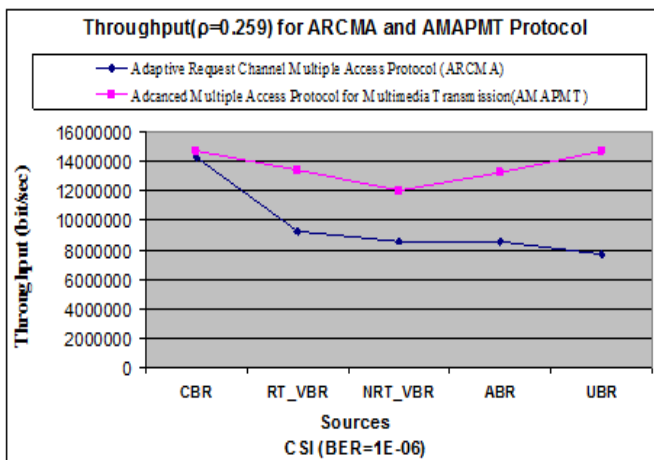


Figure 15. Comparison of Throughput for ARCMA and AMAPMT Protocols

As noted earlier, the currently-available multiple-access protocols deal only with voice and data and not a full complement of multimedia signals, and with an explicit priority scheme based on traffic types that can improve performance. However, the problem with priority assignment, according only to the type of media, is that some lower-priority media may have to wait too long and the information may become stale and may be considered lost. The stations have limited buffer space and some of the information may be lost due to buffer overflow. Further lower-quality data coming through the channels compete for resources with good data coming over channels with acceptable CSI. The proposed protocol improves performance in terms of CLR by taking out of consideration any data arriv-

ing over channels and assigning the highest priority to the most dominant CBR data tempered with providing priority to data of any type with short TTL values. The same procedures reduce the MCTD and improve the throughput at same time. Thus, consideration of explicit priorities, time to live (TTL) of transactions and channel state information (CSI) parameters, improve the overall performance.

Summary

Wireless networks suitable for multimedia (voice, video, ftp, data download, email and others) transmission were considered. A simulation model was developed and used to evaluate CLR and MCTD and Throughput for given link capacity, buffer size and input rate for selectable values of priorities of various media, TTL and CSI values. Thus, the algorithm can be used for allocation of resources at the nodes to obtain simultaneous satisfaction of prescribed end-to-end CLR, MCTD and Throughput for a given input rate.

The results of this study will be helpful in implementing and evaluating performance of multimedia communication over wireless networks under many selectable conditions. This will help in the design of such networks and protocols. The ability to communicate with multimedia signals is becoming more and more important and is going to impact society in many ways. The multiple-access protocol for multimedia transmission will enhance the performance and capability of wireless networks to handle multimedia signals. This will make these networks more useful for fulfilling the need of multimedia signals.

References

- [1] Awater, G. J. and Kruys, J., 'Wireless ATM – an overview', Mobile Networks and Applications, January 1996, pp 235-243,
- [2] Hac', A. and Chew, B.L., "ARCMA-Adaptive Request Channel Multiple Access Protocol for Wireless ATM Networks", International Journal of Network Management, Vol. 11. 2001, pp 333-363
- [3] Itraqi, Y., Boutaba, R. and Leon-Garcia, A. "QoS Control in Wireless ATM", Mobile Networks and Applications, May 2000, pp1-21,
- [4] Kwong Kwok, Y. and Lau, V., "A Performance Study of Multiple Access Control Protocol for Wireless Multimedia Services" IEEE International Conference on Network Protocols, November 2000, pp283-292
- [5] Karol, M.J., "An Efficient Demand-Assignment Multiple Access Protocol for Wireless Packet (ATM) Networks", Wireless Network, 1995, pp267-279.

-
- [6] Kwok, Y., "On Channel Adaptive Multiple Access Control without Contention Queue for Wireless Multimedia Services", *Wireless Networks*, 2003. pp379-392
 - [7] Frigon, J.F., Leung, V. and Chan, H.C., "Dynamic Reservation TDMA Protocol for Wireless ATM Networks", *IEEE journal on selected areas in communications*, Vol.19, No. 2, February, 2001, pp370-383
 - [8] Akyildiz, I.F., Driver, H. and Ho, Y.L., "An Adaptive FEC Scheme for Data Traffic in Wireless ATM Networks", *IEEE/ACM Transactions on Networking*, Vol.9, No.4, August 2001, pp419-426

Biographies

HONG YU received the B.S degree in Electrical Engineering from the University of Hunan, China in 1989 and His Ph.D. degree in Electrical Engineering from the Catholic University of America in 2008. Currently, He is Associate Professor of Electrical Engineering at Capitol College. His teaching and research areas included network communication protocol and embedded system design. Dr. Yu may be reached at yhong2006@gmail.com

MOHAMMED AROZULLAH received his B.S degree in Physics from Rajshahi University, Bangladesh, in 1956. He earned his M. Sc degree in Physics from Dhaka University, Bangladesh. He received the Ph.D degree in Electrical Engineering from University of Ottawa, Canada, 1967. Dr. Arozullah is Professor of Electronics Engineering and Computer Science at The Catholic University of America. Dr. Arozullah may be reached at arozullah@cua.edu

INSTRUCTIONS FOR AUTHORS: MANUSCRIPT REQUIREMENTS

The INTERNATIONAL JOURNAL OF MODERN ENGINEERING is an online/print publication, designed for Engineering, Engineering Technology, and Industrial Technology professionals. All submissions to this journal, submission of manuscripts, peer-reviews of submitted documents, requested editing changes, notification of acceptance or rejection, and final publication of accepted manuscripts will be handled electronically.

All manuscripts must be submitted electronically. Manuscripts submitted to the International Journal of Modern Engineering must be prepared in Microsoft Word 98 or higher (.doc) with all pictures, jpg's, gif's and pdf's included in the body of the paper. All communications must be conducted via e-mail to the manuscript editor at philipw@bgsu.edu with a copy to the editor at editor@ijme.us

The editorial staff of the International Journal of Modern Engineering reserves the right to format and edit any submitted word document in order to meet publication standards of the journal.

1. Word Document Page Setup: Top = 1", Bottom = 1", Left = 1.25", and Right = 1.25". This is the default setting for Microsoft Word. Do Not Use Headers or Footers.
2. Text Justification: Submit all text as "LEFT JUSTIFIED" with No paragraph indentation.
3. Page Breaks: No page breaks are to be inserted in your document.
4. Font Style: Use 11-point Times New Roman throughout the paper except where indicated otherwise.
5. Image Resolution: Images should be 96 dpi, and not larger than 460 X 345 Pixels.
6. Images: All images should be included in the body of the paper (.jpg or .gif format preferred).
7. Paper Title: Center at the top with 18-point Times New Roman (Bold).
8. Author and Affiliation: Use 12-point Times New Roman. Leave one blank line between the Title and the "Author and Affiliation" section. List on consecutive lines: the Author's name and the Author's Affiliation. If there are two authors follow the above guidelines by adding one space below the first listed author and repeat the process. If there are more than two authors, add one line below the last listed author and repeat the same procedure. Do not create a table or text box and place the "Author and Affiliation" information horizontally.
9. Body of the Paper: Use 11-point Times New Roman. Leave one blank line between the "Author's Affiliation" section and the body of the paper. Use a one-column format with left justification. Please do not use spaces between paragraphs and use 0.5" indentation as a break between paragraphs.
10. Abstracts: Abstracts are required. Use 11-point Times New Roman Italic. Limit abstracts to 250 words or less.
11. Headings: Headings are not required but can be included. Use 11-point Times New Roman (ALL CAPS AND BOLD). Leave one blank line between the heading and body of the paper.
12. Page Numbering: The pages should not be numbered.
13. Bibliographical Information: Leave one blank line between the body of the paper and the bibliographical information. The referencing preference is to list and number each reference when referring to them in the text (e.g. [2]), type the corresponding reference number inside of bracket [1]. Consider each citation as a separate paragraph, using a standard paragraph break between each citation. Do not use the End-Page Reference utility in Microsoft Word. You must manually place references in the body of the text. Use font size 11 Times New Roman.
14. Tables and Figures: Center all tables with the caption placed one space above the table and centered. Center all figures with the caption placed one space below the figure and centered.
15. Page limit: Submitted article should not be more than 15 pages.

College of Engineering, Technology, and Architecture

University of Hartford



For more information please visit us at
www.hartford.edu/ceta

For more information on undergraduate programs please contact Kelly Cofiell at cetainfo@hartford.edu.

For more information on Graduate programs please contact Laurie Grandstrand at grandstran@hartford.edu.

Toll Free: 1-800-766-4024
Fax: 1-800-768-5073



DEGREES OFFERED :

ENGINEERING UNDERGRADUATE

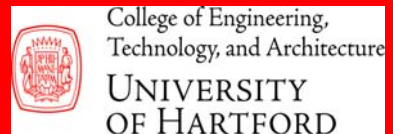
Acoustical Engineering and Music (B.S.E)
Biomedical Engineering (B.S.E)
Civil Engineering (B.S.C.E)
-Environmental Engineering Concentration
Environment Engineering (B.S.E)
Computer Engineering (B.S.Comp.E.)
Electrical Engineering (B.S.E.E.)
Mechanical Engineering (B.S.M.E.)
- Concentrations in Acoustics and
- Concentrations in Manufacturing

TECHNOLOGY UNDERGRADUATE

Architectural Engineering Technology (B.S.)
Audio Engineering Technology (B.S.)
Computer Engineering Technology (B.S.)
Electronic Engineering Technology (B.S.)
-Concentrations in Networking/
Communications and Mechatronics
Mechanical Engineering Technology (B.S.)

GRADUATE

Master of Architecture (M.Arch)
Master of Engineering (M.Eng)
• Civil Engineering
• Electrical Engineering
• Environmental Engineering
• Mechanical Engineering
- Manufacturing Engineering
- Turbomachinery
3+2 Program (Bachelor of Science and
Master of Engineering Degrees)
E²M Program (Master of Engineering and
Master of Business Administration)



IJME NOW SEEKS SPONSORS

**IJME IS THE OFFICAL AND FLAGSHIP JOURNAL OF THE
INTERNATIONAL ASSOCIATION OF JOURNALS AND CONFERENCE (IAJC)**

www.iajc.org



The International Journal of Modern Engineering (IJME) is a highly-selective, peer-reviewed journal covering topics that appeal to a broad readership of various branches of engineering and related technologies. IJME is steered by the IAJC distinguished board of directors and is supported by an international review board consisting of prominent individuals representing many well-known universities, colleges, and corporations in the United States and abroad.

IJME Contact Information

General questions or inquiries about sponsorship of the journal should be directed to:

Mark Rajai, Ph.D.

Editor-in-Chief

Office: (818) 677-2167

Email: editor@ijme.us

Department of Manufacturing Systems Engineering & Management

California State University-Northridge

1811 Nordhoff St.

Northridge, CA 91330